UNIVERSITY OF TRENTO

Doctoral School in Civil, Environmental and Mechanical Engineering

Curriculum 3. Modelling and Simulation

Mirko Tommasini

Flutter instability in structural mechanics

Theory and experimental evidence

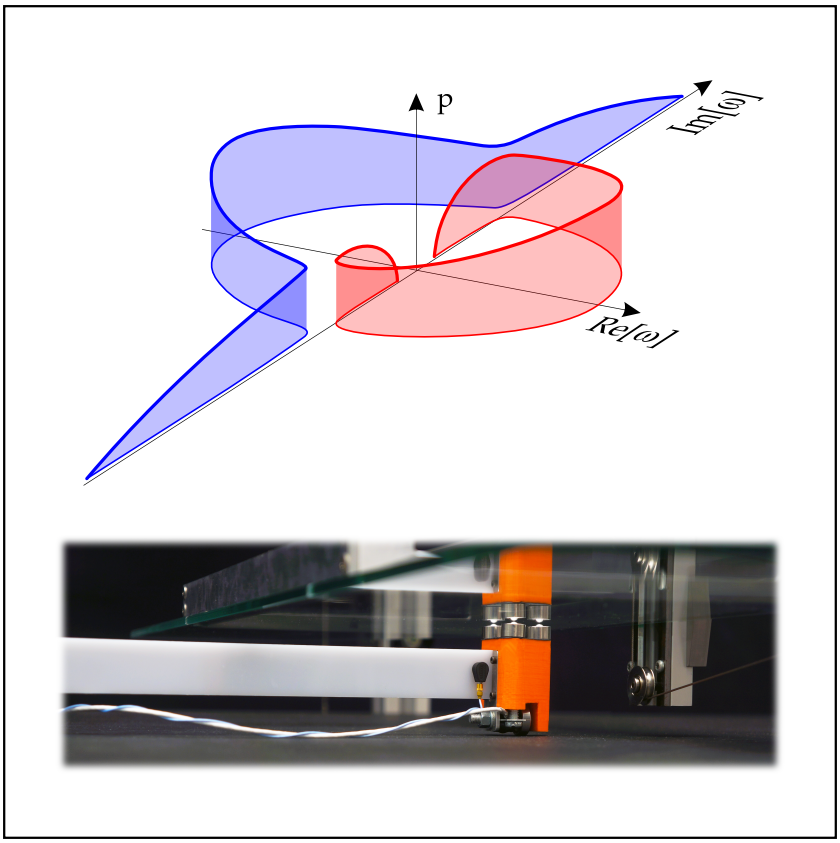

2018 - Doctoral thesis

UNIVERSITY OF TRENTO - Italy
Department of Civil, Environmental
and Mechanical Engineering

PhD in Civil, Environmental and Mechanical Engineering

Flutter Instability In Structural Mechanics

Theory and Experimental Evidence

Mirko Tommasini

Supervisors: Prof. Davide Bigoni
Dr. Diego Misseroni

Co-supervisors: Dr. Oleg N. Kirillov
Dr. Giovanni Noselli

2018

UNIVERSITY OF TRENTO
Department of Civil, Environmental and Mechanical Engineering
XXX Cycle

Final Examination:
10th April 2018

Board of Examiners:
Prof. Dennis M. Kochmann, ETH Zürich
Prof. Sèbastien Neukirch, Université Pierre et Marie Curie, Paris
Prof. Roberta Springhetti, Universitá degli Studi di Trento

The author gratefully acknowledges the financial support from the ERC Advanced Grant 'Instabilities and nonlocal multiscale modelling of materials' ERC-2013-ADG-340561-INSTABILITIES.

To my parents Flavia and Aligi,
together with Vittoria and Tito.

Acknowledgements

During my PhD course at the University of Trento I have met, known and worked with many people, and for this reason, first of all, I have to thank my supervisor Prof. Davide Bigoni for all the opportunities, advice and encouragements he gave me in the last three years. In addition, the financial support from the ERC Advanced Grant 'Instabilities and nonlocal multiscale modelling of materials' ERC - 2013 - ADG - 340561 - INSTABILITIES is to be acknowledged.

I am deeply grateful to Dr. Oleg N. Kirillov for his precious help in understanding the mathematics of dynamical system.

Moreover, I would like to thank Dr. Giovanni Noselli for the productive discussions about numerical simulations and agreements with the experimental results obtained inside the laboratory.

A special thank also goes to the technician Ludovic Taxis for his useful cooperation in the Instability Lab during the first year.

I would like to thank all the members of Solid and Structural Mechanics Group of the Department of Civil, Environmental and Mechanical Engineering, the team of Electronic Service and Design and the Physics Department of Mechanical Service.

Last but not least, my deep gratitude goes to the person who has been assisting me since 2011, firstly with the bachelor degree, secondly with the master degree and lastly with the PhD thesis. In all these years I learned a lot and, at this point, I can consider you as a true friend, not only as a mere supervisor: thank you Diego!

Trento, 10th April 2018

Mirko Tommasini

Articles

The results reported in the present thesis have been summarized in the following papers:

- M. Tommasini, O.N. Kirillov, D. Misseroni and D. Bigoni. The destabilizing effect of external damping: singular flutter boundary for the Pflüger column with vanishing external dissipation. *Journal of the Mechanics and Physics of Solids*, 91:204–215, 2016;

- D. Bigoni, O.N. Kirillov, D. Misseroni, G. Noselli and M. Tommasini. Flutter and dissipation instabilities in structures subject to friction follower forces. *International Union of Theoretical and Applied Mechanics*, 2016;

- O.N. Kirillov, D. Bigoni, D. Misseroni, G. Noselli and M. Tommasini. Experiments on the Pflüger column: flutter from friction. *JAXA Special Publication: Proceedings of the First International Symposium on Flutter and its Application*, 151–155, 2017;

- D. Bigoni, D. Misseroni, M. Tommasini, O.N. Kirillov and G. Noselli. Detecting singular weak-dissipation limit for futter onset in reversible

systems. *Phys. Rev. E*, 97, 023003;

- D. Bigoni, O.N. Kirillov, D. Misseroni, G. Noselli and M. Tommasini. Flutter and divergence instability in the Pflüger's column: experimental evidence of the Ziegler's destabilization paradox. (accepted).

Abstract

The present thesis summarizes the research activity in the field of elastic structures subject to tangential follower forces performed in the Instability Lab of the University of Trento.

Elastic structures loaded by nonconservative positional forces are interesting from different perspectives. First, they are subject to flutter instability, a dynamical instability which remains undetected using static approaches. Second, in these structures dissipation plays a fundamental and destabilizing role. Third, a critical load calculated in the limit of vanishing dissipation is found to be smaller than the critical load calculated in the same structure where the dissipation is assumed absent 'from the beginning'. This behaviour is so peculiar that is usually referred to as 'the Ziegler paradox' and was never experimentally substantiated before.

Flutter instability in elastic structures subject to follower load, the most important cases being the famous Beck's and Pflüger's columns (two elastic rods in a cantilever configuration, with an additional concentrated mass at the end of the rod in the latter case), have attracted, and still attract, a thorough research interest.

In the present thesis, the effects of internal and external damping, crucial

in the interpretation of experiments, have been investigated. Contrary to a common belief, it has been shown that the effect of external damping is qualitatively the same as the effect of internal damping, both yielding a pronounced destabilization paradox. This result corrects previous claims relative to destabilization by external damping of the Ziegler's and Pflüger's elastic structures.

The major challenge in the research area of follower forces is the practical realization of these forces, which was previously obtained only for the case of the Ziegler double pendulum (a two-degrees-of-freedom elastic system subject to a tangential force). Therefore, an experimental setup to introduce follower tangential forces at the end of an elastic rod was designed, realized, validated, and tested, in which the follower action is produced by exploiting Coulomb friction on an element (a freely-rotating wheel) in sliding contact against a plate (realized by a conveyor belt). It is therefore shown that follower forces can be realized in practice and the first experimental evidence is given of the flutter and divergence instability of the Pflüger's column. Load thresholds for both the two instabilities are measured for the first time. Moreover, the detrimental effect of dissipation on the critical load for flutter is experimentally demonstrated.

The introduced approach to follower forces discloses new horizons for testing self-oscillating structures and for exploring and documenting dynamic instabilities possible when nonconservative loads are applied.

Contents

List of Figures

List of Tables

1

Introduction

> The seeker after truth must, once in the course of his life, doubt everything, as far as is possible.
>
> *R. Descartes*

The debate on the existence of follower loads, forces which maintain their direction tangential to the deformed elastica, is of great interest in structural mechanics and in dynamical stability theory and roots in the work of Greenhill [3]. The peculiarity of a nonconservative system is the absence of a potential: in fact, the work produced by loads acting on such systems depends on the path followed by the structure in a closed loop. A follower load can in fact add energy to a mechanical system.

Nicolai [4] concluded that the stability of nonconservative systems could not be studied through a static approach, but required considerations of dynamics, see also Ziegler [5]. Several authors have later analysed stability of nonconservative systems, both analytically (Ziegler [1, 6, 7], Beck [2], Pflüger [8, 9], Rocard [10], Bolotin [11], Huseyin [12], Leipholz [13], Merkin [14], Kirillov [15], Paidoussis [16]) and experimentally (Hermann [17, 18], Wood [19], Prasad [20], Sugiyama [21], Bigoni [22]) and this research field

still represents an important topic in the stability of dynamical systems, including structural mechanics, physics, rotordynamics, aeroelasticity, and fluid-structure interaction, see the excellent critical overview provided by Elishakoff [23].

From the analytical point of view it is possible to analyze stability of a mechanical system subjected to a tangential follower force through a dynamical approach, from simple discrete systems (the most important among which is the Ziegler double pendulum, left of Fig. 1.1) to continuous systems (such as the Beck column, center of Fig. 1.1). In these elastic models other features can be added such as:

- a concentrated mass where the force is applied (thus obtaining the so-called 'Pflüger rod');
- an inclined follower force (in other words applied with a certain inclination with respect to the tangent);
- viscosity of the material (or internal damping);
- air drag (or external damping).

The above mentioned features are taken into account for the study of the Pflüger column (a generalization of the Beck column, right of Fig. 1.1), an elastic cantilever rod with a concentrated mass positioned at its free end. The initial dynamics and the stability threshold for this rod can be derived from a linearized theory, while a nonlinear numerical solution is the way to obtain a fully nonlinear structural response. A new mechanical apparatus, nicknamed 'flutter machine', was designed, realized, tested and used for investigations on instabilities that affect the Pflüger column, namely, *flutter instability* and *divergence instability*. The former instability is characterized by oscillations of increasing amplitude, which after a transient reach a steady-state regime, whereas the latter displays an exponentially blowing-up motion. In addition, the mechanical apparatus has for the first time provided the experimental proof of the destabilization role of dissipation, so that the introduction of a very small, but finite, damping in a system significantly lowers the critical flutter load (and slightly increases

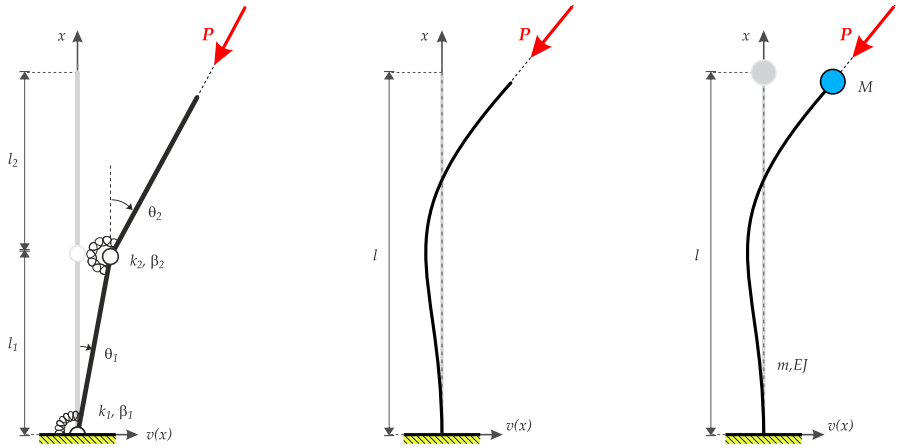

Figure 1.1: (Left) The scheme of the Ziegler double pendulum (Ziegler, 1952). (Center) The scheme of the Beck column (Beck, 1952). (Right) The scheme of the Pflüger column (Pflüger, 1955).

the critical divergence load). Moreover, the experiments have also revealed that not only the internal damping (such as viscosity of the material), but also external damping (such as air drag) have a destabilizing effect on both discrete and continuous mechanical systems

The 'flutter machine' represents, in a sense, a reply to the question posed by Doak [24]:

> *[...] should someone come forward with an experimental validation of the follower force concept, to a reasonable approximation, for some specific physical system then the day of universal rejection of follower force papers may never come.*

The topics treated in the Chapters of the present work are summarized in the following:

- Chapter 2 provides an introduction to the problem of the Ziegler double pendulum and the Beck column (a particular case of the Pflüger

column, where the end mass is set to zero) with a brief highlight on the Ziegler destabilization paradox;

- Chapter 3 is dedicated to the destabilization paradox due to air drag (where both the Ziegler double pendulum and the Pflüger column are analyzed);
- Chapter 4 collects all the experiments performed with the 'flutter machine' and the comparisons with both theoretical predictions and numerical simulations;
- Chapter 5 deals with the detection of the singular weak-dissipation limit for the flutter onset in a reversible system, giving an experimental proof to the Whitney umbrella singularity.

2

From discrete to continuous system

Do what you can where you are with what you have.

T. Roosevelt

This Chapter introduces the reader to the linearized theory of flutter instability in discrete and continuous systems. The starting point is the case of the Ziegler double pendulum, then the case of the Beck column is presented. These two mechanical systems can be excited by a nonconservative tangential load and are both affected by the so-called 'Ziegler paradox'. This destabilization paradox lowers down the critical flutter load of the ideal (undamped) system when a small, even tending to zero, source of damping is introduced.

2.1 The Ziegler double pendulum

Flutter in structural systems is analyzed under the hypothesis that follower forces are present. In general, these forces do not admit a potential and therefore are non-conservative, so that work can be extracted in a closed

path. The simplest nonconservative system subjected to a follower load is the 'Ziegler double pendulum' [1], a 2 d.o.f. system composed by two rigid bars, connected through an elastic hinge and fixed with another elastic hinge at one end, while subject to a tangential follower load at the other. This structure exhibits both flutter and divergence instabilities.

Subject to this load, we consider the two-degree-of-freedom rigid and massless rods system shown in Fig. 2.1, where two rotational springs of equal stiffnesses c provide the elasticity. The generic configuration of the system remains determined by the two Lagrangian parameters φ_1 and φ_2. The concentrated masses m_1 and m_2 are at a distance a_1 and a_2, respectively. The tangential follower load $\mathbf{P}$, applied at the free end and taken positive when compressive, maintains the direction parallel to the rod BC. The analysis of a mechanical system similar to that under consideration can be found in Herrmann [18], Ziegler [5–7, 25] and Nguyen [26], while the akin problem of a clamped elastic rod subjected to a load tangential to its axis at the free end has been solved by Beck [2] and Pflüger [9] (see the correspondent Section in the present Chapter).

The total kinetic energy of the system T can be written as

$$T = \frac{1}{2}\left[\left(m_1 a_1^2 + m_2 l^2\right)\dot{\varphi}_1^2 + 2m_2 l a_2 \dot{\varphi}_1 \dot{\varphi}_2 + m_2 a_2^2 \dot{\varphi}_2{}^2\right], \tag{2.1}$$

whereas the potential energy of the system (due to the rotational springs c) is

$$V = \frac{1}{2}\left[(2c)\,\varphi_1^2 - 2c\varphi_1\varphi_2 + (c)\,\varphi_2^2\right], \tag{2.2}$$

and the contribution of the nonconservative forces (due to the follower load $\mathbf{P}$ and the viscosity of the hinges b) is

$$Q_1 = Pl\,(\varphi_1 - \varphi_2) - b(2\dot{\varphi}_1 - \dot{\varphi}_2), \quad Q_2 = b\,(\dot{\varphi}_1 - \dot{\varphi}_2)\,. \tag{2.3}$$

Recalling the Lagrange's equations

$$\tfrac{d}{dt}\left(\tfrac{\partial L}{\partial \dot{\varphi}_k}\right) - \tfrac{\partial L}{\partial \varphi_k} = Q_k \qquad (L = T - V,\, k = 1, 2) \tag{2.4}$$

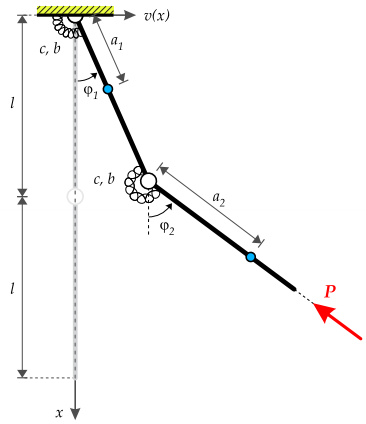

Figure 2.1: The Ziegler double pendulum as described in [1]: the follower force **P** is applied at the free end and remains parallel to the rod. The masses m_1 and m_2 are concentrated at distances a_1 and a_2. Both the rigid bars have the same length l. The elasticity c and the viscosity b of the system are concentrated in the hinges and the Lagragean parameters are φ_1 and φ_2.

it is simple to obtain the linearized equations that govern small motions of the Ziegler pendulum about the vertical equilibrium position in matrix form

$$\underbrace{\begin{bmatrix} m_1a_1^2 + m_2l^2 & m_2a_2l \\ m_2a_2l & m_2a_2^2 \end{bmatrix}}_{mass\ matrix} \begin{bmatrix} \ddot{\varphi}_1 \\ \ddot{\varphi}_2 \end{bmatrix} + \underbrace{\begin{bmatrix} 2b & -b \\ -b & b \end{bmatrix}}_{damping\ matrix} \begin{bmatrix} \dot{\varphi}_1 \\ \dot{\varphi}_2 \end{bmatrix} + \left(\overbrace{\begin{bmatrix} 2c & -c \\ -c & c \end{bmatrix}}^{stiffness\ matrix} + \overbrace{\begin{bmatrix} -Pl & Pl \\ 0 & 0 \end{bmatrix}}^{geometric\ matrix} \right) \begin{bmatrix} \varphi_1 \\ \varphi_2 \end{bmatrix} = 0. \tag{2.5}$$

Looking for time-harmonic vibrations near the equilibrium configuration, the Lagrangian parameters φ_k are assumed to be harmonic functions of time

$$\varphi_k = A_k\, e^{\lambda t}, \quad k = 1, 2 \tag{2.6}$$

where A_k are amplitudes, λ is the complex circular frequency, so that a substitution of Eq.(2.6) into Eqs.(2.5) yields to the generalized eigenvalue problem for λ, written in the matrix form

$$\left[\mathbf{K} + \mathbf{G} + \lambda\mathbf{D} + \lambda^2\mathbf{M}\right]\mathbf{a} = 0, \tag{2.7}$$

where $\mathbf{M}$ identifies the mass matrix, $\mathbf{D}$ the damping matrix, $\mathbf{K}$ the stiffness matrix and $\mathbf{G}$ the geometric matrix. Imposing the condition of null determinat of Eq.(2.7) leads to the characteristic equation

$$p_0\lambda^4 + p_1\lambda^3 + p_2\lambda^2 + p_3\lambda + p_4 = 0, \tag{2.8}$$

where the quantities p_0, p_1, p_2, p_3, p_4 are

$$\begin{aligned}
p_0 &= m_1 m_2 a_1^2 a_2^2 \\
p_1 &= \left[m_1 a_1^2 + m_2\left(l^2 + 2la_2 + 2a_2^2\right)\right] b \\
p_2 &= \left(m_1 a_1^2\right) c + m_2 a_2^2\,(2c - Pl) - m_2 l a_2\,(Pl - 2c) + b^2 \\
p_3 &= 2cb \\
p_4 &= c^2.
\end{aligned} \tag{2.9}$$

Eq.(2.8) contains the information of both the undamped (ideal) case, where dissipation is not taken into account from the beginning, and the damped case, where the viscosity of the hinges is computed. It is very simple at this point to show, both for the ideal and the damped case, the stability conditions for the Ziegler double pendulum.

2.1.1 Ideal case

Following Ziegler [1], consider first the case of m_1=$2m$, m_2=m, a_1=a_2=l, b=0. Eq.(2.8) becomes

$$2m^2l^4\lambda^4 + ml^2\left(7c - 2Pl\right)\lambda^2 + c^2 = 0. \tag{2.10}$$

The characteristic equation is quadratic in λ, with discriminant

$$\Delta = p_2^2 - 4p_0p_4 = m^2l^4\left(41c^2 - 28Plc + 4P^2l^2\right). \tag{2.11}$$

The following cases can arise:

- $(7c - 2Pl)$>0 and P<$\left(\frac{7}{2} - \sqrt{2}\right)\frac{c}{l}$: Eq.(2.11) has two real and positive values for λ^2, which correspond to a *stability condition*;
- $\left(\frac{7}{2} - \sqrt{2}\right)\frac{c}{l}$<$P$<$\left(\frac{7}{2} + \sqrt{2}\right)\frac{c}{l}$: Eq.(2.11) has two complex conjugated values for λ^2, which correspond to a *flutter instability*;
- P>$\left(\frac{7}{2} + \sqrt{2}\right)\frac{c}{l}$: Eq.(2.11) has two real and negative values for λ^2, which correspond to a *divergence instability.*

The instabilities that can arise from the Ziegler double pendulum have two different behaviours: flutter is characterised by a self-excited oscillation blowing up in time, whereas divergence instabilities shows a motion that grows in an exponential way. The critical flutter load in the ideal case is

$$P_{fl,i} = \left(\frac{7}{2} - \sqrt{2}\right)\frac{c}{l} \approx 2.086\frac{c}{l} \tag{2.12}$$

and the critical divergence load is

$$P_{div,i} = \left(\frac{7}{2} + \sqrt{2}\right) \approx 4.914\frac{c}{l} \tag{2.13}$$

2.1.2 Damped case

Let us consider now the damped case, imposing m_1=$2m$, m_2=m, a_1=a_2=l. Eq.(2.8) becomes now

$$2m^2l^4\lambda^4 + 7ml^2b\lambda^3 + \left[ml^2\left(7c - 2Pl\right) + b^2\right]\lambda^2 + 2cb\lambda + c^2 = 0. \quad (2.14)$$

In this case the characteristic equation is not quadratic in λ. The stability of the system can be determined with the aid of the Routh-Hurwitz criterion

$$\begin{aligned} &7ml^2b > 0, \\ &ml^2b\left[7b^2 + ml^2\left(45c - 14Pl\right)\right] > 0, \\ &ml^2b^2c\left[14b^2 + ml^2\left(41c - 28Pl\right)\right] > 0, \\ &c^2 > 0. \end{aligned} \quad (2.15)$$

Assuming a positive value for the viscosity and the stiffness of the springs (which means b>0 and c>0), the following cases can arise:

- P<$\left(\frac{41}{28}\frac{c}{l} + \frac{1}{2}\frac{b^2}{ml^3}\right)$: the real parts of the eigenfrequencies λ are all negative with imaginary part different from zero, which correspond to a *stability condition*;
- P>$\left(\frac{41}{28}\frac{c}{l} + \frac{1}{2}\frac{b^2}{ml^3}\right)$: at least one eigenfrequencies λ has a positive real part with imaginary part different from zero, which correspond to a *flutter instability*;
- the positive real part of the eigenfrequency λ has null imaginary part, which correspond to a *divergence instability.*

This is the mathematical proof of the destabilization paradox by Ziegler: in fact, in the limit of vanishing damping ($b \to 0$) the critical flutter load becomes

$$P_{fl,d} = \frac{41}{28}\frac{c}{l} \approx 1.464\frac{c}{l} \quad (2.16)$$

whereas the divergence load increases (on the boundary between flutter and divergence). An in depth numerical analysis of this can be found in Appendix A.2 of [22].

2.2 The Beck column

Beck [2] has introduced a scheme of a cantilever rod, which is clamped at one end and subject to a tangential load at the other, Fig. 2.2.

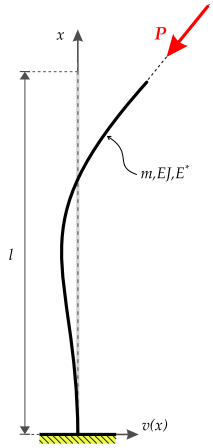

Figure 2.2: The Beck column as described in [2]. The column is clamped at the bottom and loaded with a force of intensity **P** at its free end. The system has mass per unit length m; flexural rigidity EJ and viscous modulus E^*.

The Beck column can be generalized with an end mass on the free end, leading to the so-called Pflüger column [8, 9]. These mechanical systems can be considered as the continuous elastic realization of the Ziegler double pendulum. The more general case of the damped Pflüger column is treated from an analitycal point of view in Chapter 4 and Appendix B. In the following the main goal is to obtain the critical flutter load for the Beck column in the absence of internal damping (ideal case) and taking into

account viscosity (damped case), showing the presence of the destabilization paradox also for a continuous system.

The linearized differential equation of motion which governs the dynamics of the damped Beck column, loaded by a follower force of intensity **P**, is

$$EJv''''(x,t) + E^*J\dot{v}''''(x,t) + Pv''(x,t) + m\ddot{v}(x,t) = 0, \tag{2.17}$$

where m is the mass density of the rod per unit length, E^* the viscous modulus, EJ the flexural rigidity of the column (see Fig. 2.2). Imposing the boundary condition

$$\begin{aligned} &v(0,t) = v'(0,t) = 0, \\ &-J[Ev''(l,t) - E^*\dot{v}''(l,t)] = 0, \\ &-J[Ev'''(l,t) - E^*\dot{v}'''(l,t)] = 0, \end{aligned} \tag{2.18}$$

and introducing the dimensionless quantities

$$\xi = \tfrac{x}{l}, \quad \tau = \tfrac{t}{l^2}\sqrt{\tfrac{EJ}{m}}, \quad p = \tfrac{Pl^2}{EJ}, \quad \eta = \tfrac{E^*}{El^2}\sqrt{\tfrac{EJ}{m}}, \tag{2.19}$$

the differential equation (2.17) can be rewritten as

$$v''''(\xi,\tau) + \eta\dot{v}''''(\xi,\tau) + pv''(\xi,\tau) + \ddot{v}(\xi,\tau) = 0, \tag{2.20}$$

Looking for time-harmonic vibrations in terms of the dimensionless pulsation ω

$$v(\xi,\tau) = \tilde{v}(\xi)\, e^{\omega\tau}, \tag{2.21}$$

the substitution of Eq.(2.21) into Eq.(2.20) yields the equation

$$\lambda^4(1+\eta\omega) + \lambda^2 p + \omega^2 = 0, \tag{2.22}$$

which admits the solutions

$$\lambda_{1,2}^2 = \frac{\sqrt{p^2 - 4(1+\eta\omega)\omega^2} \mp p}{2(1+\eta\omega)}. \tag{2.23}$$

Therefore, $\tilde{v}$ can be written in the form

$$\tilde{v}(\xi) = A_1 \sinh(\lambda_1\xi) + A_2 \cosh(\lambda_1\xi) + A_3 \sin(\lambda_2\xi) + A_4 \cos(\lambda_2\xi), \tag{2.24}$$

where A_i $(i = 1, .., 4)$ are arbitrary constants.

The boundary conditions of Eq.(2.18) can be rewritten in a dimensionless form as

$$\begin{aligned} &\tilde{v}(0) = \tilde{v}'(0) = 0, \\ &(1+\eta\omega)\tilde{v}''(1) = 0, \\ &(1+\eta\omega)\tilde{v}'''(1) = 0. \end{aligned} \tag{2.25}$$

A substitution of the boundary conditions (2.25) in the solution (2.24) yields an algebraic system of equations which admits non-trivial solutions at the vanishing of the determinant of the matrix of coefficients

$$\begin{bmatrix} 0 & 1 & 0 & 1 \\ \lambda_1 & 0 & \lambda_2 & 0 \\ \lambda_1^2 \sinh\lambda_1 & \lambda_1^2 \cosh\lambda_1 & -\lambda_2^2 \sin\lambda_2 & -\lambda_2^2 \cos\lambda_2 \\ \lambda_1^3 \cosh\lambda_1 & \lambda_1^3 \sinh\lambda_1 & -\lambda_2^3 \cos\lambda_2 & \lambda_2^3 \sin\lambda_2 \end{bmatrix}. \tag{2.26}$$

Noting that the λ_i's are functions of the applied load p, the pulsation ω, the viscosity η, the vanishing of the determinant of (2.26) corresponds

to the transcendental equation

$$\begin{aligned} f(p,\omega,\eta) \quad &= \lambda_1\lambda_2(1+\eta\omega)(\lambda_1^4+\lambda_2^4)+ \\ &+\lambda_1\lambda_2[2(1+\eta\omega)\lambda_1^2\lambda_2^2]\cosh\lambda_1\cos\lambda_2+ \\ &+\lambda_1^2\lambda_2^2(1+\eta\omega)(\lambda_2^2-\lambda_1^2)\sinh\lambda_1\sin\lambda_2. \end{aligned} \tag{2.27}$$

Once determined the value of the parameter η, the transcendental equation (2.27) describes the boundaries for which flutter occurs in both ideal and damped case. In particular, the system is unstable by flutter when the pulsation ω is complex with Re[ω]>0. System is stable if all the complex ω have negative real part of pulsation.

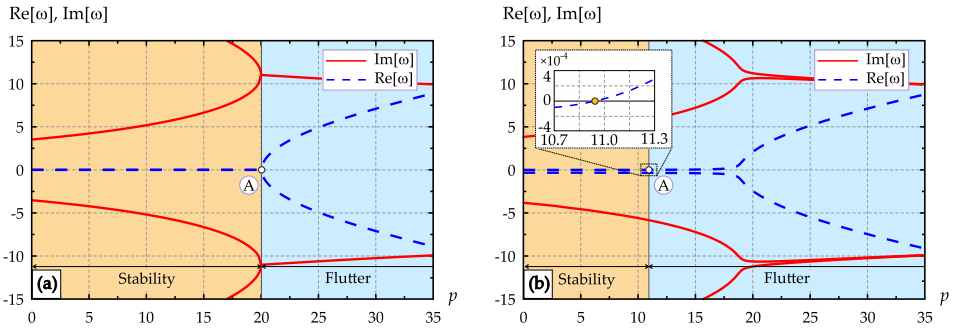

Figure 2.3: Branches of the real (Re[ω]) and imaginary (Im[ω]) parts of the pulsation for vibration of the Beck column as functions of the dimensionless load p. The undamped case (in which damping is absent 'from the beginning') is reported in (a), where flutter occurs at $p = 20.05$. The damped case is shown in (b), where is visible the drop of the flutter load to $p = 10.94$. Flutter occurs when a real branch of the pulsation $\tilde{\omega}$ becomes positive (with non-null values of the imaginary part of the pulsation). The detrimental effect of dissipation on the critical load is evident.

In Fig. 2.3 is shown a comparison between an ideal case and damped case for the Beck column (choosing the following values of the parameter, l=0.350 m, EJ=0.033 Nm^2, E^*J=7.078·10^{-6} Nsm^2): is clearly visible that the introduction of a small, but finite, damping source into the system leads

to a drop of the critical flutter load.

This is the proof of the destabilization paradox in a continuous system.

3

Destabilization paradox due to external damping

In nonconservative systems the smallest damping can significantly modify the critical load.

H. Ziegler

Elastic structures loaded by nonconservative positional forces are prone to instabilities induced by dissipation: it is well-known in fact that internal viscous damping destabilizes the marginally stable Ziegler double pendulum and Pflüger column. The result is the so-called 'destabilization paradox', where the critical force for flutter instability decreases by an order of magnitude when the coefficient of internal damping becomes infinitesimally small. Until now external damping, such as that related to air drag, is believed to provide only a stabilizing effect, as one would intuitively expect. Contrary to this belief, it will be shown that the effect of external damping is qualitatively the same as the effect of internal damping, yielding a pronounced destabilization paradox. Previous results relative to destabilization by external damping of the Ziegler's and Pflüger's elastic structures are corrected in a definitive way leading to a new understanding of the destabilizating role played by viscous terms.

3.1 Introduction

3.1.1 A premise: the Ziegler destabilization paradox

In his pioneering work Ziegler [1] considered asymptotic stability of a two-linked pendulum loaded by a tangential follower force P, as a function of the internal damping in the viscoelastic joints connecting the two rigid and weightless bars (both of length l, Fig. 3.1(c)). The pendulum carries two point masses: the mass m_1 at the central joint and the mass m_2 mounted at the loaded end of the pendulum. The follower force P is always aligned with the second bar of the pendulum, so that its work is non-zero along a closed path, which provides a canonical example of a nonconservative positional force.

For two non-equal masses ($m_1 = 2m_2$) and null damping, Ziegler found that the pendulum is marginally stable and all the eigenvalues of the 2×2 matrix governing the dynamics are purely imaginary and simple, if the load falls within the interval $0 \leq P < P_u^-$, where

$$P_u^- = \left(\frac{7}{2} - \sqrt{2}\right)\frac{k}{l} \approx 2.086\frac{k}{l}, \tag{3.1}$$

and k is the stiffness coefficient, equal for both joints. When the load P reaches the value P_u^-, two imaginary eigenvalues merge into a double one and the matrix governing dynamics becomes a Jordan block. With the further increase of P this double eigenvalue splits into two complex conjugate. The eigenvalue with the positive real part corresponds to a mode with an oscillating and exponentially growing amplitude, which is called flutter, or oscillatory, instability. Therefore, $P = P_u^-$ marks the onset of flutter in the *undamped* Ziegler double pendulum.

When the internal linear viscous damping in the joints is taken into account, Ziegler found another expression for the onset of flutter: $P = P_i$, where

$$P_i = \frac{41}{28}\frac{k}{l} + \frac{1}{2}\frac{c_i^2}{m_2 l^3}, \tag{3.2}$$

and c_i is the damping coefficient, assumed to be equal for both joints. The peculiarity of Eq.(3.2) is that in the limit of vanishing damping, $c_i \longrightarrow 0$, the flutter load P_i tends to the value $41/28\,k/l \approx 1.464\,k/l$, considerably lower than that calculated when damping is absent from the beginning, namely, the P_u^- given by Eq.(3.1). This is the so-called *Ziegler's destabilization paradox* [1, 11].

The reason for the paradox is the existence of the Whitney umbrella singularity on the boundary of the asymptotic stability domain of the dissipative system [27–29][1].

In structural mechanics, two types of viscous dampings are considered:

- *internal* is related to the viscosity of the structural material;
- *external*, is connected to the presence of external actions, such as air drag resistance during oscillations.

These two terms enter the equations of motion of an elastic rod as proportional respectively to the fourth spatial derivative of the velocity and to the velocity of the points of the elastic line.

Of the two dissipative terms only the internal viscous damping is believed to yield the destabilization paradox [11, 31, 32].

3.1.2 A new, destabilizing role for external damping

Differently from internal damping, *the role of external damping is commonly believed to be a stabilizing factor,* in an analogy with the role of sta-

[1] In the vicinity of this singularity, the boundary of the asymptotic stability domain is a ruled surface with a self-intersection, which corresponds to a set of marginally stable undamped systems. For a fixed damping distribution, the convergence to the vanishing damping case occurs along a ruler that meets the set of marginally stable undamped systems at a point located far from the undamped instability threshold, yielding the singular flutter onset limit for almost all damping distributions. Nevertheless, there exist particular damping distributions that, if fixed, allow for a smooth convergence to the flutter threshold of the undamped system in case of vanishing dissipation [11, 15, 27, 29, 30].

tionary damping in rotor dynamics [11, 33]. A full account of this statement together with a review of the existing results is provided in A.1.

Since internal and external damping are inevitably present in any experimental realization of the follower force [19, 21, 22], it becomes imperative to know how these factors affect the flutter boundary of both the Ziegler double pendulum with arbitrary mass distribution and the Pflüger column. These structures are fully analyzed in the present article, with the purpose of showing that:

- external damping is a destabilizing factor, which leads to the destabilization paradox (mentioned in the following as *external damping paradox*) for all mass distributions;

- surprisingly, for a finite number of particular mass distributions, the flutter loads of the externally damped structures converge to the flutter load of the undamped case (so that only in these exceptional cases the destabilizing effect is not present);

- the destabilization paradox is more pronounced in the case when the mass of the column or pendulum is smaller then the end mass.

Taking into account also the destabilizing role of internal damping, the results presented in this chapter demonstrate a completely new role of external damping as a destabilizing effect and suggest that destabilization paradoxes have a much better chance of being observed in the experiments with both discrete and continuous nonconservative systems than was previously believed.

3.2 External damping paradox in the Ziegler double pendulum

The linearized equations of motion for the Ziegler double pendulum (Fig. 3.1(c)), made up of two rigid bars of length l, loaded by a follower

force P, when both internal and external damping are present, have the form [34, 35]

$$\mathbf{M}\ddot{\mathbf{x}} + c_i\mathbf{D}_i\dot{\mathbf{x}} + c_e\mathbf{D}_e\dot{\mathbf{x}} + \mathbf{K}\mathbf{x} = 0, \tag{3.3}$$

where a superscript dot denotes time derivative and c_i and c_e are the coefficients of internal and external damping, respectively, in front of the corresponding matrices $\mathbf{D}_i$ and $\mathbf{D}_e$

$$\mathbf{D}_i = \begin{pmatrix} 2 & -1 \\ -1 & 1 \end{pmatrix}, \quad \mathbf{D}_e = \frac{l^3}{6}\begin{pmatrix} 8 & 3 \\ 3 & 2 \end{pmatrix}, \tag{3.4}$$

and $\mathbf{M}$ and $\mathbf{K}$ are respectively the mass and the stiffness matrices, defined as

$$\mathbf{M} = \begin{pmatrix} m_1l^2 + m_2l^2 & m_2l^2 \\ m_2l^2 & m_2l^2 \end{pmatrix}, \quad \mathbf{K} = \begin{pmatrix} -Pl + 2k & Pl - k \\ -k & k \end{pmatrix}, \tag{3.5}$$

in which k is the elastic stiffness of both viscoelastic springs acting at the hinges.

Assuming a time-harmonic solution to the Eq.(3.3) in the form $\mathbf{x} = \mathbf{u}e^{\sigma t}$ and introducing the non-dimensional parameters

$$\lambda = \frac{\sigma l}{k}\sqrt{km_2}, \quad E = c_e\frac{l^2}{\sqrt{km_2}}, \quad B = \frac{c_i}{l\sqrt{km_2}}, \quad F = \frac{Pl}{k}, \quad \mu = \frac{m_2}{m_1}, \tag{3.6}$$

an eigenvalue problem is obtained, which eigenvalues λ are the roots of the characteristic polynomial

$$\begin{aligned} p(\lambda) \;=\; & 36\lambda^4 + 12(15B\mu + 2E\mu + 3B + E)\lambda^3 + \\ & (36B^2\mu + 108BE\mu + 7E^2\mu - 72F\mu + 180\mu + 36)\lambda^2 + \\ & 6\mu(-5EF + 12B + 18E)\lambda + 36\mu. \end{aligned} \tag{3.7}$$

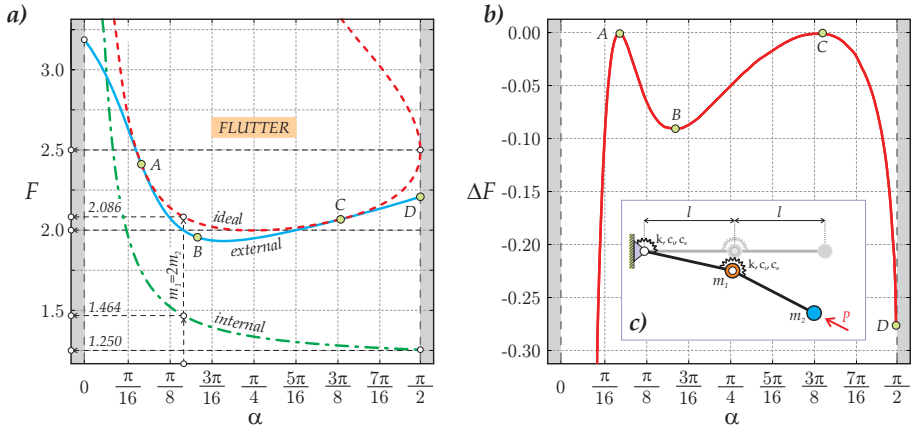

Figure 3.1: (a) The (dimensionless) tangential force F, shown as a function of the (transformed via $\cot\alpha = m_1/m_2$) mass ratio α, represents the flutter domain of (dashed/red line) the undamped, or 'ideal', Ziegler double pendulum and the flutter boundary of the dissipative system in the limit of vanishing (dot-dashed/green line) internal and (continuous/blue line) external damping. (b) Discrepancy ΔF between the critical flutter load for the ideal Ziegler double pendulum and for the same structure calculated in the limit of vanishing external damping. The discrepancy quantifies the size of the paradoxical drop in the flutter load.

In the undamped case, when $B = 0$ and $E = 0$, the pendulum is stable, if $0 \le F < F_u^-$, unstable by flutter, if $F_u^- \le F \le F_u^+$, and unstable by divergence, if $F > F_u^+$, where [36]

$$F_u^{\pm}(\mu) = \frac{5}{2} + \frac{1}{2\mu} \pm \frac{1}{\sqrt{\mu}}. \tag{3.8}$$

In order to plot the stability map for all mass distributions $0 \le \mu < \infty$, a parameter $\alpha \in [0, \pi/2]$ is introduced, so that $\cot\alpha = \mu^{-1}$ and hence

$$F_u^{\pm}(\alpha) = \frac{5}{2} + \frac{1}{2}\cot\alpha \pm \sqrt{\cot\alpha}. \tag{3.9}$$

The curves (3.9) form the boundary of the flutter domain of the un-

damped, or 'ideal', Ziegler double pendulum shown in Fig. 3.1(a) (red/dashed line) in the load versus mass distribution plane [37, 38]. The smallest flutter load $F_u^- = 2$ corresponds to $m_1 = m_2$, i.e. to $\alpha = \pi/4$. When α equals $\pi/2$, the mass at the central joint vanishes ($m_1 = 0$) and $F_u^- = F_u^+ = 5/2$. When α equals $\arctan(0.5) \approx 0.464$, the two masses are related as $m_1 = 2m_2$ and $F_u^- = 7/2 - \sqrt{2}$. In the case when only internal damping is present ($E = 0$) the Routh-Hurwitz criterion yields the flutter threshold as [38]

$$F_i(\mu, B) = \frac{25\mu^2 + 6\mu + 1}{4\mu(5\mu + 1)} + \frac{1}{2}B^2. \tag{3.10}$$

For $\mu = 0.5$ Eq.(3.10) reduces to Ziegler's formula (3.2). The limit for vanishing internal damping is

$$\lim_{B\to 0} F_i(\mu, B) = F_i^0(\mu) = \frac{25\mu^2 + 6\mu + 1}{4\mu(5\mu + 1)}. \tag{3.11}$$

The limit $F_i^0(\mu)$ of the flutter boundary at vanishing internal damping is shown in green in Fig. 3.1(a). Note that $F_i^0(0.5) = 41/28$ and $F_i^0(\infty) = 5/4$. For $0 \le \mu < \infty$ the limiting curve $F_i^0(\mu)$ has no common points with the flutter threshold $F_u^-(\mu)$ of the ideal system, which indicates that the internal damping causes the Ziegler destabilization paradox for *every* mass distribution.

In a route similar to the above, by employing the Routh-Hurwitz criterion, the critical flutter load of the Ziegler double pendulum with the external damping $F_e(\mu, E)$ can be found

$$\begin{aligned} F_e(\mu, E) &= \frac{122\mu^2 - 19\mu + 5}{5\mu(8\mu - 1)} + \frac{7(2\mu + 1)}{36(8\mu - 1)}E^2 \\ &- (2\mu + 1)\frac{\sqrt{35E^2\mu(35E^2\mu - 792\mu + 360) + 1296(281\mu^2 - 130\mu + 25)}}{180\mu(8\mu - 1)} \end{aligned}$$

and its limit calculated when $E \to 0$, which provides the result

$$F_e^0(\mu) = \frac{122\mu^2 - 19\mu + 5 - (2\mu + 1)\sqrt{281\mu^2 - 130\mu + 25}}{5\mu(8\mu - 1)}. \tag{3.12}$$

The limiting curve (3.12) is shown in blue in Fig. 3.1(a). It has a minimum $\min_\mu F_e^0(\mu) = -28 + 8\sqrt{14} \approx 1.933$ at $\mu = (31 + 7\sqrt{14})/75 \approx 0.763$.

Remarkably, *for almost all* mass ratios, *except two* (marked as A and C in Fig. 3.1(a)), the limit of the flutter load $F_e^0(\mu)$ is *below* the critical flutter load $F_u^-(\mu)$ of the undamped system. It is therefore concluded that external damping causes the discontinuous decrease in the critical flutter load exactly as it happens when internal damping vanishes. *Qualitatively*, the effect of vanishing internal and external damping is *the same*. The only difference is the magnitude of the discrepancy: the vanishing internal damping limit is larger than the vanishing external damping limit, see Fig. 3.1(b), where $\Delta F(\mu) = F_e(\mu) - F_u^-(\mu)$ is plotted.

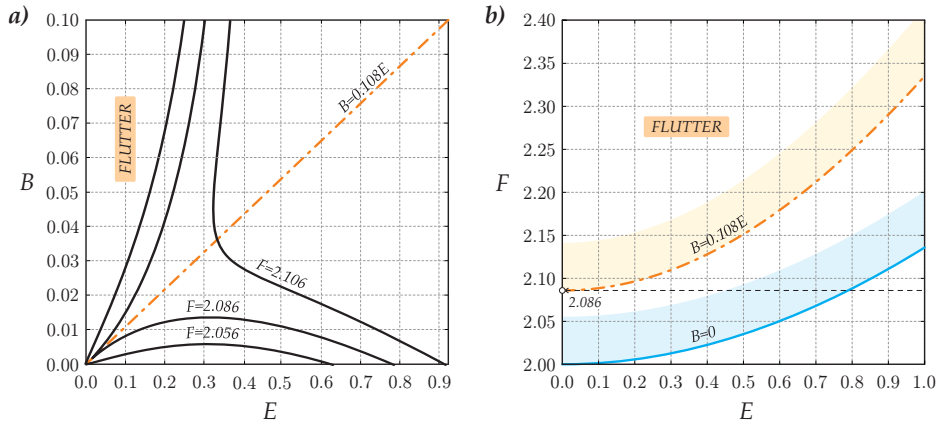

Figure 3.2: Analysis of the Ziegler double pendulum with fixed mass ratio, $\mu = m_2/m_1 = 1/2$: (a) contours of the flutter boundary in the internal/external damping plane, (B, E), and (b) critical flutter load as a function of the external damping E (continuous/blue curve) along the null internal damping line, $B = 0$, and (dot-dashed/orange curve) along the line $B = \left(8/123 + 5\sqrt{2}/164\right) E$.

For example, $\Delta F \approx -0.091$ at the local minimum for the discrepancy, occurring at the point B with $\alpha \approx 0.523$. The largest finite drop in the flutter load due to external damping occurs at $\alpha = \pi/2$, marked as point D

in Fig. 3.1(a,b):

$$\Delta F = \frac{11}{20} - \frac{1}{20}\sqrt{281} \approx -0.288. \tag{3.13}$$

For comparison, at the same value of α, the flutter load drops due to internal damping of exactly 50%, namely, from 2.5 to 1.25, see Fig. 3.1(a,b).

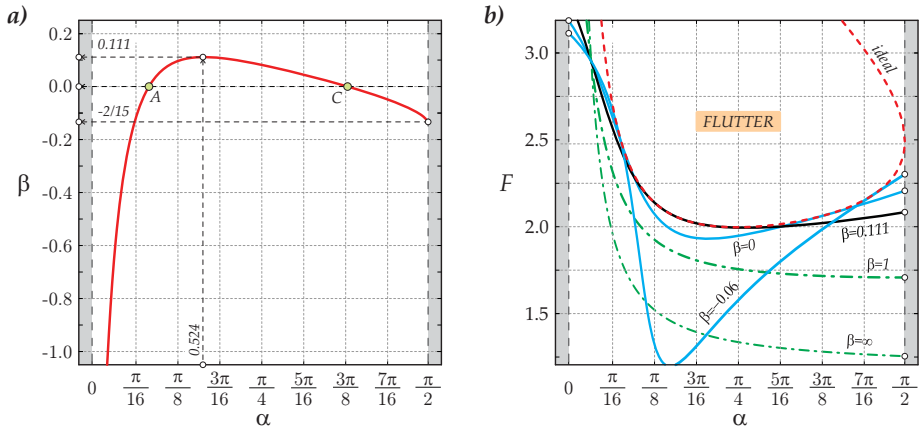

Figure 3.3: Analysis of the Ziegler double pendulum. (a) Stabilizing damping ratios $\beta(\mu)$ according to Eq.(3.19) with the points A and C corresponding to the tangent points A and C in Fig. 3.1(a) and to the points A and C of vanishing discrepancy $\Delta F = 0$ in Fig. 3.1(b). (b) The limits of the flutter boundary for different damping ratios β have: two or one or none common points with the flutter boundary (dashed/red line) of the undamped Ziegler double pendulum, respectively when $\beta < 0.111$ (continuous/blue curves), $\beta \approx 0.111$ (continuous/black curve), and $\beta > 0.111$ (dot-dashed/green curves).

As a particular case, for the mass ratio $\mu = 1/2$, considered by [34] and [35], the following limit flutter load is found

$$F_e^0(1/2) = 2, \tag{3.14}$$

only slightly inferior to the value for the undamped system, $F_u^-(1/2) = 7/2 - \sqrt{2} \approx 2.086$. This discrepancy passed unnoticed in Plaut [34, 35] but gives evidence to the destabilizing effect of external damping. To appreciate

this effect, the contours of the flutter boundary in the (B, E) - plane are plotted in Fig. 3.2(a) for three different values of F. The contours are typical of a surface with a Whitney umbrella singularity at the origin [29]. At $F = 7/2 - \sqrt{2}$ the stability domain assumes the form of a cusp with a unique tangent line, $B = \beta E$, at the origin, where

$$\beta = \frac{8}{123} + \frac{5}{164}\sqrt{2} \approx 0.108. \tag{3.15}$$

For higher values of F the flutter boundary is displaced from the origin, Fig. 3.2(a), which indicates the possibility of a continuous increase in the flutter load with damping. Indeed, along the direction in the (B, E) - plane with the slope (3.15) the flutter load increases as

$$F(E) = \frac{7}{2} - \sqrt{2} + \left(\frac{47887}{242064} + \frac{1925}{40344}\sqrt{2}\right) E^2 + o(E^2), \tag{3.16}$$

see Fig. 3.2(b), and monotonously tends to the undamped value as $E \to 0$. On the other hand, along the direction in the (B, E) - plane specified by the equation $B = 0$, the following condition is obtained

$$F(E) = 2 + \frac{14}{99}E^2 + o(E^2), \tag{3.17}$$

see Fig. 3.2(b), with the convergence to a lower value $F = 2$ as $E \to 0$. In general, the limit of the flutter load along the line $B = \beta E$ when $E \to 0$ is

$$F(\beta) = \frac{504\beta^2 + 1467\beta + 104 - (4 + 21\beta)\sqrt{576\beta^2 + 1728\beta + 121}}{30(1 + 14\beta)} \leq \frac{7}{2} - \sqrt{2}, \tag{3.18}$$

an equation showing that for almost all directions the limit is lower than the ideal flutter load. The limits only coincide in the sole direction specified by Eq.(3.15), which is different from the E-axis, characterized by $\beta = 0$. As a conclusion, pure external damping yields the destabilization paradox even at $\mu = 1/2$, which was unnoticed in Plaut [34, 35].

In the limit of vanishing external (E) and internal (B) damping, a ratio of the two $\beta = B/E$ exists for which the critical load of the undamped system is attained, so that the Ziegler's paradox does not occur. This ratio can therefore be called 'stabilizing', it exists for every mass ratio $\mu = m_2/m_1$, and is given by the expression

$$\beta(\mu) = -\frac{1}{3}\frac{(10\mu-1)(\mu-1)}{25\mu^2+6\mu+1} + \frac{1}{12}\frac{(13\mu-5)(3\mu+1)}{25\mu^2+6\mu+1}\mu^{-1/2}. \qquad (3.19)$$

Eq.(3.19) reduces for $\mu = 1/2$ to Eq.(3.15) and gives $\beta = -2/15$ in the limit $\mu \to \infty$. With the damping ratio specified by Eq.(3.19) the critical flutter load has the following Taylor expansion near $E = 0$:

$$\begin{aligned} F(E,\mu) &= F_u^-(\mu) + \beta(\mu)\frac{(5\mu+1)(41\mu+7)}{6(25\mu^2+6\mu+1)}E^2 \\ &+ \frac{636\mu^3+385\mu^2-118\mu+25}{288(25\mu^2+6\mu+1)\mu}E^2 + o(E^2), \end{aligned} \qquad (3.20)$$

yielding Eq.(3.16) when $\mu = 1/2$. Eq.(3.20) shows that the flutter load reduces to the undamped case when $E = 0$ (called 'ideal' in the figure).

When the stabilizing damping ratio is null, $\beta = 0$, convergence to the critical flutter load of the undamped system occurs by approaching the origin in the (B, E) - plane along the E - axis. The corresponding mass ratio can be obtained finding the roots of the function $\beta(\mu)$ defined by Eq.(3.19). This function has only two roots for $0 \leq \mu < \infty$, one at $\mu \approx 0.273$ (or $\alpha \approx 0.267$, marked as point A in Fig. 3.3(a)) and another at $\mu \approx 2.559$ (or $\alpha \approx 1.198$, marked as point C in Fig. 3.3(a)).

Therefore, if $\beta = 0$ is kept in the limit when the damping tends to zero, the limit of the flutter boundary in the load versus mass ratio plane will be obtained as a curve showing two common points with the flutter boundary of the undamped system, exactly at the mass ratios corresponding to the points denoted as A and C in Fig. 3.1(a), respectively characterized by $F \approx 2.417$ and $F \approx 2.070$.

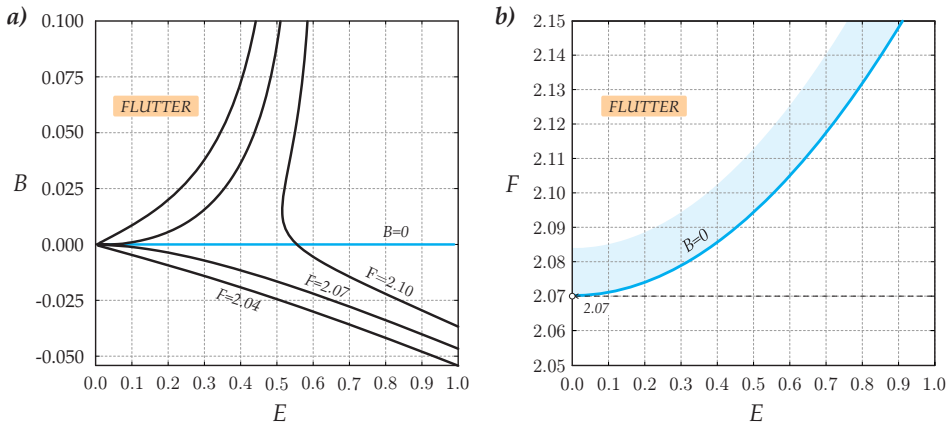

Figure 3.4: Analysis of the Ziegler double pendulum with fixed mass ratio, $\mu \approx 2.559$: (a) contours of the flutter boundary in the internal/external damping plane, (B, E), and (b) critical flutter load as a function of external damping E (continuous/blue curve) along the null internal damping line, $B = 0$.

If for instance the mass ratio at the point C is considered and the contour plots are analyzed of the flutter boundary in the (B, E) - plane, it can be noted that at the critical flutter load of the undamped system, $F \approx 2.07$, the boundary evidences a cusp with only one tangent coinciding with the E axis, Fig. 3.4(a). It can be therefore concluded that at the mass ratio $\mu \approx 2.559$ the external damping alone has a stabilizing effect and the system does not demonstrate the Ziegler paradox due to small external damping, see Fig. 3.4(b), where the the flutter load $F(E)$ is shown.

Looking back at the damping matrices (3.4) one may ask, what is the property of the damping operator which determines its stabilizing or destabilizing character. The answer to this question (provided by Kirillov [15, 39] via perturbation of multiple eigenvalues) involves all the three matrices **M** (mass), **D** (damping), and **K** (stiffness). In fact, the distributions of mass, stiffness, and damping should be related in a specific manner in order that the three matrices (**M**, **D**, **K**) have a stabilizing effect (see A.2 for details).

3.3 External damping paradox in the Pflüger column

The Ziegler double pendulum is usually considered as the two-dimensional analog of the Beck column, which is a cantilevered (visco)elastic rod loaded by a tangential follower force [2]. Strictly speaking, this analogy is not correct because the Beck column has a different mass distribution (the usual mass distribution of the Ziegler double pendulum is $m_1 = 2m_2$) and this mass distribution yields different limiting behavior of the stability threshold (Section 3.2). For this reason, in order to judge the stabilizing or destabilizing influence of external damping in the continuous case and to compare it with the case of the Ziegler double pendulum, it is correct to consider the Beck column with the point mass at the loaded end, in other words the so-called 'Pflüger column' [9].

A viscoelastic column of length l, made up of a Kelvin-Voigt material with Young modulus E and viscosity modulus E^*, and mass per unit length m is considered, clamped at one end and loaded by a tangential follower force P at the other end (Fig. 3.5(c)), where a point mass M is mounted.

The moment of inertia of a cross-section of the column is denoted by I and a distributed external damping is assumed, characterized by the coefficient K.

Small lateral vibrations of the viscoelastic Pflüger column near the undeformed equilibrium state is described by the linear partial differential equation [40]

$$EI\frac{\partial^4 y}{\partial x^4} + E^*I\frac{\partial^5 y}{\partial t \partial x^4} + P\frac{\partial^2 y}{\partial x^2} + K\frac{\partial y}{\partial t} + m\frac{\partial^2 y}{\partial t^2} = 0, \tag{3.21}$$

where $y(x,t)$ is the amplitude of the vibrations and $x \in [0,l]$ is a coordinate along the column. At the clamped end ($x = 0$) Eq.(3.21) is equipped with the boundary conditions

$$y = \frac{\partial y}{\partial x} = 0, \tag{3.22}$$

while at the loaded end ($x = l$), the boundary conditions are

$$EI\frac{\partial^2 y}{\partial x^2} + E^* I\frac{\partial^3 y}{\partial t \partial x^2} = 0, \quad EI\frac{\partial^3 y}{\partial x^3} + E^* I\frac{\partial^4 y}{\partial t \partial x^3} = M\frac{\partial^2 y}{\partial t^2}. \tag{3.23}$$

Introducing the dimensionless quantities

$$\begin{aligned} \xi = \tfrac{x}{l}, \quad \tau = \tfrac{t}{l^2}\sqrt{\tfrac{EI}{m}}, \quad p = \tfrac{Pl^2}{EI}, \quad \mu = \tfrac{M}{ml}, \\ \gamma = \tfrac{E^*}{El^2}\sqrt{\tfrac{EI}{m}}, \quad k = \tfrac{Kl^2}{\sqrt{mEI}} \end{aligned} \tag{3.24}$$

and separating the time variable through $y(\xi, \tau) = lf(\xi)\exp(\lambda\tau)$, the dimensionless boundary eigenvalue problem is obtained

$$\begin{aligned} (1+\gamma\lambda)\partial_\xi^4 f + p\partial_\xi^2 f + (k\lambda + \lambda^2)f &= 0, \\ (1+\gamma\lambda)\partial_\xi^2 f(1) &= 0, \\ (1+\gamma\lambda)\partial_\xi^3 f(1) &= \mu\lambda^2 f(1), \\ f(0) = \partial_\xi f(0) &= 0, \end{aligned} \tag{3.25}$$

defined on the interval $\xi \in [0, 1]$. A solution to the boundary eigenvalue problem (3.25) was found by Pedersen [41] and Detinko [40] to be

$$f(\xi) = A(\cosh(g_2\xi) - \cos(g_1\xi)) + B(g_1\sinh(g_2\xi) - g_2\sin(g_1\xi)) \tag{3.26}$$

with

$$g_{1,2}^2 = \frac{\sqrt{p^2 - 4\lambda(\lambda+k)(1+\gamma\lambda)} \pm p}{2(1+\gamma\lambda)}. \tag{3.27}$$

Imposing the boundary conditions (3.25) on the solution (3.26) yields the characteristic equation $\Delta(\lambda) = 0$ needed for the determination of the eigenvalues λ, where

$$\Delta(\lambda) = (1+\gamma\lambda)^2 A_1 - (1+\gamma\lambda)A_2\mu\lambda^2 \tag{3.28}$$

and

$$\begin{aligned} A_1 &= g_1 g_2 \left(g_1^4 + g_2^4 + 2g_1^2 g_2^2 \cosh g_2 \cos g_1 + g_1 g_2 (g_1^2 - g_2^2) \sinh g_2 \sin g_1\right), \\ A_2 &= (g_1^2 + g_2^2)\,(g_1 \sinh g_2 \cos g_1 - g_2 \cosh g_2 \sin g_1)\,. \end{aligned} \tag{3.29}$$

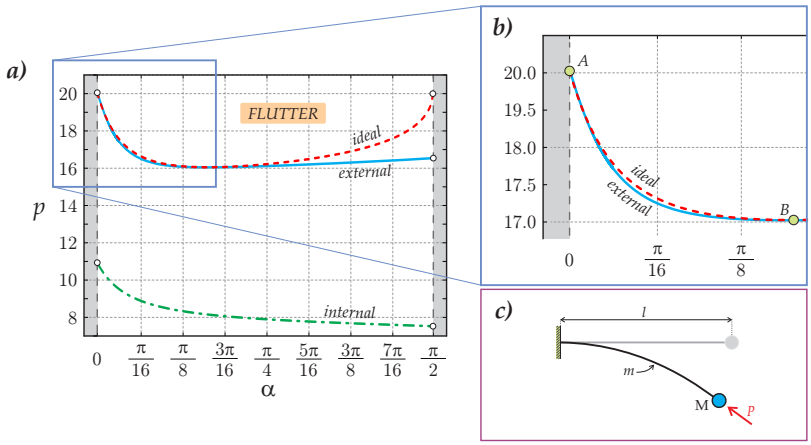

Figure 3.5: Analysis of the Pflüger column [scheme reported in (c)]. (a) Stability map for the Pflüger column in the load-mass ratio plane. The dashed/red curve corresponds to the stability boundary in the undamped case, the dot-dashed/green curve to the case of vanishing internal dissipation ($\gamma = 10^{-10}$ and $k = 0$) and the continuous/blue curve to the case of vanishing external damping ($k = 10^{-10}$ and $\gamma = 0$). (b) Detail of the curve reported in (a) showing the destabilization effect of external damping: small, but not null.

Transforming the mass ratio parameter in Eq.(3.28) as $\mu = \tan\alpha$ with $\alpha \in [0, \pi/2]$ allows the exploration of all possible ratios between the end mass and the mass of the column covering the mass ratios μ from zero ($\alpha = 0$) to infinity ($\alpha = \pi/2$). The former case, without end mass, corresponds to the Beck column, whereas the latter corresponds to a weightless rod with an end mass, which is known as the 'Dzhanelidze column' [11].

It is well-known that the undamped Beck column loses its stability via flutter at $p \approx 20.05$ [2]. In contrast, the undamped Dzhanelidze's column loses its stability via divergence at $p \approx 20.19$, which is the root of the equation $\tan\sqrt{p} = \sqrt{p}$ [11]. These values, corresponding to two extreme situations, are connected by a marginal stability curve in the (p, α)-plane that was numerically evaluated in [9, 11, 37, 41–43]. The instability threshold of the undamped Pflüger column is shown in Fig. (3.5) as a dashed/red curve.

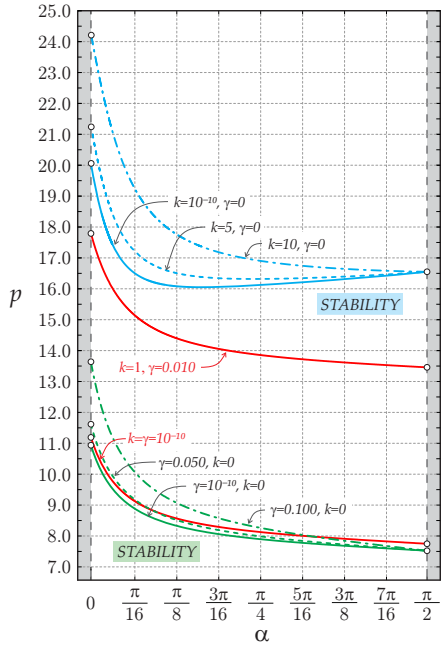

Figure 3.6: Evolution of the marginal stability curve for the Pflüger column in the (α, p) - plane in the case of $k = 0$ and γ tending to zero (green curves in the lower part of the graph) and in the case of $\gamma = 0$ and k tending to zero (blue curves in the upper part of the graph). The cases of $k = \gamma = 10^{-10}$ and of $k = 1$ and $\gamma = 0.01$ are reported with continuous/red lines.

For every fixed value $\alpha \in [0, \pi/2)$, the undamped column loses stability via flutter when an increase in p causes the imaginary eigenvalues of two different modes to approach each other and merge into a double eigenvalue with one eigenfunction. When p lies above the dashed/red curve, the double eigenvalue splits into two complex eigenvalues, one with the positive real part, which determines a flutter unstable mode.

At $\alpha = \pi/2$ the stability boundary of the undamped Pflüger column has a vertical tangent and the type of instability becomes divergence [11, 37, 42].

Setting $k = 0$ in Eq.(3.28) the location in the (α, p)-plane of the marginal stability curves can be numerically found for the viscoelastic Pflüger column without external damping, but for different values of the coefficient of internal damping γ, Fig. 3.6(a). The thresholds tend to a limit which does not share common points with the stability boundary of the ideal column, as shown in Fig. 3.5(a), where this limit is set by the dot-dashed/green curve.

The limiting curve calculated for $\gamma = 10^{-10}$ agrees well with that obtained for $\gamma = 10^{-3}$ in [21, 43]. At the point $\alpha = 0$, the limit value of the critical flutter load when the internal damping is approaching zero equals the well-known value for the Beck column, $p \approx 10.94$. At $\alpha = \pi/4$ the limiting value becomes $p \approx 7.91$, while for the case of the Dzhanelidze column $(\alpha = \pi/2)$ it becomes $p \approx 7.49$.

An interesting question is what is the limit of the stability diagram for the Pflüger column in the (α, p)-plane when the coefficient of internal damping is kept null $(\gamma = 0)$, while the coefficient of external damping k tends to zero.

The answer to this question was previously known only for the Beck column $(\alpha = 0)$, for which it was established, both numerically [31, 34] and analytically [44], that the flutter threshold of the externally damped Beck column is higher than that obtained for the undamped Beck column (tending to the ideal value $p \approx 20.05$, when the external damping tends to zero). This very particular example was at the basis of the common and incorrect opinion (maintained for decades until now) that the external damping is only a stabilizing factor, even for non-conservative loadings. Perhaps for this reason the effect of the external damping in the Pflüger column has, so far, simply been ignored.

The evolution of the flutter boundary for $\gamma = 0$ and k tending to zero is illustrated by the blue curves in Fig. 3.6. It can be noted that the marginal stability boundary tends to a limiting curve which has two common tangent points with the stability boundary of the undamped Pflüger column, Fig. 3.5(b). One of the common points, at $\alpha = 0$ and $p \approx 20.05$, marked as point A, corresponds to the case of the Beck column. The other corresponds to $\alpha \approx 0.516$ and $p \approx 16.05$, marked as point B. Only for these two 'exceptional' mass ratios the critical flutter load of the externally damped Pflüger column coincides with the ideal value when $k \to 0$. Remarkably, for all other mass ratios the limit of the critical flutter load for the vanishing external damping is located *below* the ideal value, which means that the Pflüger column fully demonstrates the *destabilization paradox due to vanishing external damping*, exactly as it does in the case of the vanishing internal damping, see Fig. 3.5(a), where the two limiting curves are compared.

Note that the discrepancy in case of vanishing external damping is smaller than in case of vanishing internal damping, in accordance with the analogous result that was established in Section 3.2 for the Ziegler double pendulum with arbitrary mass distribution. As for the discrete case, also for the Pflüger column the flutter instability threshold calculated in the limit when the external damping tends to zero has only two common points with the ideal marginal stability curve. The discrepancy is the most pronounced for the case of Dzhanelidze column at $\alpha = \pi/2$, where the critical load drops from $p \approx 20.19$ in the ideal case to $p \approx 16.55$ in the case of vanishing external damping.

4

The flutter machine

> I never satisfy myself until I can make a mechanical model of a thing. If I can make a mechanical model, I understand it.
>
> *W. Kelvin*

Flutter instability in elastic structures subject to follower load, the most important cases being the famous Beck and Pflüger columns (two elastic rods in a cantilever configuration, with an additional concentrated mass at the end of the rod in the latter case), have attracted, and still attract, a thorough research interest. In this field, the most important issue is the validation of the model itself of follower force, a nonconservative action which was harshly criticized and never realized in practice for structures with diffused elasticity. An experimental setup to introduce follower tangential forces at the end of an elastic rod was designed, realized, validated, and tested, in which the follower action is produced by exploiting Coulomb friction on an element (a freely-rotating wheel) in sliding contact against a flat plate (realized by a conveyor belt). It is therefore shown that follower forces can be realized in practice and the first experimental evidence is given of the flutter and divergence

instability in the Pflüger column. Load thresholds for the two instabilities are for the first time measured. Moreover, the detrimental effect of dissipation on the critical load for flutter is experimentally demonstrated. The presented approach to follower forces discloses new horizons for testing self-oscillating structures and for exploring and documenting dynamic instabilities possible when nonconservative loads are applied.

4.1 The need of a new experimental set-up

Many articles have been written after Pflüger [8, 9], Ziegler [1, 6, 7], Beck [2], and Bolotin [11] have initiated the study of structures subject to follower tangential loads. This topic is of great interest not only in structural mechanics, but also in rotordynamics and gyrodynamics, in automatic control, aeroelasticity, fluid-structure interaction and even in astrophysics and geophysics.

Flutter instability, a dynamical instability which passes undetected using static methods, is a phenomenon that can affect structures loaded with follower forces. In fact, these forces can in certain circumstances provide energy to the elastic system to which they are applied, so that a blowing-up oscillation is produced, which eventually leads to a periodic self-oscillation mode. In this context, stability is affected by dissipation in a detrimental way, so that even a vanishing small viscosity can produce a strong (and finite) decrease in the flutter load evaluated without keeping damping into consideration, a counter-intuitive effect known as the 'Ziegler paradox'.

The most important problem emerged from the beginning of the research on flutter instability is the concept itself of a follower force, which has been often questioned and denied, up to the point that Koiter [24] proposed the *"elimination of the abstraction of follower forces as external loads from the physical and engineering literature on elastic stability"* and claimed *"beware of unrealistic follower forces"*. If follower forces could not be realized in practice, all the theoretical findings, including dissipative instabilities and the Ziegler paradox, would become mere mathematical curiosities without any specific interest. For this reason, experiments were attempted from the

very beginning and developed in two directions, namely, using water or air flowing from a nozzle (Herrmann [17, 45], Wood [19], Prasad [20]), or using a solid motor rocket (Sugiyama [21]) to produce a follower force at the end of an elastic rod or of a Ziegler double pendulum. Neither of these methods was capable of exactly realizing a tangential follower force, in the former case because of hydrodynamical effects influencing the motion of the rod (due to the Coriolis force that arise when the governing differential equation of a uniform pipe is written) and in the latter because of the non-negligible and variable mass of the rocket, which burns so fast (just few seconds) that a long-term analysis of the motion is prevented. The fact that a follower, tangential force was never properly realized is clearly put in evidence in the thorough review by Elishakoff [23].

A significant breakthrough was achieved by Bigoni [22], who designed and tested a device capable of realizing a follower tangential force emerging at the contact with friction of a wheel constrained to slide against a moving surface. The device was successfully applied to the Ziegler double pendulum, but not to cases of diffuse elasticity, because difficulties related to early flexo-torsional buckling occurring in the structure prevented the use of the experimental setup. Therefore, the important cases of the Beck and Pflüger columns remained so far unexplored till nowadays. The goals of the present chapter are:

- to extend the experimental investigation [22] to continuous elastic systems (in particular the Pflüger column) through the design, realization and testing of a new mechanical apparatus to generate follower forces from friction. An example of the Pflüger column during a flutter (left) and a divergence (right) experiment is shown in stroboscopic photos reported in Fig. 4.1;

- to provide another experimental evidence on the relation between Coulomb friction and dynamical instabilities occurring now in a deformable system with diffused elasticity;

- to document (theoretically and experimentally) the existence of divergence instability occurring at loads higher than those for flutter for

the Pflüger column, an instability never addressed before;

- to experimentally demonstrate that the introduction of damping lowers the critical load for flutter and increases the critical load for divergence (when this occurs at loads higher than those for flutter), thus demonstrating the concept of dissipation-induced instability by dissipation-induced instability by Kelvin [46], see Krechetnikov [28] and Kirillov [29];

- to prove that, as a consequence of dissipation and nonlinearities, the systems, both in flutter and in divergence conditions, eventually attain a limit cycle in which a self-oscillating structure is obtained, in the sense explained by Jenkins [47].

The presented results: (i.) show that concepts related to follower forces correspond to true physical phenomena, and give an answer to Doak [24] (ii.) open new and unexpected possibilities to test the dynamical behaviour of structures under nonconservative loads (which include for instance the instability of a rocket subject to variable trust, the possibility of simulate aeroelastic effects without a wind tunnel, or to investigate the interactions between mechanical components with friction), as hoped by Elishakoff [23].

The Chapter is organized as follows, Section 4.2 is devoted to the design and realization of the 'flutter machine', whereas Section 4.3 gathers the comparisons between experiments and both theoretical and numerical results. The theoretical approach to the Pflüger column (of which the Beck column is a particular case) and the identification of the parameters of the models of samples tested are deferred to Appendix B.1 and B.2 respectively. The theory of the modified logarithmic decrement approach used in the parameters identification procedure is reported in B.3.

4.2 Design and validation of the flutter machine

A new mechanical device, nicknamed 'flutter machine', has been designed and realized to induce follower loads through friction at given points

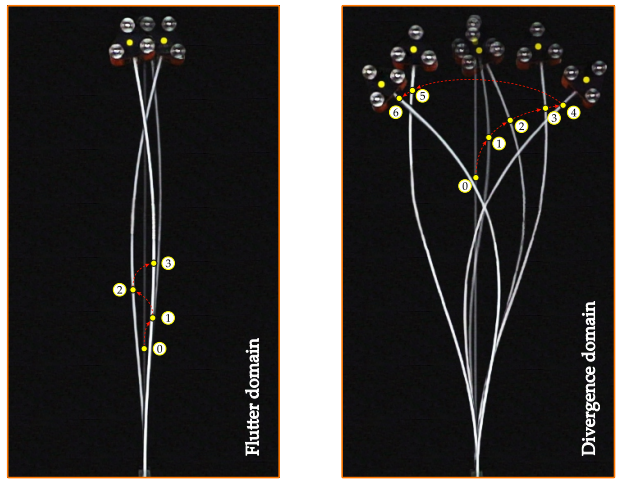

Figure 4.1: Stroboscopic photographs (taken with a Sony PXW-FS5 camera at 240 fps) of the initial motion of the Pflüger column when flutter instability (left) or divergence (right) occurs. The elastic rod corresponds to sample 5 of Table 4.1. A vertical load of 6.5 N (40.0 N) was applied for flutter (for divergence) and the conveyor belt was running at 0.1 m/s. Note the different shape of the deformed rods at the beginning of the instability and their evolution towards a limit-cycle oscillation.

of an elastic system, which is now identified with either the Beck or Pflüger column. The working principle of the device is sketched in Fig. 4.2 as a development of the idea by Bigoni [22] and is based on the friction that arises at the contact between a freely-rotating wheel and a moving surface. The wheel realizes a highly-anisotropic Coulomb friction, so that, in principle, only a force parallel to the wheel axis is produced (P_{tang} in the figure). While the stroke of the device used for testing the Ziegler double pendulum was limited to about 1 m, the new device realizes a virtually infinite stroke, because the sliding surface is obtained by means of a conveyor belt (C8N, from Robotunits). In this way, experiments of any time duration can be performed. A structure under test can be fixed at one end to a loading frame mounted across the moving belt, while subject at the other end to

the follower force, which is transmitted to the structure through a 'loading head' (realized in PLA with a 3D printer from GiMax 3D) endowed with the above-mentioned wheel (a ball bearing from Misumi-Europe). The loading head can be weighted with additional masses in order to obtain different ratio between the end mass and the distributed mass of the sample employed.

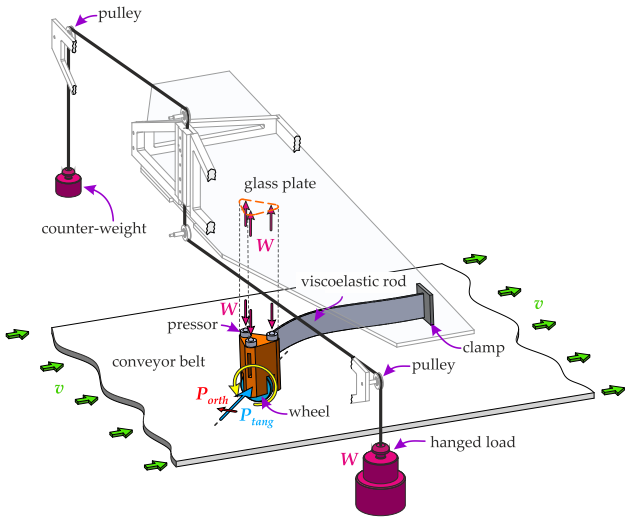

Figure 4.2: The working principle of the 'flutter machine': a freely-rotating wheel is constrained to slide with friction against a moving substrate. The wheel is contained in a 'loading head' endowed with a miniaturized load cell (used to measure the follower force) and a miniaturized accelerometer. The head is pressed vertically against the conveyor belt by a glass plate, indirectly loaded through a pulley system subject to a weight. A change in the applied weight leads, according to the law of Coulomb friction, to a change in the tangential force applied to the viscoelastic rod.

Measurement of the follower force is achieved by means of a miniaturized load cell (XFTC301 from TE connectivity) mounted inside the 'loading head' together with a miniaturized accelerometer (352A24 from PCB Piezotronics). As regards the loading head, this can be modelled as a point

mass which cannot be reduced to zero in practice, so that the Pflüger column, rather than the Beck column, can be realized. The amount of the follower force can be calibrated as proportional, through Coulomb friction law, to a vertical load pressing the head against the conveyor belt (W in the figure). This load is provided through contact of the head (on which three pressors are mounted to minimize friction, thus leaving the head free of moving) with a 5 mm thick tempered glass plate, which is in turn loaded through a weight (a tank filled with water) indirectly applied by means of a double-pulley system. The pulley system is made in such a way that it can completely compensate for the weight of the loading frame, so that any vertical load can be applied starting from zero.

Note that the loading system of the rod's head is one of the most important design differences with respect to the earlier testing apparatus realized in 2011. In fact, in the previous apparatus the amount of the follower load was controlled by exploiting the structure under testing as a lever, so that the setup was useful only for discrete structures (e.g., the Ziegler double pendulum) which, having an infinite torsional stiffness, do not display flexo-torsional instability. Hence, the design of the 'flutter machine' was driven by the aim to overcome such limitation and extend the experimental study of flutter and divergence instability to structural systems with diffused elasticity.

Experimental results collected by exploiting the 'flutter machine' will be presented in the following Sections together with theoretical predictions. All the data from the load cell and from the accelerometer were acquired with a NI cDaq-9172 system (from National Instruments) interfaced with LabVIEW 13. Also, the conveyor belt was actuated with a SEW-Eurodrive motor and controlled with an inverter (E800 from Eurodrive), so that its velocity could range between 0 and 0.3 m/s. As regards the viscoelastic rods that model the Pflüger column, these were realized in polycarbonate (white 2099 Makrolon UV from Bayer of Young's modulus $E \simeq 2344\,\mathrm{MPa}$, Poisson's ratio $\nu = 0.37$ and volumetric mass density $m \simeq 1185\,\mathrm{kg\,m^{-3}}$). In order to measure the reaction force at the clamped extremity of the tested rods, this was endowed with a load cell (OC-K5U-C3 from Gefran). A photograph of the experimental setting is reported in Fig. 4.3 together with

a detailed view of the loading head.

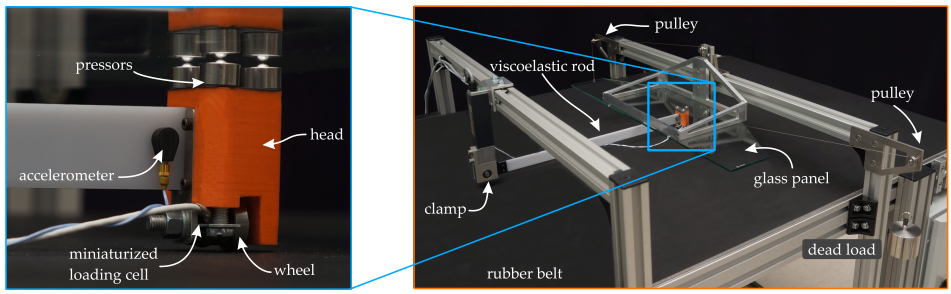

Figure 4.3: A photograph of the 'flutter machine' (on the right) showing the conveyor rubber belt and the viscoelastic rod connected at one end to a load cell and to the head transmitting the follower force at the other end. Modulation of the follower force is achieved by varying the vertical load acting on the head and transmitted through contact with a glass plate. Notice the double-pulley loading system. A detail is reported (on the left) of the head introducing the follower force to the end of the Pflüger column. The upper edge of the head is in contact through three pressors with the glass plate transmitting the vertical load, while its lower edge contains the wheel sliding against the conveyor belt. The head contains a miniaturized load cell to measure the follower force, and a miniaturized accelerometer is mounted near the head.

Assuming perfect transmission of loads, perfect sliding with ideal Coulomb friction at the wheel contact, and null spurious frictional forces, a purely tangential follower load should be generated at the end of the Pflüger column. However, for practical reasons the 'flutter machine' is not capable of perfectly realizing such an ideal condition and discrepancies can arise from different sources, the most important of which are:

1. imperfect transmission of the vertical force W at the loading head;
2. friction at the glass plate/pressors contact;
3. generation of a spurious force orthogonal to the tangent to the rod at its end, due to the non-negligible rolling friction of the wheel and its (small) inertia;

4. deviation from the simple law of Coulomb friction at the sliding contact between the steel wheel and the rubber conveyor belt, so that the friction coefficient depends on:

   4.1. the vertical load applied to the wheel;

   4.2. the relative velocity between the end of the rod and the conveyor belt.

All of the above-listed discrepancies have been subject to experimental investigation and the results are summarized in the following.

4.2.1 Transmission of W

Imperfect transmission of the vertical load W at the head of the elastic rod. To evaluate the performance of the load transmission system against the pressors mounted on the head of the elastic rod, a load cell has been placed between the glass plate and the belt. The load transmission mechanism was found to be almost perfect and insensitive to the position of the head on the glass plate, so that the mechanical components of the double-pulley loading system do not introduce any significant friction.

4.2.2 Friction at the glass plate/pressors contact

The three steel pressors at the glass plate/head contact introduce a spurious friction in the system, that has been measured and found to be negligible.

4.2.3 Inclined follower force P

A departure from the pure tangentiality of the follower force is due to rolling friction and inertia of the wheel, and determines a non-null component of the follower load orthogonal to the tangent to the rod at its end, i.e. P_{orth} in Figs. 4.2 and 4.4. This component, which adds to the tangential force P_{tang}, was directly measured with a load cell (XFTC301 from TE connectivity) using a rigid bar (instead of the deformable rod employed

in the experiments) during sliding of the belt against the wheel. Different inclinations of the rod (15°, 30°, 45° and 60°) were investigated for several applied vertical loads, see Fig. 4.4. With these experiments the ratio between the orthogonal and tangential components of the load, namely, $v'(l)\bar{\chi} = \arctan(P_{orth}/P_{tang})$, where $\bar{\chi} = 1 - \chi$ and $v'(l)$ is the derivative of the rod's deflection at its end, was experimentally estimated. In particular, the mean value of $v'(l)\bar{\chi} = 0.092$ was established.

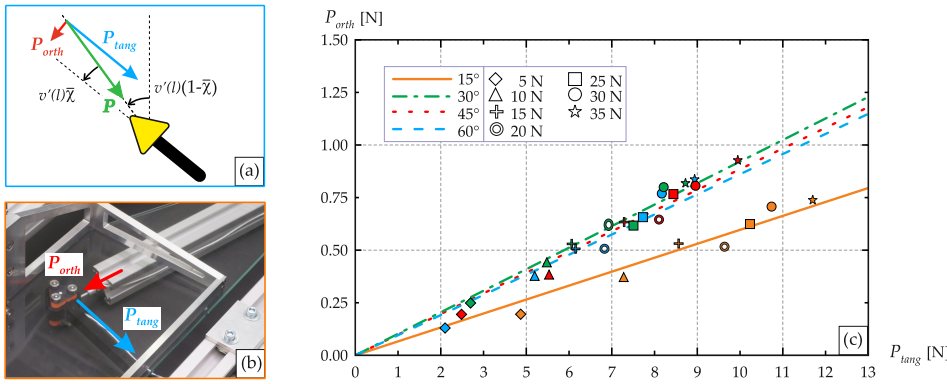

Figure 4.4: (a) A sketch of the tangential, P_{tang}, and orthogonal, P_{orth}, components of the follower force P acting at the end of the rod. (b) A photograph of the experimental setting exploited to measure the two components of the follower force P. Specifically, the tangential component is measured with the load cell inside the head, whereas the orthogonal component is measured with an external load cell. (c) Tangential and orthogonal components of the follower force P acting on the loading head as measured for different vertical loads W and different inclinations of the rod. Best fitting lines are reported for the distinct inclinations of the rod, leading to a mean value of $v'(l)\bar{\chi} = \arctan(P_{orth}/P_{tang}) = 0.092$.

4.2.4 Friction at the steel/rubber contact

The deviation from the simple law of Coulomb friction at the sliding contact between the steel wheel and the rubber conveyor belt depends on two main factors: vertical load applied W and running velocity of the con-

veyor belt. In fact the law of Coulomb friction at the wheel/conveyor belt contact holds only as a first approximation. The coefficient of friction was found experimentally to be a function of the vertical load applied to the head. The dependence of the friction coefficient upon the vertical load W was investigated with a rigid rod replacing the viscoelastic rod. During experimentation, the velocity of the belt was kept constant at 0.1 m/s. Experimental results are reported in Fig. 4.5(a) together with their interpolation

$$\mu_0(W) = -2.406 + 0.013W + (0.288 + 0.0039W)^{-1}, \tag{4.1}$$

which was used in the modelling. Notice that a nonlinearity of the friction coefficient at a rubber/steel contact (the belt is made of rubber) was previously documented by Maegawa [48].

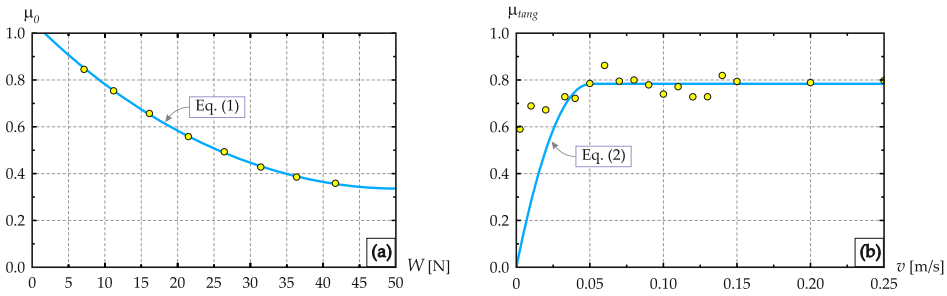

Figure 4.5: (a) Dependence of the dynamic friction coefficient μ_0 at the wheel/belt contact on the applied vertical load W for a fixed velocity of the belt, namely 0.1 m/s. The experimental data (yellow spots) are fitted with the non-linear interpolation of Eq.(4.1). (b) Dependance of the dynamic friction coefficient μ_{tang} at the wheel/belt contact on the velocity of the belt for a fixed vertical load $W = 10$ N. The experimental data (yellow spots) follow the law proposed by Oden (1985) and Martins (1990), that is Eq.(4.2).

Moreover, the friction coefficient is sensitive to the sliding velocity at the wheel/belt contact and exhibits a nonlinear behaviour characterized by an increase with velocity and later a stabilization, which occurs from approximately 0.05 m/s. The dependence of the friction coefficient on the velocity

was measured (at a constant vertical load of 10 N) with the experimental setup used to address point (4.1), and found to follow the law provided by Oden [49] and Martins [50]. In particular, with reference to the friction coefficient $\mu_0(W)$ introduced in equation (4.1), the tangential coefficient of friction determining the relation between the follower force P_{tang} and the weight W as $P_{tang} = \mu_{tang} W$ can be written in the form

$$\mu_{tang} = \mu_0(W) \begin{cases} \operatorname{sgn}(v_{tang}) & \text{if } v_{tang} \notin [-\varepsilon, \varepsilon] \\ \left(2 - \dfrac{|v_{tang}|}{\varepsilon}\right) \dfrac{v_{tang}}{\varepsilon} & \text{if } v_{tang} \in [-\varepsilon, \varepsilon] \end{cases} \tag{4.2}$$

where v_{tang} is the tangential component of the wheel/belt relative sliding velocity and $\varepsilon = 0.05\,\mathrm{m/s}$ is a parameter. The correspondence between experiments and the law of equation (4.2) is reported in Fig. 4.5(b). In view of the experimental results reported in Fig. 4.4, the coefficient μ_{orth} is defined by the same equation (4.2), but with a value of the dynamic friction coefficient equal to $0.09\mu_0$ and with the velocity v_{orth} replacing v_{tang}.

4.3 Experiment vs theory

In the present Section we provide a detailed analysis of the results obtained by means of the experimental setting introduced in Section 4.2. While the onset of flutter and divergence instability can be accurately predicted via a theoretical study of the governing equations in their linearized form, a computational approach is needed to capture the nonlinear dynamics of the system when large displacements and rotations occur.

4.3.1 Onset of flutter and divergence with dampings

The theoretical approach to the Beck and Pflüger columns, when both the internal and external dissipations are present, is based on the analysis of an axially pre-stressed, rectilinear and viscoelastic rod, characterized by the

transversal deflection $v(x,t)$, function of the axial coordinate x and of time t. A moment-curvature viscoelastic constitutive relation of the Kelvin-Voigt type is assumed in the form

$$\mathcal{M}(x,t) = -EJv''(x,t) - E^*J\dot{v}''(x,t), \tag{4.3}$$

where a superimposed dot denotes the time derivative and a prime the derivative with respect to the coordinate x, E and E^* are the elastic and the viscous moduli, respectively, and J is the moment of inertia of the rod. The shear force $\mathcal{T}(x)$ can be computed as the derivative of the bending moment, so that for constant moduli E and E^*, it can be written as

$$\mathcal{T}(x,t) = -EJv'''(x,t) - E^*J\dot{v}'''(x,t). \tag{4.4}$$

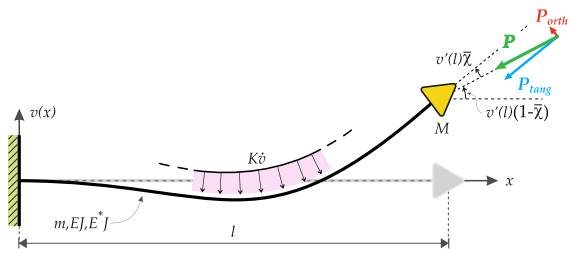

Figure 4.6: Structural model for the Pflüger column: a viscoelastic cantilever rod (of length l, mass per unit length m, and elastic and viscous bending stiffnesses EJ and E^*J, respectively) with a concentrated mass M at its free end is loaded by a partially tangential follower load P.

The linearized differential equation of motion which governs the dynamics of a rectilinear viscoelastic rod, loaded by an axial force P (positive when compressive) and a transversal distributed load proportional through a coefficient K to the velocity $\dot{v}$ (which models for instance the air drag) is

$$EJv''''(x,t) + E^*J\dot{v}''''(x,t) + Pv''(x,t) + K\dot{v}(x,t) + m\ddot{v}(x,t) = 0, \tag{4.5}$$

where m is the mass density of the rod per unit length, see Fig. 4.6.

The solution to the Pflüger column problem (of which the Beck column is a particular case) is obtained by imposing on the differential equation (4.5) the following boundary conditions

$$\begin{aligned} &v(0,t) = v'(0,t) = 0, \\ &\mathcal{M}(l,t) = -J[Ev''(l,t) - E^*\dot{v}''(l,t)] = 0, \\ &\mathcal{T}(l,t) = -J[Ev'''(l,t) - E^*\dot{v}'''(l,t)] = P\bar{\chi}v'(l,t) - M\ddot{v}(l,t), \end{aligned} \tag{4.6}$$

where $\bar{\chi}$ measures the inclination of the applied tangential force P, such that $\bar{\chi} = 0$ corresponds to a purely tangential follower load. Notice that the Beck column problem is obtained by setting $M = 0$. By introducing the dimensionless quantities

$$\begin{aligned} &\xi = \tfrac{x}{l}, \qquad &&\tau = \tfrac{t}{l^2}\sqrt{\tfrac{EJ}{m}}, \qquad &&p = \tfrac{Pl^2}{EJ}, \\ &\alpha = \arctan\left(\tfrac{M}{ml}\right), \quad &&\eta = \tfrac{E^*}{El^2}\sqrt{\tfrac{EJ}{m}}, \quad &&\gamma = \tfrac{Kl^2}{\sqrt{mEJ}}. \end{aligned} \tag{4.7}$$

the governing Eq.(4.5) can be rewritten as

$$v''''(\xi,\tau) + \eta\dot{v}''''(\xi,\tau) + pv''(\xi,\tau) + \gamma\dot{v}(\xi,\tau) + \ddot{v}(\xi,\tau) = 0, \tag{4.8}$$

where now a prime denotes differentiation with respect to ξ and a dot differentiation with respect to τ. It is now expedient to assume time-harmonic vibrations of dimensionless pulsation ω as

$$v(\xi,\tau) = \tilde{v}(\xi)\exp(\omega\tau), \tag{4.9}$$

such that Eq.(4.8) is transformed into a linear differential equation for $\tilde{v}(\xi)$, which can be solved in an explicit form. Specifically, imposition of the boundary conditions (4.6), transformed via Eqs.(4.7)-(4.9), yields an

eigenvalue problem for the pulsation ω, which can be solved for given values of: (i.) dimensionless load p, (ii.) mass contrast α, (iii.) rod viscosity η, (iv.) external damping γ modelling the air drag, and (v.) inclination of the load χ. The details of this analysis are deferred to B.1.

The stability of the structure can be judged on the basis of the nature of the pulsation ω. In particular, the system is unstable when the real part of the pulsation is positive, $\mathrm{Re}[\omega] > 0$; in this case flutter instability occurs when ω is complex with non vanishing imaginary part, whereas the system becomes unstable by divergence when ω is purely real and positive. In view of this, flutter corresponds to a blowing-up oscillation, whereas divergence to an exponential growth.

The eigenmodes associated to flutter instability and divergence instability can be found from the eigenvectors of matrix (B.5), once the critical pulsation ω has been determined. As an example, referred to sample 5 of Table 4.1, two eigenmodes, one corresponding to flutter instability (6.5 N of applied vertical load) and the other to divergence instability (40.0 N of applied vertical load) are reported in Fig. 4.7, together with two photos taken during experimentation.

Note the difference between the shapes of the two modes and the remarkable correspondence with the photos, which correspond to the onset of the two motions shown in Fig. 4.1. The difference in the shape of the modes for flutter and for divergence has been used during the experiments to discriminate between the two instabilities (see the following discussion).

Dissipation has a complex effect on flutter and divergence instability. Recalling what already exposed in Chapters 2 and 3, a vanishing damping has a strong detrimental effect on the flutter threshold, the so-called *Destabilization paradox*, found for the first time by Ziegler [1] (rearding the internal damping) and recently by Tommasini [51]. A map of the real and imaginary parts of the pulsation ω as functions of the applied (dimensionless) load p is provided in Fig. 4.8, which refers to both the 'ideal' case in which all dissipation sources are set to zero (on the left) and to the damped case in which both internal and external dissipation are present (on the right). The figure, relative to sample 8 of Table 4.1 , confirms the fact that the flutter load is strongly decreased by dissipation, while the divergence

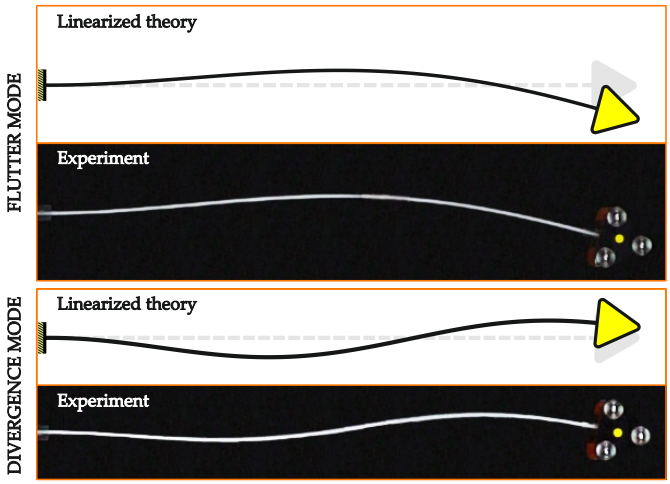

Figure 4.7: Eigenmodes associated to flutter instability (upper part) and divergence instability (lower part) compared with two photographs referred to two experiments performed on sample 5 of Table 4.1.

load is slightly increased. This effect is more pronounced when internal and external dampings are both increased.

Such a destabilizing effect was experimentally explored only quite recently, see Chapter 5 for details, so that this verification is strongly connected with the proper identification of all damping sources. In the following, the experiments are described in which the parameters governing flutter and divergence are varied in a way that the effect of damping can be assessed.

The behaviour of the Pflüger column was experimentally investigated covering a wide range of values of the ratio between the concentrated mass M at the free end of the column and the mass of the column ml, expressed through the parameter α ranging in the experiments between 0.7019 and 1.4256 for the eleven tested rods, see Table 4.1. The velocity of the belt was maintained constant during all the experiments and equal to 0.1 m/s. To measure the critical load for flutter with high precision, the system was

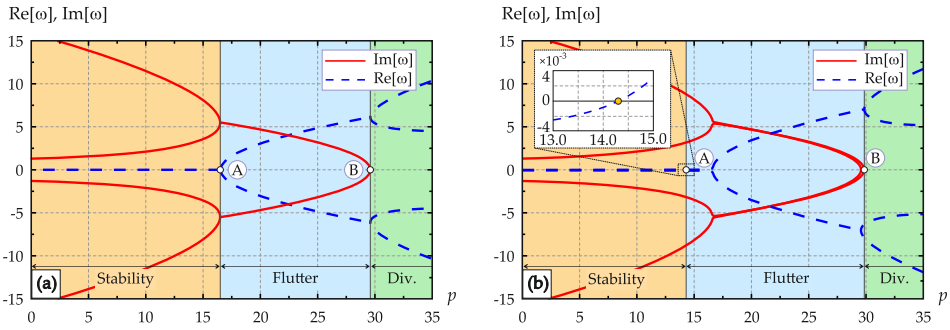

Figure 4.8: Branches of the real Re[ω] and imaginary Im[ω] parts of the pulsation ω defining the vibration of the Pflüger column, with a mass ratio $\alpha = 0.9819$ and an inclination of the end force $v'(l)\bar{\chi} = 0.092$. The ideal case (absence of damping) is reported on the left (a), where flutter (marked with the letter A) occurs at $p = 16.499$ and divergence (marked with the letter B) at $p = 29.597$. The case in which both the external and internal dampings are present (with coefficients corresponding to our experimental setup, i.e. $\eta = 0.348 \cdot 10^{-3}$ and $\gamma = 50.764 \cdot 10^{-3}$) is shown on the right (b). Here, the flutter load decreases to $p = 14.318$, while the divergence load increases to $p = 29.575$. Flutter occurs when a real branch of the pulsation ω becomes positive (with non zero values of the imaginary part of the pulsation).

loaded by filling a container with water, so that an accuracy of one gram was achieved.

Before proceeding with the presentation of the results, notice that, since the experiments were performed for rods of six different lengths, namely $L = \{250, 300, 350, 400, 550, 800\}$ mm, these correspond to different flutter and divergence boundaries in a (p, α) - plane, except for the ideal case (in which sources of damping are absent), where only a continuous curve arises. Therefore, when all the results are reported in the same graph, the relevant theoretical curves for flutter and divergence appear fictitiously discontinuous. The discontinuities are clearly visible for flutter when both the damping sources are introduced, but these become hardly visible when only one damping is present or for divergence.

Theoretical predictions and experimental results are reported in Fig. 4.9

Sample	b [mm]	h [mm]	L [mm]	M [kg]	α [-]	η [$\times 10^{-3}$]	γ [$\times 10^{-3}$]
1	1.90	24	250	0.105	1.426	1.059	24.705
2	1.90	24	250	0.075	1.369	1.059	24.705
3	1.90	24	250	0.060	1.320	1.059	24.705
4	1.90	24	300	0.060	1.280	0.746	36.056
5	1.92	24	350	0.060	1.236	0.557	48.368
6	1.95	24	400	0.060	1.196	0.439	62.128
7	2.98	24	550	0.089	1.063	0.348	50.764
8	2.98	24	550	0.075	0.982	0.348	50.764
9	3.07	24	800	0.089	0.903	0.177	102.538
10	3.07	24	800	0.075	0.813	0.177	102.538
11	3.07	24	800	0.060	0.702	0.177	102.538

Table 4.1: Geometrical parameters and dimensionless coefficients for internal and external viscosity of the different structures tested with the 'flutter machine'.

in terms of the dimensionless load p as a function of mass-ratio parameter α. In the figures, numbers identify the specific sample tested (the characteristics of the samples are reported in Table 4.1).

For conciseness, all the experimental data are reported in the figures, where 'pieces' of the relevant theoretical curves have been plotted for comparison (marked with different colors in the figure). The ideal case is also included (dashed). Fig. 4.9(b) is a detail of Fig. 4.9(a) to highlight the flutter threshold, which is reported and compared to the theoretical curves relative to the presence of both damping sources and only one of them (either internal or external). It is visible that only when the two sources of dissipation act simultaneously the theoretical predictions fit correctly the experiments.

It has to be noted that the loads for the onset of flutter were measured simply observing oscillations of the rod with deviations from rectilinearity of the structure, whereas the loads for the onset of divergence have been detected on the basis of the modes of vibrations, a circumstance which

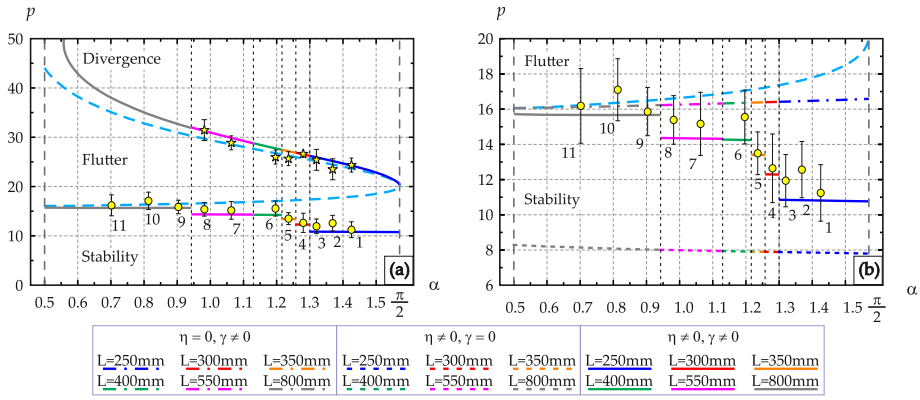

Figure 4.9: (a) Dimensionless critical load p for flutter and divergence instability versus the mass ratio parameter α. Experimental results are shown (spots and stars with error bars) together with theoretical predictions. The latter are reported for the ideal case (where damping is assumed to be absent) with a dashed curve and when both damping sources are present (solid curves). The different colors and the numbers identify the different samples tested (see Table 4.1 for details). (b) Detail of the flutter boundary, considering only internal damping (dotted curves), only external damping (dash-dotted curves) or both of them (solid curves). All the theoretical curves were computed considering that the load is not purely tangential ($v'(l)\bar{\chi} = 0.092$). The experimental results confirm the decrease (the increase) of the critical load for flutter (for divergence) due to the effect of dissipation.

merits the following clarification.

The *linearized* equations of motion show that the instabilities of flutter and divergence are both characterized by an exponential growth in time of displacements (though the former is also accompanied by oscillations), which rapidly leads to a large amplitude motion and thus to a departure from the applicability of a linear theory. For the Ziegler double pendulum, both the experiments and the theoretical calculations show that the structure reaches a limit cycle when nonlinearities dominate [22]. While these experiments clearly reveal the flutter instability threshold, the discrimination between flutter and divergence becomes difficult, because oscillations are experimentally found at every load beyond flutter and in all cases a

limit cycle vibration is observed. This circumstance can be understood because quasi-static solutions are impossible for the Pflüger rod, so that an exponential growth should always 'come to an end' for a real system, in which displacements are necessarily limited. Therefore, oscillatory behaviour becomes in a sense necessary, and in fact was always observed in *both* the experiments and the numerical simulations (which will presented in subsection 4.3.2).

As a conclusion, a discrimination between flutter and divergence cannot be simply based of the fact that oscillations do not occur for the latter case, which represents only the prediction of a linearized model. Divergence instability (never experimentally investigated before) is discriminated from flutter on the basis of the deformation of the rod at the onset of the instability, see Fig. 4.7. Therefore, to detect divergence instability, high-speed videos at 240 fps were taken (with a Sony high-speed camera, model PXW-FS5) and the motion of the rod at the beginning of the instability monitored.

The experimental results obtained for flutter instability and shown in Fig. 4.9 lead to the important conclusion that *damping decreases the flutter load*, an effect previously never experimentally documented. Damping has much less influence on the divergence load than on the flutter load, so that it is harder to conclude on this. Nevertheless, the experiments reported in Fig. 4.9 are in agreement with the conclusion that viscosity produces a shift of divergence towards higher loads.

The variation of the dimensionless critical frequency for flutter with the mass ratio α (ranging between 0.5 and $\pi/2$) is reported in Fig. 4.10. This behaviour was previously analyzed by Pedersen [41], by Chen [52], and by Ryu [43], but only theoretically and without considering external and internal damping separately. Experiments, and therefore also theoretical predictions, are reported in Fig. 4.10 for different lengths of the rod, so that, while the theoretical predictions for the ideal case (without damping) describe a continuous curve (dashed light blue), the cases where damping is present evidence fictitious discontinuities (the discontinuities occurring only when one damping is present are so small that they are not visible in the graphs). The situations in which either the internal or the external damping is considered separately correspond to the dotted and dot-dashed curves,

respectively, whereas both sources of damping were taken into account to generate the discontinuous curve. The vertical bars and different colors denote the intervals corresponding to different lengths.

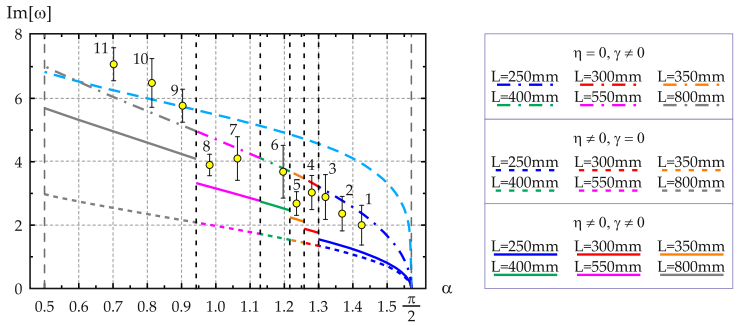

Figure 4.10: Imaginary part of the dimensionless critical pulsations for flutter $\mathrm{Im}[\omega]$ as a function of the mass ratio α. Experiments are reported against different theoretical predictions. The latter are for the ideal case (without damping, dashed light blue curve), for the case with only internal (dotted curves) and only external (dot-dashed curves) damping and with both dampings (solid curves). The colors and numbers identify the different samples tested (see Table 4.1 for details). All the curves were computed considering that the load is not purely tangential ($v'(l)\bar{\chi} = 0.092$).

4.3.2 Nonlinear dynamics of the Pflüger column

It has been already highlighted that, while the linearized theory predicts the exponential growth of divergence to occur at vanishing frequency, in reality limit cycle oscillations always occur. In fact, indefinite exponential growth is impossible in a real system and quasi-static solutions are impossible for the Pflüger rod. Hence, the discrimination between the two instabilities of flutter and divergence requires a numerical investigation in the full nonlinear range, which is presented below.

With the purpose of simulating the behaviour of the Pflüger column beyond the flutter threshold, a nonlinear computational model was devised and implemented in the commercial finite element software ABAQUS

Standard 6.13-2. Specifically, 2-nodes linear elements of type B21 (in the ABAQUS nomenclature) were employed to discretize the viscoelastic rod of constant, rectangular cross section. A number of 20 elements was found to be sufficient to adequately resolve for the rod dynamics. A linear viscoelastic model of the Kelvin-Voigt type was implemented for the constitutive response of the rod in a UMAT user subroutine, such that the bending moment $\mathcal{M}$ was proportional to the rod curvature and its time derivative through the elastic and viscous moduli, respectively. In the spirit of the linear model, the air drag (that is, the external source of damping) was accounted for with a distributed load, transversely applied to the rod and proportional to its velocity via the damping coefficient K. The follower forces P_{tang} and P_{orth} acting at the end of the rod (see the sketch of Fig. 4.2) were set proportional to the virtually applied weight W and to the respective friction coefficients μ_{tang} and μ_{orth}, the former of which is defined by Eq. (4.2), while the latter is defined by the same equation, but with the orthogonal velocity component v_{orth} replacing v_{tang} and with μ_0 replaced by $0.09\mu_0$.

From the computational standpoint, the friction law of Eq.(4.2) was implemented by exploiting the user subroutine UAMP together with the SENSOR functionality of ABAQUS. All the dynamic analyses were performed by exploiting the default settings of ABAQUS Standard 6.13-2 and with a time increment of 10^{-4} seconds. The values of the geometric and material parameters were employed as summarized in Table 4.1. Finally, to check for the accuracy of the finite element model, the critical weight W corresponding to the onset of flutter was numerically computed and compared with its theoretical value as provided by the linear model. Remarkable agreement was found for all the samples.

Three samples of different length were selected for the experimental and computational analysis of flutter and divergence in the nonlinear regime, namely sample 3, 5 and 8 of Table 4.1. These were tested at increasing values of $W = \{10, 15, 20, 25, 30, 35, 40\}$ N so as to explore the nonlinear response of the system. While conducting the experiments, high-speed movies were recorded at 240 fps. These were employed to track the position of the rod end in time, and consequently to estimate the frequency of the periodic

oscillations reached at the limit cycle. Data acquired from an accelerometer mounted at free end of the rod were also exploited to the same purpose.

Experimental results are reported in Fig. 4.11, together with the predictions obtained from the linear model and from the numerical simulations. The frequency is reported versus the applied load in the left part of the figure, while the trajectories of the rod's end are reported on the right for the three selected rods.

The evolution of the pulsation (and consequently of the frequency) shows an initial increase with the load level (in the flutter range), followed by a decrease (when divergence is approached). While the linearized solution (solid blue curve) displays a well-defined divergence threshold, both the experimental results (green spots) and the numerical simulations (red diamonds) evidence that vanishing of the pulsation is attained only in an asymptotic sense, so that, as already remarked, divergence cannot be discriminated just looking at the absence of oscillations. At high load, when the divergence region is entered, the numerical solution of the fully nonlinear problem highlights that there is an initial exponential growth of the solution (as the linearized analysis predicts), but after this the rod reaches a maximum of flexure, stops for a moment and then shows a sort of 'whipstroke-back', thus reaching an opposed inflected configuration (as reported on the right of Fig. 4.1). In other words, both the numerical solutions and the experiments show that the exponential growth predicted by the linearized solution degenerates into a sort of limit cycle oscillation.

Looking to the evolution of trajectories traced by the rod's end at different load levels, it can be noticed that the numerical simulation are in excellent agreement with the experiments reported. Furthermore, at increasing values of the applied weight W correspond a linear increase of the amplitude of the periodic motion. The region that contains all the possible positions of the free end of the cantilever rod can be called 'flutter cone'.

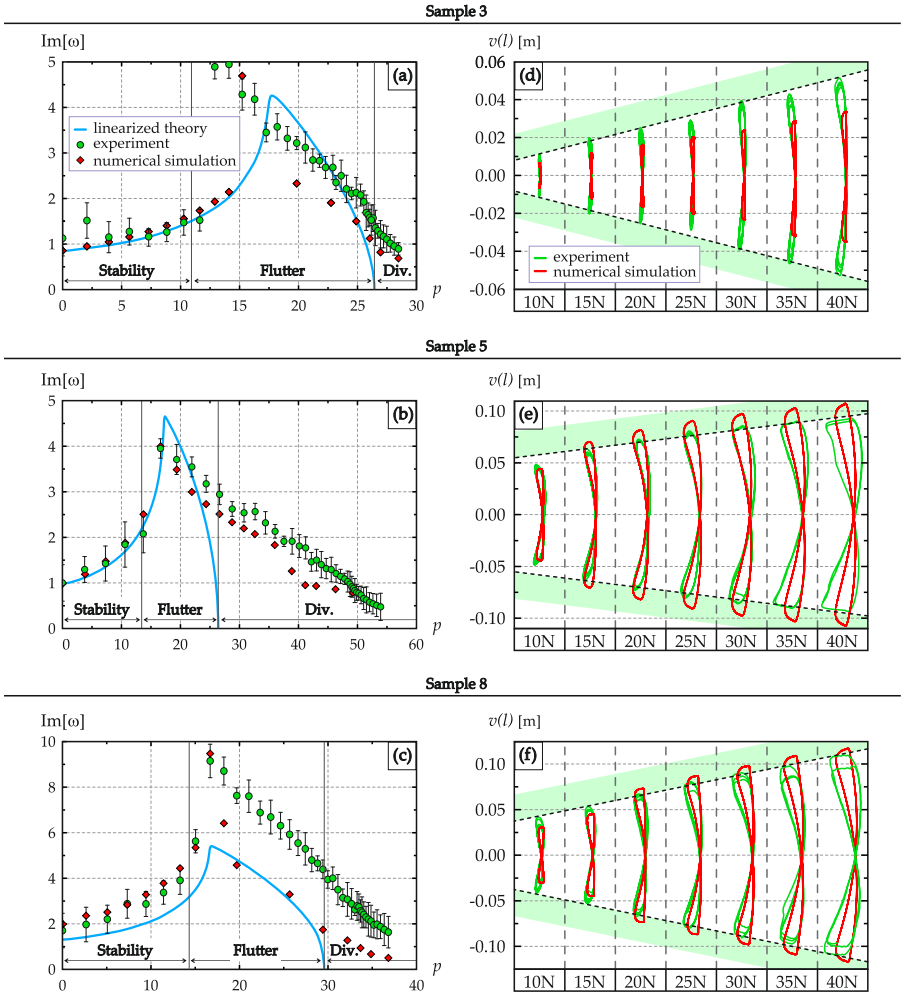

Figure 4.11: (a) The theoretical (from the linearized theory, blue solid curve), experimental (green spots) and computational (red diamonds) evolution of the pulsation Im[ω] is reported for three different samples at increasing loads. (b) Experimental (green) and numerical (red) trajectories of the Pflüger column end at increasing load. The velocity of the tape was set to 0.1 m/s.

5

Experimental investigation on the singular interface between the classical and reversible Hopf bifurcations

> It is a profound and necessary truth that the deep things in science are not found because they are useful; they are found because it was possible to find them.
>
> *J.R. Oppenheimer*

The 'flutter machine' is introduced for the investigation of a singular interface between the classical and reversible Hopf bifurcations that is theoretically predicted to be generic in nonconservative reversible systems with vanishing dissipation. In particular, such a singular interface exists for the Pflüger viscoelastic column moving in a resistive medium, which is proven by means of the perturbation theory of multiple eigenvalues with the Jordan block. The laboratory setup mentioned in Chapter 4 (consisting of a cantilevered viscoelastic rod loaded by a positional force with non-zero curl

produced by dry friction), demonstrates high sensitivity of the classical Hopf bifurcation onset to the ratio between the weak air drag and Kelvin-Voigt damping in the Pflüger column. Thus, the Whitney umbrella singularity is experimentally confirmed, responsible for discontinuities accompanying dissipation-induced instabilities in a broad range of physical contexts.

5.1 Introduction

In a dissipative system oscillatory flutter instability, an example of a classical Hopf bifurcation, shifts a complex-conjugate pair of eigenvalues to the right in the complex plane. This instability mechanism is modified for a non-dissipative system possessing a *reversible* symmetry, defined with reference to the differential equation

$$\frac{d\mathbf{x}}{dt} = \mathbf{g}(\mathbf{x}), \quad \mathbf{x} \in \mathbb{R}^n \tag{5.1}$$

which is said to be $\mathbf{R}$-reversible ($\mathbf{R}^{-1} = \mathbf{R}$) if it is invariant with respect to the transformation $(\mathbf{x}, t) \mapsto (\mathbf{R}\mathbf{x}, -t)$, implying that the right hand side must satisfy $\mathbf{R}\mathbf{g}(\mathbf{x}) = -\mathbf{g}(\mathbf{R}\mathbf{x})$.

If $\mathbf{x} = \mathbf{x}_0$ is a reversible equilibrium such that $\mathbf{R}\mathbf{x}_0 = \mathbf{x}_0$, and $\mathbf{A} = \nabla\mathbf{g}$ is the linearization matrix about $\mathbf{x}_0$, then $\mathbf{A} = -\mathbf{R}\mathbf{A}\mathbf{R}$, and the characteristic polynomial

$$\det(\mathbf{A} - \lambda\mathbf{I}) = \det(-\mathbf{R}\mathbf{A}\mathbf{R} - \mathbf{R}\lambda\mathbf{R}) = (-1)^n \det(\mathbf{A} + \lambda\mathbf{I}), \tag{5.2}$$

implies that $\pm\lambda, \pm\overline{\lambda}$ are eigenvalues of $\mathbf{A}$ [53–56]. Due to the spectrum's symmetry with respect to both the real and imaginary axes of the complex plane, the reversible-Hopf bifurcation requires the generation of a non-semi-simple double pair of imaginary eigenvalues and its subsequent separation into a complex quadruplet [53–56].

All equations of second order

$$\frac{d^2\mathbf{x}}{dt^2} = \mathbf{f}(\mathbf{x}), \tag{5.3}$$

are reversible [53, 54], including the case when the positional force $\mathbf{f}(\mathbf{x})$ has a non-trivial curl, $\nabla \times \mathbf{f}(\mathbf{x}) \neq 0$, which makes the reversible system *nonconservative*.

Such nonconservative *curl forces* [57] appear in modern opto-mechanical applications, including optical tweezers [58–60]. In mechanics, they are known as *circulatory forces* for producing non-zero work along a closed circuit. Circulatory forces are common in the models of friction-induced vibrations [61], rotordynamics [56], biomechanics [62] and fluid-structure interactions [63, 64], to name a few. A circulatory force acting on an elastic structure and remaining directed along the tangent line to the structure at the point of its application during deformation is known as *follower* [1, 11].

Since the dynamics of an elastic structure under a follower load is described by reversible equations [53], flutter instability may occur via the reversible-Hopf bifurcation mechanism [53, 56]. In these conditions, Ziegler [1] discovered that, when viscosity is present, the location of the curve for the onset of the classical Hopf bifurcation is displaced by an order-one distance in the parameter space, with respect to the curve for the onset of the reversible-Hopf bifurcation in the elastic structure. This occurs even if the viscous damping in the structure is infinitesimally small [1]. Other velocity-dependent forces, such as air drag (or even gyroscopic forces), can also destabilize an elastic structure under a follower load [15, 29, 36, 51, 53]. However, acting together, the velocity-dependent forces, e.g., the air drag and the material (Kelvin-Voigt) viscous damping, can *inhibit* the destabilizing effect of each other at a particular *ratio* of their magnitudes due to the singular interface between the classical Hopf and reversible-Hopf bifurcations [1, 27, 29, 51].

For instance, the system

$$\ddot{\mathbf{x}}(t) + (\delta\mathbf{D} + \Omega\mathbf{G})\dot{\mathbf{x}}(t) + (\mathbf{K} + \nu\mathbf{N})\mathbf{x}(t) = 0, \quad \mathbf{x} \in \mathbb{R}^2 \tag{5.4}$$

where δ, Ω, ν are scalar coefficients and matrices $\mathbf{D} > 0$, $\mathbf{K} > 0$ are real and symmetric, while matrices $\mathbf{G}$ and $\mathbf{N}$ are skew-symmetric as follows

$$\mathbf{G} = \mathbf{N} = \begin{pmatrix} 0 & -1 \\ 1 & 0 \end{pmatrix}, \tag{5.5}$$

is nonconservative and reversible for $\delta = \Omega = 0$.

The reversible-Hopf bifurcation in the system (5.4) with $\delta = \Omega = 0$ occurs at

$$\nu_f = \sqrt{\omega_f^4 - \det \mathbf{K}}, \quad \omega_f^2 = \frac{\mathrm{tr}\mathbf{K}}{2}, \tag{5.6}$$

where "tr" denotes the trace operator, which yields flutter instability when $\nu > \nu_f$. However, when $\delta > 0$, $\Omega > 0$ the classical-Hopf bifurcation occurs at a different value of ν [15]

$$\nu_H(\Omega, \delta) \approx \nu_f - \frac{2\nu_f}{(\mathrm{tr}\mathbf{D})^2} \left(\frac{\Omega}{\delta} - \frac{\mathrm{tr}(\mathbf{KD} - \omega_f^2 \mathbf{D})}{2\nu_f} \right)^2. \tag{5.7}$$

The expression for $\nu_H(\Omega, \delta)$ defines a surface in the (δ, Ω, ν)-space that has a Whitney's umbrella singular point[1] at $(0, 0, \nu_f)$ [66]. Near that singular point, the neutral stability surface is a ruled surface, with a self-intersection degenerating at the singularity, so that a unique value of the ratio Ω/δ is produced, for which the onsets of the classical and reversible Hopf bifurcations tend to coincide[1] [27, 29].

For a dissipative nearly-reversible system, the singular dependence of the classical Hopf bifurcation onset on the parameters of velocity-dependent forces has a general character [27], which follows from the codimension 3 (for dissipative systems) and 1 (for reversible vector fields) of non-semi-simple double imaginary eigenvalues [15, 27, 29, 65, 67].

Since the singularity is related to a double imaginary eigenvalue arising from a Jordan block [65], it can be found in other dissipative systems that are close to undamped systems with the 'reversible' symmetry of spectrum [29].

Indeed, the system (5.4) with $\delta = 0$, $\Omega = 0$, and $\nu = 0$ is a conservative Hamiltonian system, which is statically unstable for $\mathbf{K} < 0$. Adding gyroscopic forces with $\Omega > 0$, keeps this system Hamiltonian and yields its

[1]The normal form of a surface in the $Oxyz$-space that has the Whitney umbrella singular point at the origin is given by the equation $zy^2 = x^2$ [15, 27, 29, 65, 66]. The function $z(x, y) = x^2/y^2 > 0$ at all x, y except for the specific line $x = 0$, where $z(0, y) = 0$.

stabilization if $\Omega > \Omega_f = \sqrt{-\kappa_1} + \sqrt{-\kappa_2}$, where $\kappa_{1,2} < 0$ are eigenvalues of $\mathbf{K}$. Owing to the 'reversible' symmetry of its spectrum [53, 68, 69], the Hamiltonian system displays flutter instability via the collision of imaginary eigenvalues at $\Omega = \Omega_f$ and their subsequent splitting into a complex quadruplet as soon as Ω decreases below Ω_f. This is the so-called linear Hamilton-Hopf bifurcation [15, 66, 70].

If $\delta > 0$, $\nu > 0$ the gyroscopic stability is destroyed at the threshold of the classical-Hopf bifurcation [15, 70]

$$\Omega_H \approx \Omega_f + \frac{2\Omega_f}{(\omega_f \mathrm{tr}\mathbf{D})^2}\left(\frac{\nu}{\delta} - \frac{\mathrm{tr}(\mathbf{KD} + (\Omega_f^2 - \omega_f^2)\mathbf{D})}{2\Omega_f}\right)^2, \qquad (5.8)$$

where $\omega_f^2 = \sqrt{\kappa_1\kappa_2}$ and $\mathbf{D} > 0$. The dependency of the new gyroscopic stabilization threshold just on the ratio ν/δ implies that the limit of Ω_H as both ν and $\delta \to 0$ is higher than Ω_f for all ratios except a unique one. Similarly to the case of nonconservative reversible systems, this happens because the classical Hopf and the Hamilton-Hopf bifurcations meet in the Whitney umbrella singularity that exists on the stability boundary of a nearly-Hamiltonian dissipative system and corresponds to the onset of the Hamilton-Hopf bifurcation [15, 28, 29, 66, 67, 69, 70].

The singular weak-dissipation limit for the flutter onset in nearly - Hamiltonian systems in the presence of two different damping mechanisms has been discovered first in the problem of secular instability of equilibria of rotating and self-gravitating masses of fluid, when dissipation due to both fluid viscosity [46, 71, 72] and emission of gravitational waves [73, 74] is taken into account [75, 76]. Later on this phenomenon manifested itself as the 'Holopäinen instability mechanism' for a baroclinic flow [77, 78] and as an enhancement of modulation instability with dissipation [79]. Analysis of this effect based on the method of normal forms and perturbation of multiple eigenvalues has been developed, among others by [15, 27, 29, 32, 44, 53, 56, 65, 67–70, 80–84].

Although the destabilizing effect of damping for equilibria of Hamiltonian and reversible systems has been discussed for decades, no experimental evidence is known for the singular limit of the classical Hopf bifurcation in

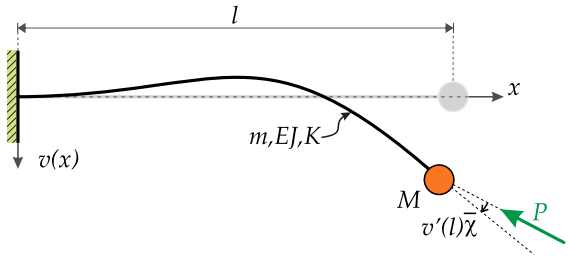

Figure 5.1: The Pflüger column clamped at $x = 0$ with a point mass M at $x = l$. The column is loaded at $x = l$ with a constant compressing circulatory force P inclined to the tangent to the elastic line of the column, so that $v'(l)\bar{\chi} = const.$ (equal to 0.092 in all the experiments).

a nearly-Hamiltonian, or a nearly-reversible system, when the dissipation tends to zero. The main difficulty for such experiments is the accurate identification and control of at least two different damping mechanisms. For reversible elastic structures an additional challenge lies in the realization of circulatory follower loads, acting for a sufficiently long time. Previous attempts are reported to create a follower load through the thrust produced either by water flowing through a nozzle (Wood [19]), or by a solid rocket motor mounted at the end of an elastic rod in a cantilever configuration (Sugiyama [21, 85–87]). In the former realization hydrodynamical effects enter into play and in the latter the duration of the experiments is limited to a few seconds. In contrast, the frictional follower force acting on a wheel mounted at the free end of the double-link Ziegler double pendulum allowed Bigoni [22] to significantly relax the limitation on time.

The case study of this Chapter is related to the Pflüger column [2, 9, 42, 43] of Chapter 4, a viscoelastic cantilevered rod carrying a point mass at the free end and loaded with a follower force (as already described in Fig. 4.6) obtained via friction (similarly to [22]). Two dissipation mechanisms—the air resistance and the internal Kelvin-Voigt damping—are identified and controlled by changing the geometrical characteristics of the sample rods. The measured critical flutter loads demonstrate a high sensitivity to the

ratio between the two damping coefficients, being almost insensitive to each of the damping coefficients that both are very close to zero, in agreement with both numerical modeling of [51] and perturbation theory developed for the Pflüger column in the present work.

5.2 Galerkin discretization of the Pflüger column

Consider a rod of length l, mass density per unit length m and end mass M, its deflection v, function of the x coordinate, obeys the Bernoulli law that the rotation of the cross-section ϕ is given by $\phi(x) = -v'(x)$, where a prime denotes derivative with respect to x. A moment-curvature viscoelastic constitutive relation of the Kelvin-Voigt type is assumed in the form

$$\mathcal{M}(x,t) = -EJv''(x,t) - E^*J\dot{v}''(x,t), \tag{5.9}$$

where a superimposed dot denotes the time derivative, E and E^* are respectively the elastic and the viscous moduli of the rod, which has a cross section with moment of inertia J. The rod is clamped at one end and is loaded through the force P that is inclined with respect to the tangent to the rod at its free end such that $v'(l)\bar{\chi} = const.$ (Fig. 5.1).

Assuming that a distributed external damping K caused by the air drag is acting on the rod, and introducing the dimensionless quantities

$$\xi = \tfrac{x}{l},\ \tau = \tfrac{t}{l^2}\sqrt{\tfrac{EJ}{m}},\ p = \tfrac{Pl^2}{EJ},\ \alpha = \tan^{-1}\left(\tfrac{M}{ml}\right),$$

$$\eta = \tfrac{E^*l^2}{\sqrt{mEJ}}\tfrac{J}{l^4},\ \gamma = \tfrac{Kl^2}{\sqrt{mEJ}},\ \beta = \tfrac{\gamma}{\eta},\ \chi = 1 - \bar{\chi}, \tag{5.10}$$

the linearized partial differential equation of motion governing the dynamics of the rod can be written as

$$v''''(\xi,\tau) + \eta\dot{v}''''(\xi,\tau) + pv''(\xi,\tau) + \gamma\dot{v}(\xi,\tau) + \ddot{v}(\xi,\tau) = 0, \tag{5.11}$$

where now a prime and a dot denote partial differentiation with respect to ξ and τ, respectively. Separating time in Eq.(5.11) with $v(\xi,\tau) = \tilde{v}(\xi)\exp(\omega\tau)$ yields a non-self-adjoint boundary eigenvalue problem [51]

$$\begin{gathered}(1+\eta\omega)\tilde{v}'''' + p\tilde{v}'' + (\gamma\omega+\omega^2)\tilde{v} = 0,\\ (1+\eta\omega)\tilde{v}'''(1) - (\chi-1)\tilde{v}'(1)p - \omega^2\tan(\alpha)\tilde{v}(1) = 0,\\ \tilde{v}(0) = \tilde{v}'(0) = 0, \quad \tilde{v}''(1) = 0. \end{gathered} \tag{5.12}$$

Assuming that $\tilde{v}(\xi)$ has the form

$$\begin{aligned}\tilde{v}(\xi) \quad &= A_1\sinh(\lambda_1\xi) + A_2\cosh(\lambda_1\xi) + \\ &+ A_3\sin(\lambda_2\xi) + A_4\cos(\lambda_2\xi),\end{aligned} \tag{5.13}$$

with A_i $(i = 1,..,4)$ arbitrary constants and

$$\lambda_{1,2}^2 = \frac{\sqrt{p^2 - 4(1+\eta\omega)(\gamma\omega+\omega^2)} \mp p}{2(1+\eta\omega)} \tag{5.14}$$

and substituting Eq.(5.13) into Eqs.(5.12) yields an algebraic system of equations which admits non-trivial solutions if [51]

$$\begin{aligned}0 = {} & \lambda_1\lambda_2(1+\eta\omega)(\lambda_1^4+\lambda_2^4) + \lambda_1\lambda_2 p(\chi-1)(\lambda_2^2-\lambda_1^2) + \\ & + \lambda_1\lambda_2[2(1+\eta\omega)\lambda_1^2\lambda_2^2 - p(\chi-1)(\lambda_2^2-\lambda_1^2)]\cosh\lambda_1\cos\lambda_2 + \\ & - \omega^2\tan\alpha(\lambda_1^2+\lambda_2^2)[\lambda_2\sinh\lambda_1\cos\lambda_2 - \lambda_1\cosh\lambda_1\sin\lambda_2] + \\ & \lambda_1^2\lambda_2^2[2p(\chi-1) + (1+\eta\omega)(\lambda_2^2-\lambda_1^2)]\sinh\lambda_1\sin\lambda_2.\end{aligned} \tag{5.15}$$

Results from experiments are compared with the eigenvalues, eigenfunctions and critical parameters of the boundary eigenvalue problem (5.12) which are directly found by numerical solution of the transcendental characteristic equation (5.15).

For theoretical purposes, the N-dimensional Galerkin discretization of the continuous problem (5.12) is also considered:

$$(\omega^2[\mathbf{I}+4\mathbf{M}_1\tan\alpha]+\omega[\gamma\mathbf{I}+\eta\mathbf{D}_i]+[\mathbf{K}_1-p\mathbf{K}_2+\chi p\mathbf{N}])\mathbf{a}=0, \tag{5.16}$$

where $\mathbf{a}$ is an N-vector and $\mathbf{I}$ is the $N\times N$ identity matrix. The entries of the $N\times N$ mass matrix $\mathbf{M}_1$ are $M_{1,ij}=(-1)^{i+j}$, the matrix of internal damping $\mathbf{D}_i$ is $\mathbf{D}_i=\mathrm{diag}(\omega_1^2,\omega_2^2,\ldots,\omega_N^2)$, and the stiffness matrix $\mathbf{K}_1$ is $\mathbf{K}_1=\mathrm{diag}(\omega_1^2,\omega_2^2,\ldots,\omega_N^2)$. The values of the frequencies $\omega_1,\ldots,\omega_N$ as well as the entries of the symmetric stiffness matrix $\mathbf{K}_2$ and the non-symmetric matrix of circulatory forces $\mathbf{N}$ are given in the Appendix C.1.

5.3 Theory of dissipation-induced flutter instability

For a Galerkin-discretized model of the Pflüger column (imposing an approximation of $N=2$) described in Eq.(5.16) a perturbation theory is developed of the singular weak-dissipation limit for the onset of flutter.

The eigenvalue problem (5.16) has the form

$$(\mathbf{M}(\alpha)\omega^2+\mathbf{D}(\gamma,\eta)\omega+\mathbf{A}(p,\chi))\mathbf{a}=0, \tag{5.17}$$

where $\mathbf{M}=\mathbf{M}^T$, $\mathbf{D}=\mathbf{D}^T$, $\mathbf{D}(0,0)=0$, and $\mathbf{A}\neq\mathbf{A}^T$, with the superscript T denoting transposition.

Recall that the adjugate $\mathbf{X}^*$ of a $N\times N$ matrix $\mathbf{X}$ is defined as $\mathbf{X}^*=\mathbf{X}^{-1}\det\mathbf{X}$ and, in particular,

$$\frac{\partial\det\mathbf{X}}{\partial p}=\mathrm{tr}\left(\mathbf{X}^*\frac{\partial\mathbf{X}}{\partial p}\right). \tag{5.18}$$

Since $\mathrm{tr}(\mathbf{X}^*\mathbf{Y})=\mathrm{tr}(\mathbf{Y}^*\mathbf{X})$ for $N=2$, the characteristic polynomial of Eq.(5.17) in the case of $N=2$ can be written by means of the Leverrier algorithm in a compact form:

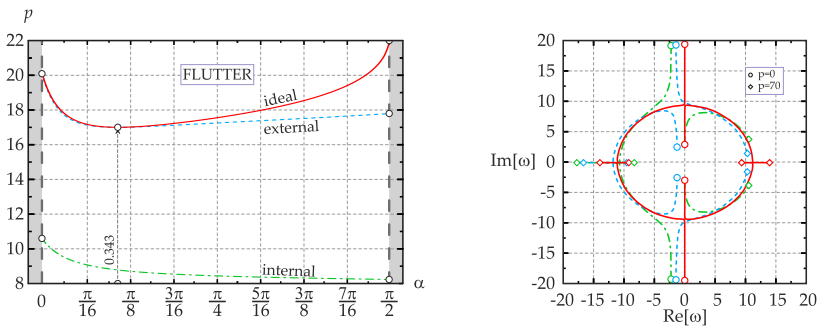

Figure 5.2: (Left) Stability boundary for (green dash-dot) internally and (blue dashed) externally damped discretized model of the Pflüger column with $N = 2$ modes and pure follower force ($\chi = 1$), when one of the damping coefficients is zero and another one tends to zero. The red solid curve shows the stability boundary of the non-damped discretized model of the Pflüger column according to Eq.(5.21). (Right) The eigenvalue movement when p increases from 0 (circle) to 70 (diamond) for $N = 2$, $\chi = 1$, $\alpha = 0.1$, and (red curves) $\gamma = 0$, $\eta = 0$, (blue dashed curves) $\gamma = 4.5$, $\eta = 0$, and (green dash-dotted curves) $\gamma = 0$, $\eta = 0.015$.

$$q(\omega, \alpha, \chi, p, \gamma, \eta) = \det \mathbf{M}\omega^4 + \mathrm{tr}(\mathbf{D}^*\mathbf{M})\omega^3 + \\ +(\mathrm{tr}(\mathbf{A}^*\mathbf{M}) + \det \mathbf{D})\omega^2 + \mathrm{tr}(\mathbf{A}^*\mathbf{D})\omega + \det \mathbf{A}. \tag{5.19}$$

Assuming that for $\eta = 0$, $\gamma = 0$, $\alpha = \alpha_0$, $\chi = \chi_0$, and $p = p_0$ the undamped system with $N = 2$ degrees of freedom be on the flutter boundary, on this boundary its eigenvalues are imaginary and form a double complex-conjugate pair $\omega = \pm i\sigma_0$ of a Jordan block. In these conditions, the real critical frequency σ_0 at the onset of flutter follows from the characteristic polynomial in the closed form

$$\sigma_0^2 = \frac{\mathrm{tr}(\mathbf{A}_0^*\mathbf{M}_0)}{2\det \mathbf{M}_0} = \sqrt{\frac{\det \mathbf{A}_0}{\det \mathbf{M}_0}}, \\ \mathbf{M}_0 = \mathbf{M}(\alpha_0), \quad \mathbf{A}_0 = \mathbf{A}(p_0, \chi_0) \tag{5.20}$$

and the flutter boundary is described by the equation

$$(\mathrm{tr}(\mathbf{A}_0^*\mathbf{M}_0))^2 = 4\det\mathbf{A}_0\det\mathbf{M}_0. \tag{5.21}$$

Since $\mathbf{M}_0 = \mathbf{I} + 4\mathbf{M}_1\tan\alpha_0$ and $\mathbf{A}_0 = \mathbf{K}_1 - p_0\mathbf{K}_2 + \chi_0 p_0\mathbf{N}$ is a linear function of p_0, Eq.(5.21) is quadratic with respect to p_0, which can thus be easily solved. The red solid curve in Fig. 5.2(left) shows the flutter boundary (5.21) of the undamped discretized model (5.16) of the Pflüger column with $N = 2$ modes for $\chi_0 = 1$ in the (α_0, p_0)-plane. The red solid curves in Fig. 5.2(right) demonstrate the movement of the eigenvalues of the undamped system at given $\chi = \chi_0 = 1$ and $\alpha = \alpha_0 = 0.1$ when the load parameter $0 \le p \le 70$. The equilibrium is stable for $0 \le p < p_0$ where the critical flutter load is $p_0 \approx 17.83368$, corresponding to a double pair of imaginary eigenvalues with the imaginary part $\sigma_0 \approx 9.366049$ (see Eq.(5.20)). The value $p = p_0$ corresponds to the linear reversible-Hopf bifurcation, yielding the splitting of the double eigenvalues into a complex quadruplet causing flutter instability.

5.3.1 Reversible-Hopf bifurcation in the undamped model

A perturbation formula is now derived for the splitting of a double eigenvalue $\omega = i\sigma_0$, when $\gamma = \gamma_0$ and $\alpha = \alpha_0$ are fixed and p is left to vary. Introducing a small parameter $0 \le \varepsilon \ll 1$ and assuming in the polynomial $q_0(\omega, p) = q(\omega, \alpha_0, \chi_0, p, \gamma = 0, \eta = 0)$ that $p(\varepsilon) = p_0 + \varepsilon\frac{dp}{d\varepsilon} + \dots$ (where the derivative is taken at $\varepsilon = 0$) yields

$$\begin{gathered} q_0(\omega, p(\varepsilon)) = \textstyle\sum_{r=0}^{2N} \frac{(\omega(\varepsilon)-i\sigma_0)^r}{r!}\left(\frac{\partial^r q_0}{\partial\omega^r} + \varepsilon\frac{\partial^r q_1}{\partial\omega^r} + o(\varepsilon)\right), \\ \frac{\partial^r q_1}{\partial\omega^r} = \frac{\partial^{r+1} q_0}{\partial\omega^r\partial p}\frac{dp}{d\varepsilon}, \end{gathered} \tag{5.22}$$

where the partial derivatives are evaluated at $p = p_0$ and $\omega = i\sigma_0$.

Assuming for the perturbed double non-semisimple eigenvalue the Newton-Puiseux series

$$\omega(\varepsilon) = i\sigma_0 + \varepsilon^{1/2}\sigma_1 + \varepsilon\sigma_2 + \dots, \tag{5.23}$$

substituting Eqs.(5.22) and (5.23) into the equation $q_0(\omega, p)$ and collecting the terms of the same powers of ε, leads to

$$q_0(i\sigma_0, p_0) = 0, \quad \sigma_1 \frac{\partial q_0}{\partial \omega}\bigg|_{\omega=i\sigma_0, p=p_0} = 0, \tag{5.24}$$

and

$$\left(q_1 + \frac{1}{2}\sigma_1^2 \frac{\partial^2 q_0}{\partial \omega^2} + \sigma_2 \frac{\partial q_0}{\partial \omega}\right)\bigg|_{\omega=i\sigma_0, p=p_0} = 0. \tag{5.25}$$

Conditions (5.24) are satisfied for the double eigenvalue $\omega = i\sigma_0$, so that an account of this into (5.25) yields

$$\sigma_1^2 = -q_1 \left(\frac{1}{2}\frac{\partial^2 q_0}{\partial \omega^2}\right)^{-1} = -\left(\frac{1}{2}\frac{\partial^2 q_0}{\partial \omega^2}\right)^{-1} \frac{\partial q_0}{\partial p}\frac{dp}{d\varepsilon}.$$

Hence, the splitting of the double non-semisimple eigenvalue due to the variation of p is governed by the formula

$$\omega(p) = i\sigma_0 \pm i\sqrt{\left(\frac{1}{2}\frac{\partial^2 q_0}{\partial \omega^2}\right)^{-1} \frac{\partial q_0}{\partial p}(p - p_0)} + o(|p - p_0|^{1/2}).$$

With the help of Eqs.(5.18) and (5.20), and the relations

$$\begin{gathered} q_0(\omega, p) = \omega^4 \det \mathbf{M} + \omega^2 \mathrm{tr}(\mathbf{M}^* \mathbf{A}) + \det \mathbf{A}, \\ \frac{\partial q_0}{\partial p}\bigg|_{\omega=i\sigma_0, p=p_0} = -\mathrm{tr}\left((\mathbf{A}_0^* - \sigma_0^2 \mathbf{M}_0^*)(\mathbf{K}_2 - \chi_0 \mathbf{N})\right), \\ \frac{1}{2}\frac{\partial^2 q_0}{\partial \omega^2}\bigg|_{\omega=i\sigma_0, p=p_0} = -2\mathrm{tr}(\mathbf{A}_0^* \mathbf{M}_0), \end{gathered} \tag{5.26}$$

the following result is finally obtained

$$\begin{gathered} \omega(p) = i\sigma_0 \\ \pm i\sqrt{\frac{\mathrm{tr}\left[(\mathbf{A}_0^* - \sigma_0^2 \mathbf{M}_0^*)(\mathbf{K}_2 - \chi_0 \mathbf{N})\right]}{2\mathrm{tr}(\mathbf{A}_0^* \mathbf{M}_0)}(p - p_0)} + o(|p - p_0|^{1/2}). \end{gathered} \tag{5.27}$$

For instance, for $\alpha_0 = 0.1$, $\chi_0 = 1$, $p_0 \approx 17.83368$, and $\sigma_0 \approx 9.366049$, Eq.(5.27) becomes

$$\omega(p) \approx i\sigma_0 \pm i\sqrt{-3.962532(p - p_0)} \tag{5.28}$$

confirming the splitting of the double $i\sigma_0$ into two complex eigenvalues with opposite real parts (flutter) at $p > p_0$.

5.3.2 Dissipative perturbation of simple imaginary eigenvalues

At $p < p_0$ the eigenvalues of the undamped system $\omega = \omega(p)$ remain simple and imaginary. To investigate how they are affected by dissipation, it is assumed that $\eta(\varepsilon) = \frac{d\eta}{d\varepsilon}\varepsilon + o(\varepsilon)$, and $\gamma(\varepsilon) = \frac{d\gamma}{d\varepsilon}\varepsilon + o(\varepsilon)$ in the polynomial (5.19), where $\alpha = \alpha_0$, $\gamma = \gamma_0$ and $0 \leq p < p_0$ are also fixed. Then, $\omega = \omega(p) + \frac{d\omega}{d\varepsilon}\varepsilon + o(\varepsilon)$, with

$$\frac{d\omega}{d\varepsilon} = -\left(\frac{\partial q}{\partial \omega}\right)^{-1}\left(\frac{\partial q}{\partial \eta}\frac{d\eta}{d\varepsilon} + \frac{\partial q}{\partial \gamma}\frac{d\gamma}{d\varepsilon}\right).$$

The following approximation is therefore obtained

$$\omega = \omega(p) - \left(\frac{\partial q}{\partial \omega}\right)^{-1}\left(\frac{\partial q}{\partial \eta}\eta + \frac{\partial q}{\partial \gamma}\gamma\right) + o(\gamma, \eta),$$

where the partial derivatives are evaluated at $p < p_0$ and $\omega = \omega(p)$. An account of the following derivatives

$$\begin{aligned} \tfrac{\partial q}{\partial \omega} &= 2\sigma_0^{-2}\omega \mathrm{tr}(\mathbf{M}_0^*(\omega^2\mathbf{A}_0 + \sigma_0^2\mathbf{A})), \\ \tfrac{\partial q}{\partial \eta} &= \omega \mathrm{tr}\left(\mathbf{D}_i^*(\mathbf{A} + \omega^2\mathbf{M}_0)\right), \\ \tfrac{\partial q}{\partial \gamma} &= \omega \mathrm{tr}\left(\mathbf{A} + \omega^2\mathbf{M}_0\right), \end{aligned} \tag{5.29}$$

leads to

$$\begin{aligned}\omega &= \omega(p) + \\ &- \frac{\eta \mathrm{tr}\left(\mathbf{D}_i^*(\mathbf{A}+\omega^2\mathbf{M}_0)\right) + \gamma \mathrm{tr}\left(\mathbf{A}+\omega^2\mathbf{M}_0\right)}{2\mathrm{tr}(\mathbf{M}_0^*(\omega^2\mathbf{A}_0+\sigma_0^2\mathbf{A}))}\sigma_0^2 + \\ &+ o(\gamma,\eta). \end{aligned} \tag{5.30}$$

5.3.3 Linear approximation to the stability boundary and the exact zero-dissipation limit of the critical flutter load

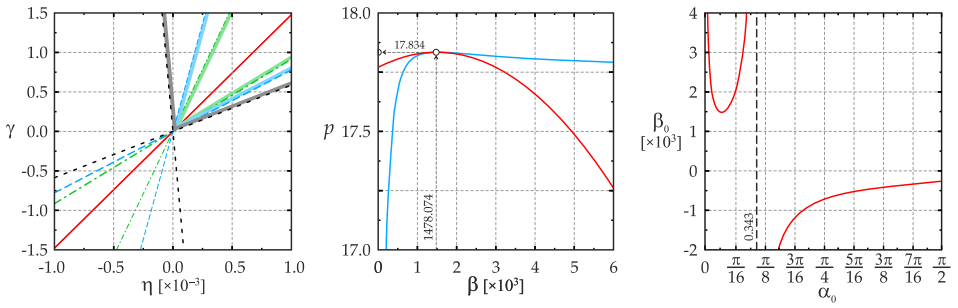

Figure 5.3: (Left) For $N = 2$, $\chi_0 = 1$, and $\alpha_0 = 0.1$ the linear approximation (5.31) to the classical-Hopf bifurcation onset in the (η, γ)-plane for (black) $p = p_0 - 0.1$, (blue) $p = p_0 - 0.04$, (green) $p = p_0 - 0.02$, and (red) $p = p_0$. The stability region for every p is inside the narrow angle-shaped regions in the first quadrant; flutter instability in the complement. (Centre) The critical flutter load in the limit of vanishing dissipation as a function of the damping ratio $\beta = \gamma/\eta$ according to the (blue curve) exact expression (5.31) and (red curve) its quadratic approximation (5.32). The maximum of the limit coincides with the critical flutter load $p_0 \approx 17.83368$ of the undamped system at $\beta = \beta_0 \approx 1478.074$ that is determined from Eq.(5.33). (Right) The stabilizing ratio β_0 as a function of α_0 according to Eq.(5.33) with vertical asymptotes at $\alpha_0 = 0$ (Beck column) and $\alpha_0 \approx 0.342716$.

The correction, linear in η and γ, to the simple imaginary eigenvalue in Eq.(5.30) due to damping is real and therefore it determines whether the

dissipative perturbation is stabilizing or destabilizing. Equating this linear term to zero and taking into account that $\mathbf{A} = \mathbf{K}_1 - p(\mathbf{K}_2 - \chi_0\mathbf{N})$ and $\mathbf{D}_i = \mathbf{K}_1 = \mathrm{diag}(\omega_1^2, \omega_2^2)$ yields the following approximation to the flutter boundary, which represents the onset of the classical Hopf bifurcation

$$\begin{aligned}\eta\left[2\omega_1^2\omega_2^2 + \mathrm{tr}(\mathbf{D}_i^*(\mathbf{M}_0\omega^2(p) - p(\mathbf{K}_2 - \chi_0\mathbf{N})))\right] = \\ -\gamma\left[\omega_1^2 + \omega_2^2 + \mathrm{tr}(\mathbf{M}_0\omega^2(p) - p(\mathbf{K}_2 - \chi_0\mathbf{N})\right],\end{aligned} \tag{5.31}$$

where $\mathbf{M}_0 = \mathbf{I} + 4\mathbf{M}_1 \tan\alpha_0$ and $\omega(p)$ is a root of the polynomial $q_0(\omega, p)$ in Eq.(5.26)$_1$ at $p < p_0$. In the (η, γ)-plane the Eq.(5.31) defines a straight line, Fig. 5.3(left). In fact, at every $p < p_0$ there exist two lines (5.31) corresponding to two different eigenvalues $\omega(p)$ that participate in the reversible-Hopf bifurcation at $p = p_0$. However, as p tends to p_0, the angle between the two lines decreases and completely vanishes in the limit $p \to p_0$, Fig. 5.3(left). This suggests that the approximation (5.31) defines a ruled surface in the (η, γ, p)-space. As a consequence, every fixed damping ratio $\beta = \gamma/\eta$ corresponds to a ruler at some $p < p_0$. Therefore, the condition for which the damping tends to zero at fixed damping ratio will occur along this ruler for the corresponding constant value of $p < p_0$ and will result in the limiting value of the critical flutter load that is lower than the critical load at the onset of the reversible-Hopf bifurcation, p_0, see Fig. 5.3(centre). Note that Eq.(5.31) gives the exact dependency of the limit of the critical flutter load at vanishing dissipation as a function of the damping ratio, β, if the exact solution $\omega(p)$ of the polynomial $q_0(\omega, p)$ is used, see [15, 29, 32, 70, 82].

5.3.4 Quadratic approximation in β to the exact zero-dissipation limit of the critical flutter load

In the vicinity of $p = p_0$ the two roots participating in the reversible-Hopf bifurcation are approximated by Eq.(5.27). Using this expression in Eq.(5.31), the limit of zero dissipation can be found for the critical flutter load as a function of the damping ratio, $p(\beta)$, in the form of a series

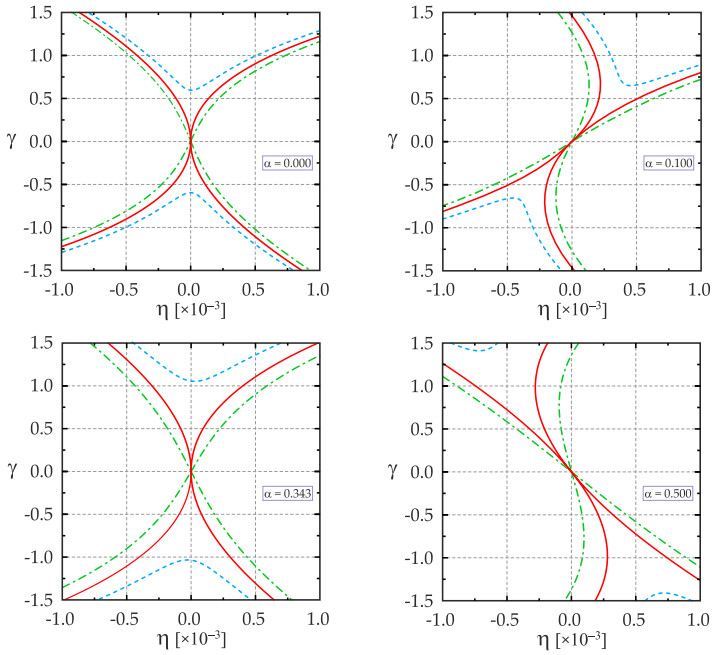

Figure 5.4: For $N = 2$, $\chi_0 = 1$, stability boundary of the discretized model for the Pflüger column in the plane of internal, η, and external, γ, damping for (upper left) $\alpha_0 = 0$ with $\beta_0 \to +\infty$, (upper right) $\alpha_0 = 0.1$ with $\beta_0 \approx 1478.074$, (lower left) $\alpha_0 \approx 0.3427$ with $\beta_0 \to +\infty$, (lower right) $\alpha_0 = 0.5$ with $\beta_0 \approx -1856.099$. The red solid lines correspond to the undamped critical load $p = p_0(\alpha_0)$, which depends on α_0, the blue dashed lines to $p = p_0(\alpha_0) + 0.02$, and the green dash-dotted lines to $p = p_0(\alpha_0) - 0.02$.

$$p(\beta) = p_0 - \frac{2\mathrm{tr}(\mathbf{A}_0^* \mathbf{M}_0)}{\mathrm{tr}\left[(\mathbf{A}_0^* - \sigma_0^2 \mathbf{M}_0^*)(\mathbf{K}_2 - \chi_0 \mathbf{N})\right]} \cdot$$
$$\cdot \left[\frac{\mathrm{tr}\left(\mathbf{A}_0 - \sigma_0^2 \mathbf{M}_0\right)}{2\sigma_0 \mathrm{tr}(\mathbf{M}_0^*(\beta_0 \mathbf{I} + \mathbf{D}_i))}\right]^2 (\beta - \beta_0)^2 + o((\beta - \beta_0)^2), \tag{5.32}$$

where

$$\beta_0 = -\frac{\mathrm{tr}\left(\mathbf{D}_i^*(\mathbf{A}_0 - \sigma_0^2\mathbf{M}_0)\right)}{\mathrm{tr}\left(\mathbf{A}_0 - \sigma_0^2\mathbf{M}_0\right)}. \tag{5.33}$$

From the quadratic approximation (5.32) it is evident that $p(\beta) \leq p_0$ for all β except for the specific case of $\beta = \beta_0$, at which it exactly coincides with the critical flutter load of the undamped system: $p(\beta_0) = p_0$. For instance, for $\alpha_0 = 0.1$ and $\chi_0 = 1$, the approximation (5.32) is

$$p(\beta) \approx 17.83368 - 2.807584 \cdot 10^{-8}(\beta - 1478.074)^2, \tag{5.34}$$

as shown in Fig. 5.3(centre) with a red solid curve.

5.3.5 The Whitney umbrella singularity

Truncating the series (5.32) and substituting $\beta = \gamma/\eta$ into the result, yields an expression for the ruled surface in the (η, γ, p)-space

$$p(\gamma,\eta) = p_0 - \frac{2\mathrm{tr}(\mathbf{A}_0^*\mathbf{M}_0)}{\mathrm{tr}\left[(\mathbf{A}_0^* - \sigma_0^2\mathbf{M}_0^*)(\mathbf{K}_2 - \chi_0\mathbf{N})\right]} \cdot \\ \cdot \left[\frac{\mathrm{tr}\left(\mathbf{A}_0 - \sigma_0^2\mathbf{M}_0\right)}{2\sigma_0\mathrm{tr}(\mathbf{M}_0^*(\beta_0\mathbf{I} + \mathbf{D}_i))}\right]^2 \frac{(\gamma - \beta_0\eta)^2}{\eta^2}. \tag{5.35}$$

This expression is in the form $Z = X^2/Y^2$, which is the well-known normal form for the Whitney umbrella surface [12-15]. The surface described by (5.35) has a singular point at $p = p_0$, corresponding to the onset of the reversible-Hopf bifurcation, and a self-intersection at $p < p_0$.

In Fig. 5.4 the cross-sections are plotted in the (η, γ)-plane for different values of p of the exact stability boundary calculated with the use of the Routh-Hurwitz criterion applied directly to the polynomial (5.19). Physically relevant is the first quadrant of the (η, γ)-plane.

For every $\alpha_0 \in [0, \pi/2]$ the cross-sections look qualitatively similar. For $p > p_0$ the stability domain is bounded by a smooth curve departing from the origin, Fig. 5.4. For $p = p_0(\alpha_0)$ the stability boundary has a cuspidal

point at the origin with the single tangent line to the boundary specified by the ratio β_0 given by the Eq.(5.33); the stability region is inside the cusp. For $p < p_0(\alpha_0)$ the stability boundary has a point of intersection at the origin in the (η, γ)-plane; the stability region is inside the narrow angle-shaped domain, which becomes wider as p decreases and for $p = 0$ spreads over the first quadrant of the plane for every possible mass distribution.

A comparison between Fig. 5.3(left) and the upper right panel of Fig. 5.4 shows that Eq.(5.31) gives a correct linear approximation to the stability domain provided by the Routh-Hurwith criterion in the (η, γ)-plane and, therefore, to the singular interface between the classical-Hopf and reversible-Hopf bifurcations in the (η, γ, p)-space.

5.3.6 Stabilizing damping ratio β_0 for different mass distributions α_0

Fig. 5.4 demonstrates that the contour plot patterns of the stability boundary in the (η, γ)-plane remain qualitatively the same for different values of α_0, but differ in the orientation of the cusp, which is determined by the stabilizing damping ratio β_0. Evaluating the series in (5.33) at the points of the stability boundary of the undamped system, provides the plot of the function $\beta_0(\alpha_0)$ reported in Fig. 5.3(right). One can see that two intervals of α_0 exist with opposite signs of β_0. The intervals are bounded by the values $\alpha_0 = 0$ and $\alpha_0 \approx 0.342716$, at which the graph $\beta_0(\alpha_0)$ displays a vertical asymptote, Fig. 5.3(right). Positive values of β_0 correspond to sufficiently small $\alpha_0 \leq 0.342716$, cf. the upper right panel of Fig. 5.4; negative values of β_0 are characteristic for $0.342716 \leq \alpha_0 \leq \pi/2$.

The above critical values of α_0 are determined by the zeros of the denominator of Eq.(5.33). Indeed, taking into account that

$$\begin{aligned} \mathrm{tr}\mathbf{M}_0 = 2 + 8\tan\alpha_0, \quad \det\mathbf{M}_0 = 1 + 8\tan\alpha_0, \\ \mathrm{tr}(\mathbf{A}_0^*\mathbf{M}_0) = \mathrm{tr}\mathbf{A}_0 + 4\mathrm{tr}(\mathbf{M}_1^*\mathbf{A}_0)\tan\alpha_0, \end{aligned} \tag{5.36}$$

the denominator can be obtained in the form

$$\mathrm{tr}(\mathbf{A}_0 - \sigma_0^2\mathbf{M}_0) = \mathrm{tr}\mathbf{A}_0 - \frac{\mathrm{tr}(\mathbf{A}_0^*\mathbf{M}_0)}{2\det\mathbf{M}_0}\mathrm{tr}\mathbf{M}_0 =$$
$$= \frac{4\tan\alpha_0}{1+8\tan\alpha_0}\mathrm{tr}\left((\mathbf{I} - (1+4\tan\alpha_0)\mathbf{M}_1^*)\mathbf{A}_0\right). \tag{5.37}$$

Evidently, one of the roots is $\alpha_0 = 0$, corresponding to the case of the Beck column (which is the Pflüger column without the end mass). In this case, the cusp in the (η, γ)-plane is oriented vertically, see the upper left panel of Fig. 5.4. This confirms the well-known fact that for the Beck column the internal Kelvin-Voigt damping (η) is destabilizing, and the external air drag damping (γ) is stabilizing [11, 44, 51]. As soon as α_0 departs from zero, the external damping becomes a destabilizing factor due to the change in the orientation of the cusp in Fig. 5.4. Nevertheless, at a specific mass distribution $\alpha_0 \approx 0.342716$, which is given by the root of the equation

$$\mathrm{tr}\left[(\mathbf{I} - (1+4\tan\alpha_0)\mathbf{M}_1^*)\mathbf{A}_0\right] = 0,$$

the cusp restores its vertical orientation, as is visible in the lower left panel in Fig. 5.4. For this specific mass ratio the external damping is stabilizing again.

The revealed behaviour of the stabilizing damping ratio as a function of the mass distribution is reflected in Fig. 5.2(left) that shows the red solid curve of the onset of the reversible-Hopf bifurcation in the undamped system together with the onset of the classical-Hopf bifurcation in the limit of vanishing (the green dash-dotted curve) internal damping and (the blue dashed curve) external damping. The latter curve has two common points with the stability boundary of the undamped system exactly at $\alpha_0 = 0$ and $\alpha_0 \approx 0.342716$.

Remarkably, β_0 and its sign determine which mode will be destabilized by either of the two damping mechanisms or by their combination. For instance, in the case of $\beta_0 > 0$ the cusp of the stability boundary in the (η, γ)-plane is directed to the first quadrant, Fig. 5.4(upper right). Therefore, a dominating external damping will destabilize the mode with the higher frequency, whereas a dominating internal damping will destabilize the mode with the lower frequency, see Fig. 5.2(right). In the case of $\beta_0 < 0$

the cusp is oriented towards the second quadrant, Fig. 5.4(lower right), so that for every choice of internal and external damping with $\eta > 0$ and $\gamma > 0$, the mode with the lower frequency will be the destabilizing one.

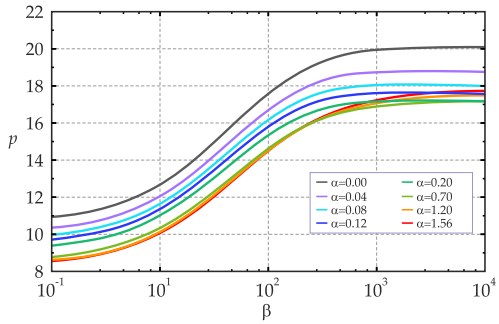

Figure 5.5: Each curve, computed with the use of the Eq.(5.31), shows the critical flutter load in the limit of vanishing dissipation as a function of the damping ratio β for the discretized model with $N = 2$ and $\chi = 1$ and corresponds to a different mass ratio α (reported in the legend). Note that at large mass ratios $0.7 \lesssim \alpha \leq \pi/2$ the curves form a dense family.

Finally, using Eq.(5.31), the critical flutter load in the limit of vanishing dissipation is plotted in Fig. 5.5 as a function of the damping ratio β, for different mass ratios $\alpha \in [0, \pi/2]$. It is worth noting that in the range $0.7 \leq \alpha \leq \pi/2$ the curves form a dense family. According to Fig. 5.3(right), for $0.342716 \leq \alpha_0 \leq \pi/2$ the stabilizing damping ratio β_0 is negative and tends to infinity as $\alpha_0 \to +0.342716\ldots$, which corresponds to the vertically oriented cusp in the lower left panel of Fig. 5.4.

5.3.7 Agreement with the solution of the boundary eigenvalue problem Eq.(5.12)

When N is increased, the eigenvalues, eigenvectors, and stability boundary based on the finite-dimensional approximation (5.16) converge to those solutions of the eigenvalue problem (5.12). However, already the $N = 2$ approximation is in an excellent qualitative agreement and in a very rea-

sonable quantitative agreement with the solution of Eq.(5.12). For completeness, Appendix C.2 reports the perturbation formulas for the singular flutter boundary, which are valid for arbitrary dimension N of the discretized model.

5.4 Experimental detection of the singular flutter limit

Inspired by the Ziegler set-up [22], the 'flutter machine' (Fig. 4.3) has been designed and realized to induce a follower force at the end of a Pflüger column. As already discussed in Chapter 4, the force (whose magnitude is continuously acquired with a miniaturized load cell) is produced by friction generated through sliding of a freely rotating wheel against a conveyor belt and can be calibrated as proportional (through the Coulomb friction rule) to a vertical load (provided via frictionless contact with a glass plate, loaded through a pulley system) pressing the wheel against the conveyor belt (which was set at a constant speed of 0.1 m/s in all experiments).

Looking in detail to dampings, during vibration of a rod two types of dissipations arise: an external (due to the air drag) and an internal (due to the viscosity of the constitutive material of the rod) damping. Often external and internal damping are condensed in a single coefficient [88, 89], but it was shown [36, 51] that for problems of flutter a careful distinction has to be maintained between the different sources of damping, as both strongly influence results. Therefore, experiments were performed to identify the two damping parameters introduced in the model, namely, a viscous modulus E^* (modelling the internal damping) and an air drag coefficient K (corresponding to a distributed external damping). To this purpose, the viscoelastic rod used for the flutter experiments was mounted on a shaker in a cantilever configuration and the acceleration of its free end measured when the basis was imposed a sinusoidal displacement of a frequency corresponding to the first two modes of resonance (see Appendix B.2 for details). Results from these experiments were used with a modified logarithmic decrement approach detailed in Appendix B.3, to obtain the following values of the

internal and external damping coefficients: $E^* = 2.139796 \cdot 10^6\, kg\, m^{-1} s^{-1}$ and $K = 1.75239 \cdot 10^{-5}\, kg\, m^{-1} s^{-1}$.

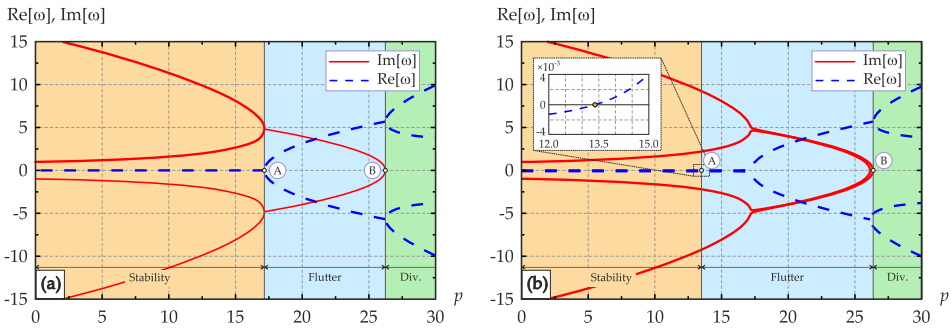

Figure 5.6: Pulsation (solid red curves) and growth rates (dashed blue curves) for the Pflüger column versus the dimensionless load p (left) without damping and (right) in the presence of a Kelvin-Voigt damping for the material (η) and air drag (γ), demonstrating the drop in the onset of flutter. The plots were obtained with the parameters representative of sample 5 in Table 4.1.

The experiments are compared with the numerical solution of the boundary eigenvalue problem (5.12). The roots of the characteristic equation (5.15) are the eigenvalues ω governing the vibrations of the Pflüger column. The first two eigenvalues with their conjugates are plotted in Fig. 5.6 versus the load p, with all the other parameters kept fixed. In the absence of both the Kelvin-Voigt damping (η) and the air drag (γ), the Pflüger column is a reversible system and loses stability by flutter via collision of imaginary eigenvalues in a linear reversible-Hopf bifurcation, Fig. 5.6(left). In the presence of the two dissipation mechanisms, the merging of modes is imperfect, thus yielding flutter through the classical Hopf bifurcation at a value of p significantly lower than in the case when the dissipation source is absent, Fig. 5.6(right). The theory of the previous section predicts that when the damping coefficients tend to zero while their ratio is kept constant, a limiting value of the flutter onset is reached, which generically differs from the flutter onset of the undamped column, thus justifying the numerical results

of [51].

The critical flutter load for the Pflüger column was experimentally investigated covering a wide range of values of the mass ratio α, (look to Table 4.1). Note that, since E^* and K are constant, the geometry of the tested rods parameterizes the dimensionless damping coefficients η and γ according to Eqs.(5.10), so that different values of γ and η are obtained for rods of different length (l) and thickness (b).

The results of the measurements, together with the analitycal calculations [9, 51], are shown in Fig. 5.7 for eleven samples (see Table 4.1) in the plane p versus α. Theoretical critical curves, pertaining to samples of different lengths and thicknesses, are plotted and highlighted for the relevant intervals of α. These boundaries are well-separated from the flutter boundary of the undamped system, represented by the upper dashed curve. In cases when either $\eta = 0$ (the dot-dashed curves) or $\gamma = 0$ (the lower dashed curves) the difference between the flutter boundaries corresponding to samples of various geometry is hardly visible, as it should be, in agreement with the theory, when the damping coefficients are very small [1, 9, 27, 29, 51]. In contrast, when both damping mechanisms are taken into account, the critical curves dramatically differ for samples of different length and thickness. This is because the *ratio* $\beta = \gamma/\eta = (K/E^*)(l^4/J)$ between the two damping coefficients increases almost 25 times from the first sample to the eleventh (see Table 4.1), although the damping coefficients γ and η vary weakly with the sample geometry.

Assuming $\gamma = \beta\eta$ in Eq.(5.15) and fixing η to be one of the values reported in Table 4.1, the flutter boundary is plotted in Fig. 5.8 in the p versus β representation. Since for every length and thickness the critical flutter load depends weakly on α, see Fig. 5.7, the flutter boundaries in Fig. 5.8, inset (a), are situated very close to each other (cf. Fig. 5.5). If the results of the measurements are superimposed, the experimental points perfectly fit this family of boundaries, within the error bands. Both the theoretical curves and the experimental points lie below the critical values of the undamped system for all values of α. Nevertheless, the critical flutter load of the weakly damped Pflüger column is very sensitive to the damping ratio and increases as β increases with the tendency to touch the lowest

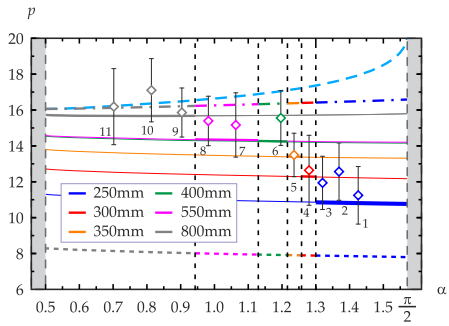

Figure 5.7: Critical flutter load p versus mass ratio α. Theoretical predictions based on Eq.(5.15) are plotted (the upper dashed curve) when damping is absent, when only external (γ, dot-dashed lines) or internal (η, lower dashed lines) damping is present, and (solid lines) when both damping mechanisms are present. Experimental results are marked by diamonds with error bars. The tested samples are numerated and their characteristics reported in Table 4.1.

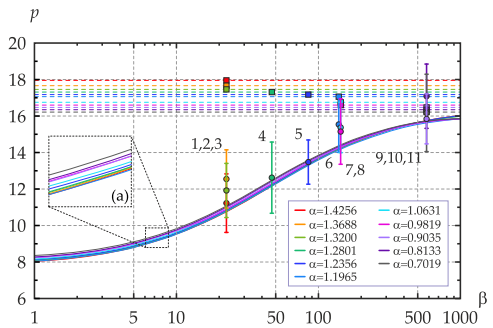

Figure 5.8: Solid curves mark the critical flutter load versus damping ratio $\beta = \gamma/\eta$ at different values of mass ratio α and corresponding fixed values of η, see Table 4.1. The experimental data are shown by spots with error bars. Dashed lines indicate the critical flutter load of the undamped Pflüger column for the same values of α.

of the ideal flutter boundaries at $\beta > 1000$, where the critical loads of the damped and undamped system tend to coincide (within the error bands),

Fig. 5.8.

5.4.1 The flutter modes

The analysis of the experiments is complemented by the determination of the flutter modes, which can be pursued by calculating the eigenvectors associated to the eigenvalues solutions of Eq.(5.15). The knowledge of the flutter modes is in fact useful to identify the shape of the vibrating rod during experiments and recognise which kind of instability is occuring. The analysis of the eigenvectors is reported in Fig. 5.9, relative to the first (lower frequency) vibration branch for the sample n. 5 of Table 4.1, with dimensionless dampings $\eta = 0.557 \cdot 10^{-3}$ and $\gamma = 48.368 \cdot 10^{-3}$. All modes 1-3 in the figures refer to stable vibrations, while the onset of flutter corresponds to the mode numbered 4 and the onset of divergence to the mode numbered 9.

It is evident from Fig. 5.9 that the shape of the vibration mode corresponds (as it should be) at null p to the free vibrations of a cantilever rod with a concentrated mass on its tip, vibrating at first resonance frequency. When the load p increases beyond the threshold of the classical-Hopf bifurcation and approaches the higher value of the load corresponding to the threshold of the reversible-Hopf bifurcation in the undamped case, the vibrations become more and more similar to the second vibration mode of the free cantilever rod. This is not surprising in view of the fact that in the undamped case the eigenvectors of the first and the second mode merge at the flutter threshold because of the formation of a double imaginary eigenvalue with the Jordan block. In all the performed experiments the modes sketched in Fig. 5.9 have been observed (a comparison between experiments and correspondent eigenvector is reported in Fig. 4.7). Moreover, if the load is increased further, the linearized theory predicts a 'second mode' of flutter and divergence, occuring at higher frequencies. The shape of the vibration modes (reported in Fig. 5.10) are more similar to the third and fourth vibration mode of the free cantilever rod. These modes can not be observed in experiments because flutter and divergences occur at lower frequencies.

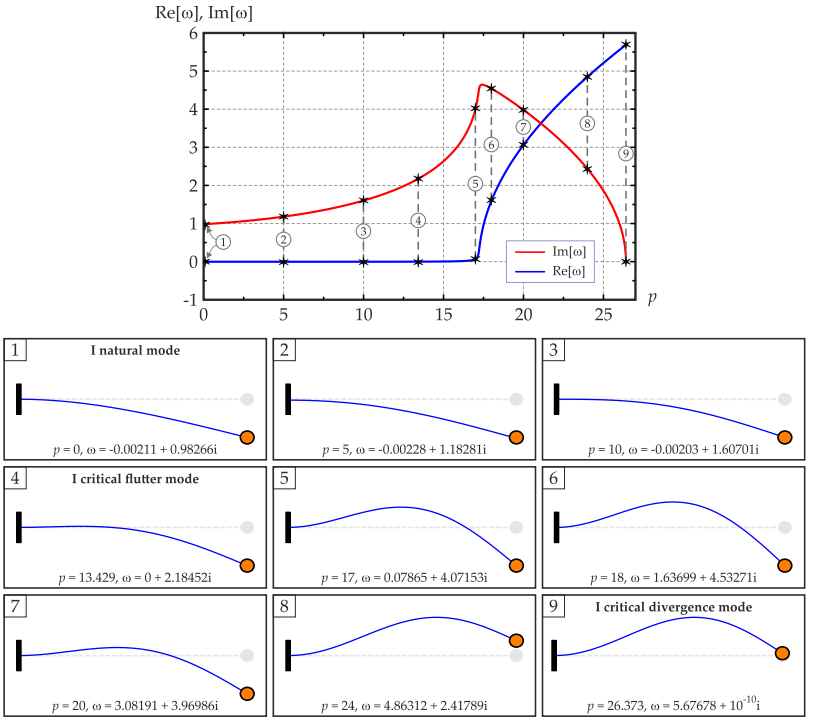

Figure 5.9: Real and imaginary part of the eigenfrequencies associated to the first (lower frequency) flutter branch (on the left). Each number corresponds to a value of the tangential load p for which the relevant eigenvector is computed and reported below in separate boxes. The vibrations numbered 1 to 3 are stable. Flutter instability first occurs at the load for which the mode numbered 4 is reported. Divergence instability first occurs at the load for which the mode numbered 9 is reported.

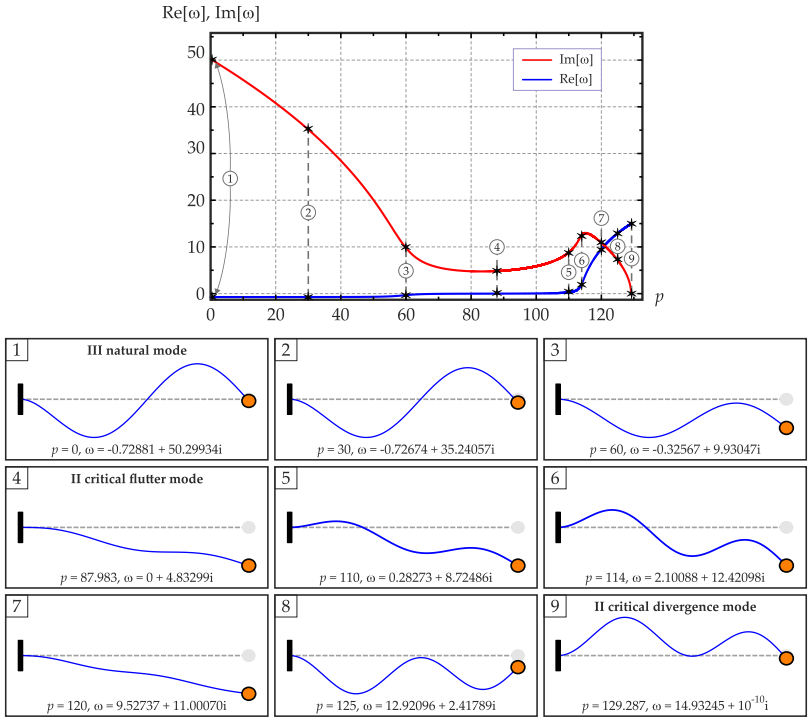

Figure 5.10: Real and imaginary part of the eigenfrequencies associated to the second (lower frequency) flutter branch. Each number corresponds to a value of the tangential load p for which the relevant eigenvector is computed and reported below in separate boxes. The vibrations numbered 1 to 3 are stable. The second flutter instability first occurs at the load for which the mode numbered 4 is reported. The second divergence instability first occurs at the load for which the mode numbered 9 is reported.

Appendix A

A.1 Brief overview on the role of external damping

A critical review of the relevant literature is given in this Appendix, with the purpose of explaining the historical origin of the misconception that the external damping introduces a mere stabilizing effect for structures subject to flutter instability.

Plaut [34] considered the Ziegler double pendulum with $m_1 = 2m_2$, without internal damping (in the joints), but subjected to an external damping proportional to the velocity along the rigid rods of the double pendulum[1]. In this system the critical flutter load increases with an increase in the external damping, so that they presented a plot showing that the flutter load converges to a value which is very close to P_u^-. However, they did not calculate the critical value in the *limit* of vanishing external damping, which would have revealed a value slightly smaller than the value corresponding to the undamped system[2]. In a subsequent work, Plaut [35] confirmed his

[1] Note that different mass distributions were never analyzed in view of external damping effect. In the absence of damping, stability investigations were carried out by Oran [37] and Kirillov [38].

[2] In fact, the flutter load of the externally damped Ziegler double pendulum with

previous result and demonstrated that internal damping with equal damping coefficients destabilizes the Ziegler double pendulum, whereas external damping has a stabilizing effect, so that it does not lead to the destabilization paradox. Plaut reports a stability diagram (in the external versus internal damping plane) that implicitly indicates the existence of the Whitney umbrella singularity on the boundary of the asymptotic stability domain. These conclusions agreed with other studies on the viscoelastic cantilevered Beck's column [2], loaded by a follower force which displays the paradox only for internal Kelvin-Voigt damping [31, 32, 34, 44] and were supported by studies on the abstract settings [39, 90, 91], which have proven the stabilizing character of external damping, assumed to be proportional to the mass [11, 92].

The Pflüger column [9] (a generalization of the Beck problem in which a concentrated mass is added to the loaded end, see also Sugiyama [42], Pedersen [41] and Chen [52]) was analyzed by Sugiyama [21] and Ryu [43], who numerically found that the internal damping leads to the destabilization paradox for all ratios of the end mass to the mass of the column. The role of external damping was investigated only by Detinko [40] who concludes that large external damping provides a stabilizing effect.

The stabilizing role of external damping was questioned only in the work by Panovko [93], in which the Ziegler double pendulum and the Beck column were considered with a dash-pot damper attached to the loaded end (a setting in which the external damper can be seen as something different than an air drag, but as merely an additional structural element, as suggested by [92]). In fact the dash-pot was shown to always yield the destabilization paradox, even in the presence of internal damping, no matter what the ratio is between the coefficients of internal and external damping [15, 94].

In summary, there is a well-established opinion that external damping stabilizes structures loaded by nonconservative positional forces.

$m_1 = 2m_2$, considered by Plaut [34] and Plaut [35] tends to the value $P = 2$ which is smaller than $P_u^- \approx 2.086$, therefore revealing the paradox.

A.2 Stability condition of a general 2 d.o.f. system

Kirillov [39] considered the stability of the system

$$\mathbf{M}\ddot{\mathbf{x}} + \varepsilon\mathbf{D}\dot{\mathbf{x}} + \mathbf{K}\mathbf{x} = 0, \tag{A.1}$$

where $\varepsilon > 0$ is a small parameter and $\mathbf{M} = \mathbf{M}^T$, $\mathbf{D} = \mathbf{D}^T$, and $\mathbf{K} \neq \mathbf{K}^T$ are real matrices of order n. In the case $n = 2$, the characteristic polynomial of the system (A.1),

$$q(\sigma, \varepsilon) = \det(\mathbf{M}\sigma^2 + \varepsilon\mathbf{D}\sigma + \mathbf{K}),$$

can be written by means of the Leverrier algorithm (adopted for matrix polynomials by Wang [95]) in a compact form:

$$q(\sigma,\varepsilon) = \det\mathbf{M}\sigma^4 + \varepsilon\mathrm{tr}(\mathbf{D}^*\mathbf{M})\sigma^3 + (\mathrm{tr}(\mathbf{K}^*\mathbf{M}) + \varepsilon^2\det\mathbf{D})\sigma^2 + \varepsilon\mathrm{tr}(\mathbf{K}^*\mathbf{D})\sigma + \det\mathbf{K}, \tag{A.2}$$

where $\mathbf{D}^* = \mathbf{D}^{-1}\det\mathbf{D}$ and $\mathbf{K}^* = \mathbf{K}^{-1}\det\mathbf{K}$ are adjugate matrices and tr denotes the trace operator.

Let us assume that at $\varepsilon = 0$ the undamped system (A.1) with $n = 2$ degrees of freedom be on the flutter boundary, so that its eigenvalues are imaginary and form a double complex-conjugate pair $\sigma = \pm i\omega_0$ of a Jordan block. In these conditions, the real critical frequency ω_0 at the onset of flutter follows from $q(\sigma, 0)$ in the closed form [15]

$$\omega_0^2 = \sqrt{\frac{\det\mathbf{K}}{\det\mathbf{M}}}. \tag{A.3}$$

A dissipative perturbation $\varepsilon\mathbf{D}$ causes splitting of the double eigenvalue $i\omega_0$, which is described by the Newton-Puiseux series $\sigma(\varepsilon) = i\omega_0 \pm i\sqrt{h\varepsilon} + o(\varepsilon)$, where the coefficient h is determined in terms of the derivatives of the polynomial $q(\sigma, \varepsilon)$ as

$$h := \frac{dq}{d\varepsilon}\left(\frac{1}{2}\frac{\partial^2 q}{\partial\sigma^2}\right)^{-1}\Bigg|_{\varepsilon=0,\,\sigma=i\omega_0} = \frac{\mathrm{tr}(\mathbf{K}^*\mathbf{D}) - \omega_0^2\mathrm{tr}(\mathbf{D}^*\mathbf{M})}{4i\omega_0\det\mathbf{M}}. \tag{A.4}$$

Since the coefficient h is imaginary, the double eigenvalue $i\omega_0$ splits generically into two complex eigenvalues, one of them with the positive real part yielding flutter instability [39]. Consequently, $h = 0$ represents a *necessary condition* for $\varepsilon\mathbf{D}$ to be a *stabilizing perturbation* [39].

In the case of the system (3.3), with matrices (3.5), it is readily obtained

$$\omega_0^2 = \frac{k}{l^2\sqrt{m_1 m_2}}. \tag{A.5}$$

Assuming $\mathbf{D} = \mathbf{D}_i$, Eq.(A.4) and the representations (3.5) and (A.5) yield

$$h = h_i := \frac{i}{m_1 l^2}\frac{5\mu - 2\sqrt{\mu} + 1}{4\mu}, \tag{A.6}$$

so that the equation $h_i = 0$ has as solution the complex-conjugate pair $\mu = (-3 \pm 4i)/25$. Therefore, for *every* real mass distribution $\mu \geq 0$ the dissipative perturbation with the matrix $\mathbf{D} = \mathbf{D}_i$ of internal damping results to be destabilizing.

Similarly, Eq.(A.4) with $\mathbf{D} = \mathbf{D}_e$ and representations (A.5), (3.5), and $F = F_u^-(\mu)$ yield

$$h = h_e := \frac{il}{48m_1}\frac{8\mu^2 - 11\sqrt{\mu^3} - 6\mu + 5\sqrt{\mu}}{\mu^2}, \tag{A.7}$$

so that the constraint $h_e = 0$ is satisfied only by the two following real values of μ

$$\mu_A \approx 0.273, \quad \mu_C \approx 2.559. \tag{A.8}$$

The mass distributions (A.8) correspond exactly to the points A and C in Fig. 3.1, which are common for the flutter boundary of the undamped system and for that of the dissipative system in the limit of vanishing external damping. Consequently, the dissipative perturbation with the matrix $\mathbf{D} = \mathbf{D}_e$ of external damping can have a stabilizing effect for *only two* particular mass distributions (A.8). Indeed, as it is shown in the present article,

the external damping is destabilizing for every $\mu \geq 0$, except for $\mu = \mu_A$ and $\mu = \mu_C$.

Consequently, the stabilizing or destabilizing effect of damping with the given matrix $\mathbf{D}$ is determined not only by its spectral properties, but also by how it 'interacts' with the mass and stiffness distributions. The condition which selects possibly stabilizing triples ($\mathbf{M}$, $\mathbf{D}$, $\mathbf{K}$) in the general case of $n = 2$ degrees of freedom is therefore the following

$$\mathrm{tr}(\mathbf{K}^*\mathbf{D}) = \omega_0^2 \mathrm{tr}(\mathbf{D}^*\mathbf{M}). \tag{A.9}$$

Appendix B

B.1 Flutter and divergence instability in the Pflüger column

The analysis of flutter and divergence instability in the Pflüger column is here continued from Eqs.(4.3)–(4.9). In particular, following the time-harmonic assumption of (4.9), Eq.(4.8) yields a linear differential equation for $\tilde{v}(\xi)$, with the characteristic equation

$$\lambda^4(1+\eta\omega) + \lambda^2 p + \gamma\omega + \omega^2 = 0, \tag{B.1}$$

which admits the solutions

$$\lambda_{1,2}^2 = \frac{\sqrt{p^2 - 4(1+\eta\omega)(\gamma\omega+\omega^2)} \mp p}{2(1+\eta\omega)}. \tag{B.2}$$

Therefore, the solution for $\tilde{v}$ can be written in the form

$$\tilde{v}(\xi) = A_1 \sinh(\lambda_1\xi) + A_2 \cosh(\lambda_1\xi) + A_3 \sin(\lambda_2\xi) + A_4 \cos(\lambda_2\xi), \tag{B.3}$$

where A_i $(i = 1, .., 4)$ are arbitrary constants.

The boundary conditions of Eq.(4.6) can be rewritten in a dimensionless form as

$$\begin{aligned}
&\tilde{v}(0) = \tilde{v}'(0) = 0 && \text{at the clamped end,}\\
&\tilde{v}''(1) = 0 && \text{at the loaded end,}\\
&(1+\eta\omega)\tilde{v}'''(1) - (\chi-1)\tilde{v}'(1)p - \omega^2\tan(\alpha)\tilde{v}(1) = 0 && \text{at the loaded end,}
\end{aligned} \tag{B.4}$$

where $\chi = 1 - \bar{\chi}$ represents the inclination of the applied dimensionless tangential force p. A substitution of the boundary conditions (B.4) in the solution (B.3) yields an algebraic system of equations which admits non-trivial solutions at the vanishing of the determinant of the matrix of coefficients

$$\begin{bmatrix}
0 & 1 & 0 & 1\\
\lambda_1 & 0 & \lambda_2 & 0\\
\lambda_1^2\sinh\lambda_1 & \lambda_1^2\cosh\lambda_1 & -\lambda_2^2\sin\lambda_2 & -\lambda_2^2\cos\lambda_2\\
a_{41} & a_{42} & a_{43} & a_{44}
\end{bmatrix} \tag{B.5}$$

where

$$\begin{aligned}
a_{41} &= (1+\eta\omega)\lambda_1^3\cosh\lambda_1 - (\chi-1)p\lambda_1\cosh\lambda_1 - \omega^2\tan\alpha\sinh\lambda_1,\\
a_{42} &= (1+\eta\omega)\lambda_1^3\sinh\lambda_1 - (\chi-1)p\lambda_1\sinh\lambda_1 - \omega^2\tan\alpha\cosh\lambda_1,\\
a_{43} &= -(1+\eta\omega)\lambda_2^3\cos\lambda_2 - (\chi-1)p\lambda_2\cos\lambda_2 - \omega^2\tan\alpha\sin\lambda_2,\\
a_{44} &= (1+\eta\omega)\lambda_2^3\sin\lambda_2 + (\chi-1)p\lambda_2\sin\lambda_2 - \omega^2\tan\alpha\cos\lambda_2.
\end{aligned} \tag{B.6}$$

Noting that the λ_i's are functions of the applied load p, the pulsation ω, the viscosity η, and the external damping γ, the vanishing of the determinant of (B.5) corresponds to the frequency equation

$$f(p, \omega, \alpha, \gamma, \eta, \chi) = 0, \tag{B.7}$$

which in explicit form reads

$$\begin{aligned} f(p,\omega,\alpha,\gamma,\eta,\chi) \quad &= \lambda_1\lambda_2(1+\eta\omega)(\lambda_1^4+\lambda_2^4)+\lambda_1\lambda_2 p(\chi-1)(\lambda_2^2-\lambda_1^2)+ \\ &+\lambda_1\lambda_2[2(1+\eta\omega)\lambda_1^2\lambda_2^2-p(\chi-1)(\lambda_2^2-\lambda_1^2)]\cosh\lambda_1\cos\lambda_2+ \\ &+\lambda_1^2\lambda_2^2[2p(\chi-1)+(1+\eta\omega)(\lambda_2^2-\lambda_1^2)]\sinh\lambda_1\sin\lambda_2+ \\ &-\omega^2\tan\alpha(\lambda_1^2+\lambda_2^2)[\lambda_2\sinh\lambda_1\cos\lambda_2-\lambda_1\cosh\lambda_1\sin\lambda_2]. \end{aligned} \tag{B.8}$$

For given values of the parameters χ, η, and γ (which were identified from experiments), the transcendental equation (B.7) describes the boundaries for which flutter occurs and for which divergence occurs. In particular, the system is unstable by divergence when the pulsation ω is real and positive, while flutter instability occurs for complex ω with $\mathrm{Re}[\omega]>0$.

Is important to remark that if the mass ratio α is set to zero (which means the elimination of the concentrated mass at the free end of the rod) the transcendental equation (B.8) describes the stability threshold of the Beck column, for which divergence instability does not occur.

B.2 Dampings identification

In the present study, two sources of damping have been accounted for in Eq.(4.5), a damping internal to the rod via parameter E^* of Eq.(4.3), and another due to the air drag via parameter K in the equations of motion (4.5). Often these two damping sources are condensed in a single coefficient, see Chopra [88] and Clough & Penzien [89], but it is well-known that in problems of flutter a careful distinction has to be maintained between the different sources of damping [40].

Therefore, experiments have been performed to identify the viscous modulus E^* which accounts for the internal damping and the coefficient K parametrizing the external damping due to air drag. To this purpose, the elastic rod used for the flutter experiments was mounted on a shaker (Tira vib 51144, frequency range 2-6500 Hz, equipped with a Power Amplifier

Tira BAA 1000) in a cantilever configuration. On the free end of the rod an accelerometer (352A24 from PCB Piezotronics) was positioned and a sinusoidal base displacement $\delta(t)$, with a maximum amplitude of 10 mm, was imposed at the clamped end of the rod. The shaker was tuned to the first and second resonance mode, as shown in Fig. B.1, until a steady state was reached. Subsequently, the shaker was turned off and the oscillations of the free end of the cantilever rod were monitored. The data acquired from the accelerometer mounted on the free end were employed in a modified logarithmic decrement approach (details on this method are reported in B.3) in order to obtain two distinct damping ratios ζ. Eventually the following values were computed for the internal and external damping coefficients, namely $E^* = 2.139796 \cdot 10^6\, kg\, m^{-1} s^{-1}$ and $K = 1.75239 \cdot 10^{-5}\, kg\, m^{-1} s^{-1}$, respectively.

The identified damping parameters were eventually validated through the following additional experiment: a displacement of 50 mm was imposed at the end of the viscoelastic rod, in a cantilever configuration, with the aid of a wire. The motion of the rod arising from the sudden cut of the wire was recorded with a high-speed camera (Sony high-speed camera, model PXW-FS5). A circular marker, applied at the end of the beam, was tracked frame by frame with an appropriate code implemented in Mathematica. The motion of the rod was then simulated with a computational model implemented in ABAQUS Standard 6.13-2, assuming the two previously evaluated damping parameters. The experimental and the computational results (reported in light blue and red in Fig. B.1, respectively) were found in good agreement, so that the estimated damping parameters were successfully validated.

B.3 Modified logarithmic decrement approach

The scope of the present Section is to detail the identification technique employed to evaluate the external and internal damping coefficients. The free vibrations of a viscoelastic rod is governed by Eq.(4.5) with $P = 0$,

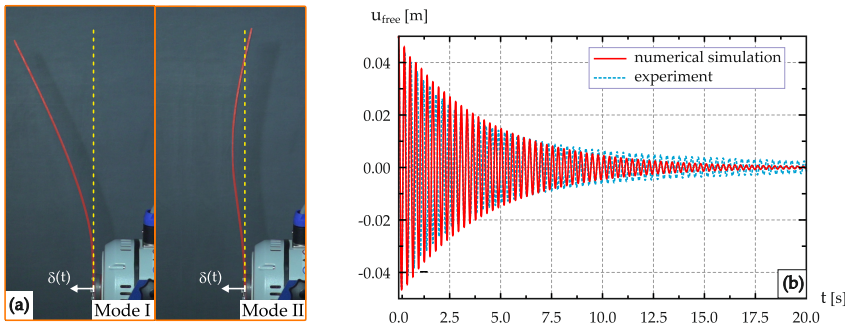

Figure B.1: Identification of the internal and external damping coefficients for an oscillating rod. (a) The experimental setup showing a rod mounted on a shaker in a cantilever configuration, which vibrates in the first and second resonant mode while a sinusoidal displacement $\delta(t)$ of amplitude 10 mm is applied at the clamp. Using this setup, after a steady state regime was reached, the shaker was turned off and the oscillations of the free end were monitored. With the data acquired, and using a modified logarithmic decrement approach, two damping ratios ζ were identified. Eventually the damping coefficients E^* and K were calculated. (b) These coefficients have been eventually validated by imposing and suddenly releasing a displacement of 50 mm at the end of the rod in a cantilever configuration. The subsequent motion of the rod end was recorded with a high-speed camera and tracked with a software developed using Mathematica. The outcome of the experiment was compared with the simulations obtained with a model of the rod implemented in ABAQUS Standard 6.13-2. The good agreement between the experiment and the simulation validates the adopted identification procedure.

which can be rewritten as

$$EJv'''' + E^*J\dot{v}'''' + K\dot{v} + m\ddot{v} = 0. \tag{B.9}$$

Before analyzing the case in which the clamped end of the rod is subject to a sinusoidal excitation of pulsation $\bar{\omega}$ (which will be relevant for the identification of the damping coefficients), free vibrations are considered of the cantilever configuration with fixed clamp.

B.3.1 Free vibration of a cantilever rod

Free vibrations of a viscoelastic cantilever rod are analyzed assuming time-harmonic solutions in the form $v(x,t) = Y(x)\exp(-i\omega t)$ [notice the slight difference with respect to the representation of Eq.(4.9)], yielding

$$\sum_{n=1}^{\infty} Y_n^{IV} - \Lambda_n^4 Y_n = 0, \tag{B.10}$$

where the coefficients Λ_n^4 are real quantities defined as

$$\Lambda_n^4 = \frac{m\omega_n^2 + i\omega_n K}{EJ - i\omega_n E^* J}. \tag{B.11}$$

The solution of Eq.(B.10) under the time-harmonic assumption can be represented as

$$Y(x) = \sum_{n=1}^{\infty} Y_n(x) = \sum_{n=1}^{\infty} C_{1,n}\sin\Lambda_n x + C_{2,n}\cos\Lambda_n x + C_{3,n}\sinh\Lambda_n x + C_{4,n}\cosh\Lambda_n x, \tag{B.12}$$

where the constants $C_{i,n}$ depend on the boundary conditions, which for a cantilever rod read

$$Y(0) = Y'(0) = Y''(l) = Y'''(l) = 0. \tag{B.13}$$

A substitution of Eqs.(B.13) in the representation (B.12) leads to

$$\begin{bmatrix} 0 & 1 & 0 & 1 \\ \Lambda_n & 0 & \Lambda_n & 0 \\ -\Lambda_n^2\sin\Lambda_n l & -\Lambda_n^2\cos\Lambda_n l & \Lambda_n^2\sinh\Lambda_n l & \Lambda_n^2\cosh\Lambda_n l \\ -\Lambda_n^3\cos\Lambda_n l & \Lambda_n^3\sin\Lambda_n l & \Lambda_n^3\cosh\Lambda_n l & \Lambda_n^3\sinh\Lambda_n l \end{bmatrix} \begin{pmatrix} C_{1,n} \\ C_{2,n} \\ C_{3,n} \\ C_{4,n} \end{pmatrix} = \begin{pmatrix} 0 \\ 0 \\ 0 \\ 0 \end{pmatrix}. \tag{B.14}$$

The first two equations yield $C_{4,n} = -C_{2,n}$ and $C_{3,n} = -C_{1,n}$, so that the algebraic system reduces to

$$\begin{bmatrix} \Lambda_n^2(\sin\Lambda_n l + \sinh\Lambda_n l) & \Lambda_n^2(\cos\Lambda_n l + \cosh\Lambda_n l) \\ \Lambda_n^3(\cos\Lambda_n l + \cosh\Lambda_n l) & \Lambda_n^3(-\sin\Lambda_n l + \sinh\Lambda_n l) \end{bmatrix} \begin{pmatrix} C_{1,n} \\ C_{2,n} \end{pmatrix} = \begin{pmatrix} 0 \\ 0 \end{pmatrix}, \tag{B.15}$$

and imposing the determinant of the matrix to vanish provides

$$\cos\Lambda_n l \cosh\Lambda_n l = -1. \tag{B.16}$$

The just obtained transcendental equation defines the values

$$\Lambda_1 l = 1.875..., \quad \Lambda_2 l = 4.694..., \quad \Lambda_n l = \tfrac{\pi}{2}(2n-1). \tag{B.17}$$

Now, the solution (B.12) can be expressed in terms of one arbitrary constant $C_{2,n}$, such that

$$C_{1,n} = -\frac{\cos\Lambda_n l + \cosh\Lambda_n l}{\sin\Lambda_n l + \sinh\Lambda_n l} C_{2,n}, \tag{B.18}$$

which leads to the general solution for the free vibrations of a cantilever rod in the form

$$v(t,x) = \sum_{n=1}^{\infty} C_{2,n} Y_n(x) e^{-\omega_n^I t} \left(\cos\omega_n^R t + \frac{\omega_n^I}{\omega_n^R} \sin\omega_n^R t \right), \tag{B.19}$$

where the pulsation is split into the real ω_n^R and imaginary ω_n^I part, so that $\omega_n = \omega_n^R + i\,\omega_n^I$, and

$$Y_n(x) = \cos\Lambda_n x - \cosh\Lambda_n x - \frac{\cos\Lambda_n l + \cosh\Lambda_n l}{\sin\Lambda_n l + \sinh\Lambda_n l} (\sin\Lambda_n x - \sinh\Lambda_n x). \tag{B.20}$$

Notice that the free vibration solutions $Y_n(x)$ satisfy the orthogonality relations

$$\int_0^l Y_n(x)Y_h(x)dx = 0 \quad \text{for } h \neq n \tag{B.21}$$

and, because of Eq.(B.10), the property

$$Y_n^{IV}(x) = \Lambda_n^4 Y_n(x). \tag{B.22}$$

The following quantities, which will be useful later, are also introduced

$$\Gamma_n := \int_0^l Y_n^2(x)dx, \qquad \Gamma_n\Lambda_n^4 := \int_0^l Y_n^{IV}(x)Y_n(x)dx. \tag{B.23}$$

B.3.2 Cantilever rod with an imposed sinusoidal base displacement

A sinusoidal displacement of amplitude U_0, namely

$$\delta(t) = U_0 \sin \bar{\omega}t, \tag{B.24}$$

is prescribed at the clamp $x = 0$ of a viscoelastic rod in a cantilever configuration, in the presence of both internal and external damping. Under these conditions, the solution $u(x,t)$ can be written as the sum of a flexural displacement (function of space and time) $v(x,t)$ and the rigid-body motion (B.24)

$$u(x,t) = v(x,t) + \delta(t), \tag{B.25}$$

so that $v(0,t) = 0$. A substitution of Eq.(B.25) in the differential equation of motion (B.9) by neglecting the term $\ddot{\delta}(t)$ yields a differential equation for $v(x,t)$, that is

$$EJv'''' + E^*J\dot{v}'''' + K\dot{v} + m\ddot{v} = mU_0\bar{\omega}^2 \sin \bar{\omega}t. \tag{B.26}$$

Therefore, the effect of the movement at the clamp can be considered as the effect of a diffused load $f(t) = mU_0\bar{\omega}^2 \sin \bar{\omega}t$, defined per unit length of the rod.

The solution of Eq.(B.26) is the sum of the solution of the associated homogeneous equation (which governs the free vibrations of the rod) and a particular solution $v_p(x,t)$. The latter solution can be sought in the form

$$v_p(x,t) = \sum_{n=1}^{\infty} Y_n(x) y_n(t), \tag{B.27}$$

where the modal functions $Y_n(x)$ are defined by Eq.(B.20) and the $y_n(t)$ are for the moment unknown. A substitution of Eq.(B.27) into Eq.(B.26) yields

$$\sum_{n=1}^{\infty} Y_n''''(x) y_n(t) + \frac{E^*}{E} Y_n''''(x) \dot{y}_n(t) + \frac{K}{EJ} Y_n(x) \dot{y}_n(t) + \frac{m}{EJ} Y_n(x) \ddot{y}_n(t) = \frac{f(t)}{EJ}. \tag{B.28}$$

A multiplication of the previous equation by $Y_h(x)$ and an integration over the length of the rod l yields

$$\Gamma_n \Lambda_n^4 y_n(t) + \Gamma_n \left(\frac{K}{EJ} + \frac{E^*}{E} \Lambda_n^4 \right) \dot{y}_n(t) + \Gamma_n \frac{m}{EJ} \ddot{y}_n(t) = F_n \frac{f(t)}{EJ}, \tag{B.29}$$

where $F_n = \int_0^l Y_n(x) dx$. Eq.(B.29) is formally identical to the equation of motion which governs the oscillations of a single-degree-of-freedom system with a mass m_n, a damper of constant c_n and a spring of stiffness k_n

$$m_n \ddot{y}_n(t) + c_n \dot{y}_n(t) + k_n y_n(t) = p_n \sin \bar{\omega} t, \tag{B.30}$$

where

$$m_n = \Gamma_n \frac{m}{EJ}, \quad c_n = \Gamma_n \left(\frac{K}{EJ} + \frac{E^*}{E} \Lambda_n^4 \right), \quad k_n = \Gamma_n \Lambda_n^4, \quad p_n = F_n \frac{m U_0 \bar{\omega}^2}{EJ}. \tag{B.31}$$

It is expedient to rewrite Eq.(B.30) in the form

$$\ddot{y}_n(t) + 2\alpha_n \zeta_n \dot{y}_n(t) + \alpha_n^2 y_n(t) = a_n \sin \bar{\omega} t \tag{B.32}$$

where

$$\alpha_n^2 = \frac{k_n}{m_n} = \frac{EJ}{m}\Lambda_n^4, \quad 2\alpha_n\zeta_n = \frac{c_n}{m_n} = \frac{K}{m} + \frac{E^*J}{m}\Lambda_n^4, \quad a_n = \frac{p_n}{m_n} = \frac{F_n}{\Gamma_n}U_0\bar{\omega}^2. \tag{B.33}$$

The solution of the differential equation (B.32) consists of the sum of the solution of the associated homogeneous equation and of a particular integral, which can be found in the form

$$y_{n,part}(t) = A_n \sin\bar{\omega}t + B_n \cos\bar{\omega}t, \tag{B.34}$$

yielding

$$A_n = a_n\left[1 - \left(\frac{\bar{\omega}}{\alpha_n}\right)^2\right]N_n, \quad B_n = -2a_n\zeta_n\left(\frac{\bar{\omega}}{\alpha_n}\right)N_n, \tag{B.35}$$

where N_n is the so called dynamic amplification factor

$$N_n(\alpha_n, \zeta_n) = \frac{1}{\left[1 - \left(\frac{\bar{\omega}}{\alpha_n}\right)^2\right]^2 + \left[2\zeta_n\frac{\bar{\omega}}{\alpha_n}\right]^2}. \tag{B.36}$$

The solution of the homogeneous equation associated to Eq.(B.32) is

$$y_{n,hom}(t) = \exp(-\alpha_n\zeta_n t)\left(C_n \sin\alpha_{n,d}t + D_n\cos\alpha_{n,d}t\right), \tag{B.37}$$

where $\alpha_{n,d} = \alpha_n\sqrt{1-\zeta_n^2}$ are the damped pulsations of the system. As regards the coefficients C_n and D_n, these can be found by imposing the initial conditions

$$y_n(0) = X_0, \quad \dot{y}_n(0) = V_0 \tag{B.38}$$

where

$$y_n(t) = y_{n,hom}(t) + y_{n,part}(t), \tag{B.39}$$

leading to the expressions

$$C_n = \frac{1}{\alpha_{n,d}} \left[X_0 \alpha_n \zeta_n + V_0 + a_n \bar{\omega} N_n \left(\frac{\bar{\omega}^2}{\alpha_n^2} + 2\zeta_n^2 - 1 \right) \right], \quad D_n = X_0 + 2 a_n \zeta_n \frac{\bar{\omega}}{\alpha_n} N_n. \tag{B.40}$$

B.3.3 Identification procedure

The identification procedure is based on experiments in which the cantilevered rod is set in a steady oscillation at the n-th mode through excitation with a sinusoidal base motion. Starting from this situation, the base motion is stopped and the subsequent decaying oscillations are monitored. This transient motion is governed by Eq.(B.37), in which the sinusoidal part has a period $T = 2\pi/\alpha_{n,d}$. If the transient motion exhibits a peak of displacement at $t = t^*$, other peaks will occur at every cycle, even after s cycles. Therefore, the logarithmic decrement is defined as

$$\delta_s = \log \frac{y_{n,hom}(t^*)}{y_{n,hom}(t^* + 2\pi s/\alpha_{n,d})}, \tag{B.41}$$

a quantity which can be measured and satisfies the relation

$$\zeta_n = \frac{\delta_s}{2\pi s \alpha_n/\alpha_{n,d}} \approx \frac{\delta_s}{2\pi s}. \tag{B.42}$$

From Eq.$(B.33)_2$ the following identity is finally obtained

$$\frac{1}{\Lambda_n^2} \left(\frac{K}{J} + E^* \Lambda_n^4 \right) \sqrt{\frac{J}{mE}} = \frac{\delta_s}{\pi s}, \tag{B.43}$$

so that if δ_s is measured at cycle s for two modes of vibration ($n = 1$ and $n = 2$ have been used in our experiments) and J, E and m are known from independent evaluations, (B.43) provides two equations for the two unknown damping coefficients E^* and K. Note that the logarithmic decrement can be equivalently measured as the ratio between peak displacements or between accelerations, because the latter are proportional to the former through a constant.

Appendix C

C.1 Discretization

C.1.1 Adjoint boundary eigenvalue problems

The boundary eigenvalue problem for the Pflüger column with partial follower load is given by Eq.(5.12). The problem is self-adjoint only for $\chi = 0$ and non-self-adjoint otherwise. Indeed, integration by parts of the differential equation (5.12) together with the boundary conditions lead to the following adjoint boundary eigenvalue problem

$$\begin{gathered}(1+\eta\bar{\omega})\tilde{w}'''' + p\tilde{w}'' + (\gamma\bar{\omega}+\bar{\omega}^2)\tilde{w} = 0,\\ \tilde{w}(0) = \tilde{w}'(0) = 0, \quad \tilde{w}''(1)(1+\eta\bar{\omega}) + \chi p\tilde{w}(1) = 0,\\ (1+\eta\bar{\omega})\tilde{w}'''(1) + p\tilde{w}'(1) - \tilde{w}(1)\omega^2\tan\alpha = 0. \end{gathered} \tag{C.1}$$

The problem (C.1) coincides with (5.12) only for $\chi = 0$. Otherwise, the boundary conditions of the two problems differ.

C.1.2 Variational principle

Let us consider now the functional

$$I(\tilde{v},\tilde{w}) = \int_0^1 \left[(1+\eta\omega)\tilde{v}''''\tilde{w} + p\tilde{v}''\tilde{w} + (\gamma\omega+\omega^2)\tilde{v}\tilde{w}\right] d\xi. \tag{C.2}$$

Integrating by parts the first two terms in Eq.(C.2) and accounting for the boundary conditions for the problems Eqs.(5.12) and (C.1), leads to

$$\begin{aligned} \int_0^1 (\tilde{v}''')'\tilde{w}d\xi &= \int_0^1 \tilde{v}''\tilde{w}''d\xi + \tilde{v}'''(1)\tilde{w}(1), \\ \int_0^1 (\tilde{v}')'\tilde{w}d\xi &= -\int_0^1 \tilde{v}'\tilde{w}'d\xi + \tilde{v}'(1)\tilde{w}(1). \end{aligned} \tag{C.3}$$

On the other hand, the last of the boundary conditions (5.12) provides

$$(1+\eta\omega)\tilde{v}'''(1) + p\tilde{v}'(1) = \chi p\tilde{v}'(1) + \tilde{v}(1)\omega^2\tan\alpha.$$

Hence,

$$\begin{aligned} I = \int_0^1 \left[(1+\eta\omega)\tilde{v}''\tilde{w}'' - p\tilde{v}'\tilde{w}' + (\gamma\omega+\omega^2)\tilde{v}\tilde{w}\right] d\xi + \\ +\tilde{v}(1)\tilde{w}(1)\omega^2\tan\alpha + \chi p\tilde{v}'(1)\tilde{w}(1). \end{aligned} \tag{C.4}$$

Stationarity of this functional with respect to arbitrary smooth variations $\delta\tilde{v}$, $\delta\tilde{w}$, which satisfy kinematic boundary conditions, is equivalent to the boundary value problems (5.12), (C.1).

C.1.3 Discretization and reduced finite-dimensional model

Let us consider solutions to the self-adjoint problems (5.12) and (C.1), with $\chi = 0$, $p = 0$, $\eta = 0$, $\gamma = 0$, and $\alpha = 0$

$$\begin{aligned} \tilde{v}_j = \tilde{w}_j = \\ = \left|\frac{\sin\sqrt{\omega_j}}{1+(-1)^j\cos\sqrt{\omega_j}}\right| \left[\sin(\xi\sqrt{\omega_j}) - \sinh(\xi\sqrt{\omega_j}) + \right. \\ \left. -\frac{\sin(\sqrt{\omega_j})+\sinh(\sqrt{\omega_j})}{\cos(\sqrt{\omega_j})+\cosh(\sqrt{\omega_j})}\left(\cos(\xi\sqrt{\omega_j}) - \cosh(\xi\sqrt{\omega_j})\right)\right] \end{aligned} \tag{C.5}$$

where ω_j is a root of the characteristic equation

$$\cos(\sqrt{\omega})\cosh(\sqrt{\omega}) + 1 = 0,$$

which provides for instance,

$$\begin{aligned}
\omega_1 &= 3.516015269, \quad \sqrt{\omega_1} = 1.875104069 \\
\omega_2 &= 22.03449156, \quad \sqrt{\omega_2} = 4.694091132 \\
\omega_3 &= 61.69721441, \quad \sqrt{\omega_3} = 7.854757438 \\
&\cdots \\
\omega_n &= \frac{\pi^2}{4}(2n-1)^2, \quad \sqrt{\omega_n} = \frac{\pi}{2}(2n-1).
\end{aligned} \tag{C.6}$$

The functions (C.5) are orthogonal and normalized as follows:

$$\int_0^1 \tilde{v}_i(\xi)\tilde{v}_j(\xi)d\xi = 0, \quad i \neq j; \quad \int_0^1 \tilde{v}_i(\xi)\tilde{v}_i(\xi)d\xi = 1.$$

Therefore, the eigenmodes $\tilde{v}$ and $\tilde{w}$ can be represented in the form of the expansions

$$\tilde{v} \approx \sum_{j=1}^{N} a_j \tilde{v}_j(\xi), \quad \tilde{w} \approx \sum_{j=1}^{N} b_j \tilde{w}_j(\xi), \tag{C.7}$$

where $\tilde{w}_j = \tilde{v}_j$.

Substituting the expansions (C.7) into the functional (C.4) yields the discretized version of the functional (C.4)

$$
\begin{aligned}
I_N &= \omega^2 \sum_{i=1}^{N}\sum_{j=1}^{N} a_i b_j \left(\int_0^1 \tilde{v}_i \tilde{v}_j d\xi + \tilde{v}_i(1)\tilde{v}_j(1)\tan\alpha \right) \\
&+ \omega \sum_{i=1}^{N}\sum_{j=1}^{N} a_i b_j \int_0^1 \left[\eta \tilde{v}_i'' \tilde{v}_j'' + \gamma \tilde{v}_i \tilde{v}_j \right] d\xi \qquad \text{(C.8)} \\
&+ \sum_{i=1}^{N}\sum_{j=1}^{N} a_i b_j \left(\int_0^1 [\tilde{v}_i'' \tilde{v}_j'' - p\tilde{v}_i' \tilde{v}_j'] d\xi + \chi p \tilde{v}_i'(1)\tilde{v}_j(1) \right).
\end{aligned}
$$

The gradient of the discretized functional, I_N, calculated with respect to the vector of coefficients $\mathbf{b} = (b_1, b_2, \ldots, b_N)$, and equated to zero, provides the discretized eigenvalue problem for the Pflüger column

$$
(\mathbf{M}\omega^2 + (\gamma \mathbf{D}_e + \eta \mathbf{D}_i)\omega + \mathbf{K}_1 - p\mathbf{K}_2 + \chi p \mathbf{N})\mathbf{a} = 0, \qquad \text{(C.9)}
$$

where $\mathbf{a} = (a_1, a_2, \ldots, a_N)$ and the elements of the matrices are

$$
\begin{gathered}
M_{ij} = \int_0^1 \tilde{v}_i \tilde{v}_j d\xi + \tilde{v}_i(1)\tilde{v}_j(1)\tan\alpha \\
= \delta_{ij} + 4(-1)^{i+j}\tan\alpha, \\
D_{e,ij} = \int_0^1 \tilde{v}_i \tilde{v}_j d\xi = \delta_{ij}, \quad D_{i,ij} = \int_0^1 \tilde{v}_i'' \tilde{v}_j'' d\xi = \delta_{ij}\omega_j^2, \\
K_{1,ij} = \int_0^1 \tilde{v}_i'' \tilde{v}_j'' d\xi = \delta_{ij}\omega_j^2, \quad K_{2,ij} = \int_0^1 \tilde{v}_i' \tilde{v}_j' d\xi, \\
N_{ij} = \tilde{v}_i'(1)\tilde{v}_j(1) = \frac{4(-1)^{j+1}\sqrt{\omega_i}\sin\sqrt{\omega_i}}{1+(-1)^i\cos\sqrt{\omega_i}}, \qquad \text{(C.10)}
\end{gathered}
$$

with δ_{ij} denoting the Kronecker symbol. The entries of the matrix $\mathbf{K}_2$ in the explicit form are

$$
\begin{gathered}
i \neq j: \quad K_{2,ij} = A\left(\frac{\sqrt{\omega_j}\sin(\sqrt{\omega_i})}{\cos(\sqrt{\omega_i})(-1)^i+1} - \frac{\sqrt{\omega_i}\sin(\sqrt{\omega_j})}{\cos(\sqrt{\omega_j})(-1)^j+1} \right), \\
i = j: \quad K_{2,jj} = \frac{\omega_j\left((-1)^j - \cos\sqrt{\omega_j}\right) - 2\sqrt{\omega_j}\sin\sqrt{\omega_j}}{\cos\sqrt{\omega_j}+(-1)^j},
\end{gathered}
\qquad \text{(C.11)}
$$

where $A = \frac{4\sqrt{\omega_i\omega_j}}{(-1)^i\omega_i-(-1)^j\omega_j}$. All the matrices are real. In addition, the matrices of mass, $\mathbf{M}$, external damping, $\mathbf{D}_e$, internal damping, $\mathbf{D}_i$, and stiffness, $\mathbf{K}_1$ and $\mathbf{K}_2$, are symmetric. The matrix of nonconservative positional forces with non-zero curl, $\mathbf{N}$, is real and non-symmetric. Note that $\det \mathbf{M} = 1 + 4N \tan\alpha > 0$.

C.2 Perturbation formulas for arbitrary N

The eigenvalue problem (5.17) can be formulated as the eigenvalue problem

$$\mathbf{L}(\omega, \mathbf{k})\mathbf{a} = 0$$

for the matrix polynomial

$$\mathbf{L}(\omega, \mathbf{k}) := \mathbf{A}(p, \chi) + \mathbf{D}(\gamma, \eta)\omega + \mathbf{M}(\alpha)\omega^2,$$

where $\mathbf{k} = (p, \chi, \gamma, \eta, \alpha)$ is a vector of parameters. The adjoint matrix polynomial $\mathbf{L}^\dagger = \mathbf{A}^T + \mathbf{D}\overline{\omega} + \mathbf{M}\overline{\omega}^2$ is introduced, so that $(\mathbf{La}, \mathbf{b}) = (\mathbf{a}, \mathbf{L}^\dagger\mathbf{b})$, where the inner product is defined as $(\mathbf{a}, \mathbf{b}) = \overline{\mathbf{b}}^T\mathbf{a}$. With this definition, the adjoint eigenvalue problem can be rewritten as

$$\mathbf{L}^\dagger(\overline{\omega}, \mathbf{k})\mathbf{b} = 0.$$

Let us assume that, for the values of the parameters $\chi = \chi_0$, $\alpha = \alpha_0$, $\gamma = 0$, $\eta = 0$, and $p = p_0$, an algebraically double imaginary eigenvalue $\omega_0 = i\sigma_0$ exists with the Jordan block which satisfies the following equations

$$\begin{aligned} \mathbf{A}_0\mathbf{a}_0 - \sigma_0^2\mathbf{M}_0\mathbf{a}_0 &= 0, \\ \mathbf{A}_0\mathbf{a}_1 - \sigma_0^2\mathbf{M}_0\mathbf{a}_1 &= -2i\sigma_0\mathbf{M}_0\mathbf{a}_0, \end{aligned} \tag{C.12}$$

where $\mathbf{a}_0$ is an eigenvector and $\mathbf{a}_1$ is an associated vector at ω_0. Then, an eigenfunction $\mathbf{b}_0$ and an associated function $\mathbf{b}_1$ at the complex-conjugate eigenvalue $\overline{\omega}_0 = -i\sigma_0$ are governed by the adjoint equations

$$\begin{aligned} \mathbf{A}_0^T\mathbf{b}_0 - \sigma_0^2\mathbf{M}_0\mathbf{b}_0 &= 0, \\ \mathbf{A}_0^T\mathbf{b}_1 - \sigma_0^2\mathbf{M}_0\mathbf{b}_1 &= 2i\sigma_0\mathbf{M}_0\mathbf{b}_0. \end{aligned} \tag{C.13}$$

Note the orthogonality between the eigenvectors, that is

$$(\mathbf{M}_0\mathbf{a}_0, \mathbf{b}_0) = 0. \tag{C.14}$$

When the parameter p is perturbed in the vicinity of p_0 as $p = p_0 + \Delta p$, an approach similar to that used for $N = 2$ yields

$$\begin{aligned} \omega(p) &= i\sigma_0 \pm \sqrt{\Delta p \, \tfrac{i(\mathbf{A}'_p\mathbf{a}_0, \mathbf{b}_0)}{2\sigma_0(\mathbf{M}_0\mathbf{a}_1, \mathbf{b}_0)}} + o(\sqrt{|\Delta p|}), \\ \mathbf{a}(p) &= \mathbf{a}_0 \pm \mathbf{a}_1\sqrt{\Delta p \, \tfrac{i(\mathbf{A}'_p\mathbf{a}_0, \mathbf{b}_0)}{2\sigma_0(\mathbf{M}_0\mathbf{a}_1, \mathbf{b}_0)}} + o(\sqrt{|\Delta p|}), \\ \mathbf{b}(p) &= \mathbf{b}_0 \pm \mathbf{b}_1\sqrt{\Delta p \, \tfrac{i(\mathbf{A}'_p\mathbf{a}_0, \mathbf{b}_0)}{2\sigma_0(\mathbf{M}_0\mathbf{a}_1, \mathbf{b}_0)}} + o(\sqrt{|\Delta p|}), \end{aligned} \tag{C.15}$$

where $\mathbf{A}'_p = \left.\frac{\partial \mathbf{A}}{\partial p}\right|_{p=p_0}$. Therefore, the eigenvalues and eigenvectors of the undamped reversible system can be approximated in the vicinity of $p = p_0$, i.e. in the vicinity of the flutter boundary corresponding to the reversible-Hopf bifurcation.

Assume that at $p < p_0$ the eigenvalues of the undamped reversible system are imaginary, $\omega(p) = i\sigma(p)$, with an eigenvector $\mathbf{a}(p)$ and the eigenvector of the adjoint problem $\mathbf{b}(p)$. Then, at $p > p_0$ the eigenvalues (C.15) are complex-conjugate (denoting instability). A dissipative perturbation with the matrix $\mathbf{D}(\eta, \gamma)$ where $\mathbf{D}(0, 0) = 0$ changes the eigenvalue $\omega(p) = i\sigma(p)$ as follows

$$\begin{aligned} \omega(p, \eta, \gamma) = \omega(p) = \\ = -\tfrac{(\mathbf{D}'_\eta\mathbf{a}(p), \mathbf{b}(p))\eta + (\mathbf{D}'_\gamma\mathbf{a}(p), \mathbf{b}(p))\gamma}{2(\mathbf{M}_0\mathbf{a}(p), \mathbf{b}(p))} + o(|\eta|, |\gamma|). \end{aligned} \tag{C.16}$$

The following condition for the imaginary eigenvalue is assumed to hold

$$(\mathbf{D}'_\eta \mathbf{a}(p), \mathbf{b}(p))\eta + (\mathbf{D}'_\gamma \mathbf{a}(p), \mathbf{b}(p))\gamma = 0, \tag{C.17}$$

so that the eigenvalue remains imaginary after a dissipative perturbation. This means that the neutral stability surface is not abandoned after the dissipative perturbation. Using the perturbation formulas (C.15) for $\mathbf{a}(p)$ and $\mathbf{b}(p)$ in (C.17), introducing the damping ratio $\beta = \gamma/\eta$, and defining

$$\beta_0 = -\frac{(\mathbf{D}'_\eta \mathbf{a}_0, \mathbf{b}_0)}{(\mathbf{D}'_\gamma \mathbf{a}_0, \mathbf{b}_0)} = -\frac{(\mathbf{D}_i \mathbf{a}_0, \mathbf{b}_0)}{(\mathbf{a}_0, \mathbf{b}_0)}, \tag{C.18}$$

the following quadratic approximation in β can be found to the critical flutter load in the limit of vanishing dissipation

$$p = p_0 + \tfrac{2\sigma_0(\mathbf{M}_0\mathbf{a}_1, \mathbf{b}_0)}{i(\mathbf{A}'_p \mathbf{a}_0, \mathbf{b}_0)} \cdot \left(\tfrac{(\mathbf{D}'_\gamma \mathbf{a}_0, \mathbf{b}_0)}{[(\mathbf{D}'_\gamma \mathbf{a}_0, \mathbf{b}_1) + (\mathbf{D}'_\gamma \mathbf{a}_1, \mathbf{b}_0)]\beta_0 + [(\mathbf{D}'_\eta \mathbf{a}_0, \mathbf{b}_1) + (\mathbf{D}'_\eta \mathbf{a}_1, \mathbf{b}_0)]} \right)^2 (\beta - \beta_0)^2. \tag{C.19}$$

From the orthogonality of eigenvectors (C.14) and the expression for the mass matrix $\mathbf{M}_0 = \mathbf{I} + 4\mathbf{M}_1 \tan\alpha_0$ it follows immediately that the denominator in (C.18) vanishes at $\alpha_0 = 0$, thus confirming that in the case of the Beck column the external air drag damping is stabilizing. Now this result has been established for the discretized model of the Pflüger column of arbitrary dimension N.

In the case of $N = 2$, $\chi_0 = 1$, $\alpha_0 = 0.1$, $p_0 \approx 17.83368$, $\sigma_0 \approx 9.366049$, the following vectors are obtained

$$\mathbf{a}_0 \approx \begin{pmatrix} 0.720378 \\ 1 \end{pmatrix}, \quad \mathbf{a}_1 \approx -i \begin{pmatrix} 0.225316 \\ 0.478780 \end{pmatrix},$$
$$\mathbf{b}_0 \approx \begin{pmatrix} -1.828847 \\ 1 \end{pmatrix}, \quad \mathbf{b}_1 \approx i \begin{pmatrix} -0.3423417 \\ 0.505899 \end{pmatrix}. \tag{C.20}$$

With these vectors the formula (C.15) exactly reproduces Eq.(5.28). The formula (C.18) provides $\beta_0 \approx 1478.074$ in full accordance with Eq.(5.33) in the case of $N = 2$. Finally, Eq.(C.19) exactly reproduces Eq.(5.34).

For $N > 2$ the procedure is the same: one only needs to find the vectors $\mathbf{a}_0$, $\mathbf{a}_1$, $\mathbf{b}_0$, $\mathbf{b}_1$ solving (C.12) and (C.13) with the corresponding $N \times N$ matrices which entries are given by Eqs.(C.10) and (C.11).

Bibliography

[1] H. Ziegler. Die Stabilitätskriterien der Elastomechanik. *Ingenieur-Archiv*, 20(1):49–56, 1952.

[2] M. Beck. Die Knicklast des einseitig eingespannten, tangential gedrückten Stabes. *Zeitschrift für angewandte Mathematik und Physik ZAMP*, 3(3):225–228, 1952.

[3] A.G. Greenhill. On the strength of shafting when exposed both to torsion and to end thrust. *Proceedings of the Institution of Mechanical Engineers*, 34(1):182–225, 1883.

[4] E.L. Nicolai. On stability of the straight form of equilibrium of a column under axial force and torque. *Izv. Leningr. Politech. Inst.*, 31: 201–231, 1928.

[5] H. Ziegler. Ein nichtkonserviertes Stabilitätsproblem. *ZAMM - Journal of Applied Mathematics and Mechanics / Zeitschrift für Angewandte Mathematik und Mechanik*, 31(8–9):265–266, 1951.

[6] H. Ziegler. On the concept of elastic stability. volume 4 of *Advances in Applied Mechanics*, pages 351–403. 1956.

[7] H. Ziegler. *Principles of Structural Stability*. Birkhäuser Verlang, Basel-Stuttgart, 2 edition, 1977.

[8] A. Pflüger. *Stabilitätsprobleme der Elastostatik*. Springer-Verlag Berlin Heidelberg, 1 edition, 1950.

[9] A. Pflüger. Zur Stabilität des tangential gedrückten Stabes. *ZAMM - Journal of Applied Mathematics and Mechanics / Zeitschrift für Angewandte Mathematik und Mechanik*, 35(5):191–191, 1955.

[10] P.Y. Rocard. *Dynamic instability: automobiles, aircraft, suspension bridges*. F. Ungar Pub. Co., New York, 1957.

[11] V.V. Bolotin. *Nonconservative Problems of Theory of Elastic Stability*. Macmillan, corr. and authorized ed edition, 1963.

[12] K. Huseyin. *Vibrations and stability of multiple parameter systems*, volume 6. Springer Science & Business Media, 1978.

[13] H. Leipholz. *Stability theory: An introduction to the stability of dynamic systems and rigid bodies*. Vieweg+Teubner Verlag, 1987.

[14] D. R. Merkin. *Introduction to the Theory of Stability (Texts in Applied Mathematics)*, volume 24. Springer Science & Business Media, 1997.

[15] O.N. Kirillov. *Nonconservative Stability Problems of Modern Physics*. De Gruyter studies in mathematical physics 14. De Gruyter, 2013.

[16] M.P. Paidoussis. *Fluid-structure interactions*, volume 1-2. Academic press, Oxford, 2014.

[17] G. Herrmann and S. Nemat-Nasser. Models demonstrating instability on nonconservative mechanical systems. *Technical Report*, (NASA-CR-76763), 1966.

[18] G. Herrmann. Models demonstrating instability on nonconservative mechanical systems. *Technical Report*, (NASA-CR-1782), 1971.

[19] W.G. Wood, S.S. Saw, and P.M. Saunders. The kinetic stability of a tangentially loaded strut. *Proceedings of the Royal Society of London A: Mathematical, Physical and Engineering Sciences*, 313(1513):239–248, 1969.

[20] S.N. Prasad and G. Herrmann. Stability of a cantilevered bar subjected to a transverse follower force of fluid jet. *Ingenieur-Archiv*, 39(5):341–356, 1970.

[21] Y. Sugiyama, K. Katayama, and S. Kinoi. Flutter of cantilevered column under rocket thrust. *Journal of Aerospace Engineering*, 8(1):9–15, 1995.

[22] D. Bigoni and G. Noselli. Experimental evidence of flutter and divergence instabilities induced by dry friction. *Journal of the Mechanics and Physics of Solids*, 59(10):2208–2226, 2011.

[23] I. Elishakoff. Controversy associated with the so-called "follower forces": Critical overview. *Applied Mechanics Reviews*, 58(2):117–142, 2005.

[24] W.T. Koiter. Unrealistic follower forces. *Journal of Sound and Vibration*, 194(4):636–638, 1996.

[25] H. Ziegler. Linear elastic stability. a critical analysis of methods. *Zeitschrift für angewandte Mathematik und Physik ZAMP*, 4(2):89–121, 1953.

[26] Q.S. Nguyen. *Stabilité des structures élastiques*. Mathématiques et Applications. Springer Berlin Heidelberg, 1995.

[27] O. Bottema. The Routh-Hurwitz condition for the biquadratic equation. *Indagationes Mathematicae (Proceedings)*, 59:403–406, 1956.

[28] R. Krechetnikov and J.E. Marsden. Dissipation-induced instabilities in finite dimensions. *Rev. Mod. Phys.*, 79:519–553, 2007.

[29] O.N. Kirillov and F. Verhulst. Paradoxes of dissipation-induced destabilization or who opened Whitney's umbrella? *ZAMM - Journal of Applied Mathematics and Mechanics / Zeitschrift für Angewandte Mathematik und Mechanik*, 90(6):462–488, 2010.

[30] N.V. Banichuk, A.S. Bratus, and A.D. Myshkis. Stabilizing and destabilizing effects in non-conservative systems. *Journal of Applied Mathematics and Mechanics*, 53(2):158–164, 1989.

[31] V.V. Bolotin and N.I. Zhinzher. Effects of damping on stability of elastic systems subjected to nonconservative forces. *International Journal of Solids and Structures*, 5(9):965 – 989, 1969.

[32] I.P. Andreichikov and V.I. Yudovich. Stability of viscoelastic bars. *Izv. Akad. Nauk. (SSSR.) Mekh. Tverd. Tela.*, 9(2):78–87, 1974.

[33] S.H. Crandall. The effect of damping on the stability of gyroscopic pendulums. *Zeitschrift für angewandte Mathematik und Physik ZAMP*, 46:S761–S780, 1995.

[34] R.H. Plaut and E.F. Infante. The effect of external damping on the stability of Beck's column. *International Journal of Solids and Structures*, 6(5):491–496, 1970.

[35] R.H. Plaut. A new destabilization phenomenon in nonconservative systems. *ZAMM - Journal of Applied Mathematics and Mechanics / Zeitschrift für Angewandte Mathematik und Mechanik*, 51(4):319–321, 1971.

[36] S.S. Saw and W.G. Wood. The stability of a damped elastic system with a follower force. *Journal of Mechanical Engineering Science*, 17 (3):163–179, 1975.

[37] C. Oran. On the significance of a type of divergence. *Journal of Applied Mechanics*, 39(1):263–265, 1972.

[38] O.N. Kirillov. Singularities in structural optimization of the Ziegler pendulum. *Acta Polytechnica*, 51(4):32–43, 2011.

[39] O.N. Kirillov and A.O. Seyranian. Stabilization and destabilization of a circulatory system by small velocity-dependent forces. *Journal of Sound and Vibration*, 283(3):781–800, 2005.

[40] F.M. Detinko. Lumped damping and stability of Beck column with a tip mass. *International Journal of Solids and Structures*, 40(17): 4479–4486, 2003.

[41] P. Pedersen. Influence of boundary conditions on the stability of a column under non-conservative load. *International Journal of Solids and Structures*, 13(5):445–455, 1977.

[42] Y. Sugiyama, K. Kashima, and H. Kawagoe. On an unduly simplified model in the non-conservative problems of elastic stability. *Journal of Sound and Vibration*, 45(2):237–247, 1976.

[43] S. Ryu and Y. Sugiyama. Computational dynamics approach to the effect of damping on stability of a cantilevered column subjected to a follower force. *Computers & Structures*, 81(4):265–271, 2003.

[44] O.N. Kirillov and A.O. Seyranian. The effect of small internal and external damping on the stability of distributed non-conservative systems. *Journal of Applied Mathematics and Mechanics*, 69(4):529–552, 2005.

[45] G. Herrmann and S. Nemat-Nasser. Instability modes of cantilevered bars induced by fluid flow through attached pipes. *International Journal of Solids and Structures*, 3(1):39–52, 1967.

[46] W. Kelvin and P.G.Tait. *Treatise on Natural Philosophy (part I*, volume 1. Cambridge University Press, Cambridge, 1879.

[47] A. Jenkins. Self-oscillation. *Physics Reports*, 525(2):167–222, 2013.

[48] S. Maegawa, F. Itoigawa, and T. Nakamura. Effect of normal load on friction coefficient for sliding contact between rough rubber surface and rigid smooth plane. *Tribology International*, 92:335–343, 2015.

[49] J.T. Oden and J.A.C. Martins. Models and computational methods for dynamic friction phenomena. *Computer Methods in Applied Mechanics and Engineering*, 52(1):527–634, 1985.

[50] J.A.C. Martins, J.T. Oden, and F.M.F. Sim oes. A study of static and kinetic friction. *International Journal of Engineering Science*, 28(1): 29–92, 1990.

[51] M. Tommasini, O.N. Kirillov, D. Misseroni, and D. Bigoni. The destabilizing effect of external damping: singular flutter boundary for the Pflüger column with vanishing external dissipation. *Journal of the Mechanics and Physics of Solids*, 91:204–215, 2016.

[52] L.W. Chen and D.M. Ku. Eigenvalue sensitivity in the stability analysis of Beck's column with a concentrated mass at the free end. *Journal of Sound and Vibration*, 153(3):403–411, 1992.

[53] O.M. O'Reilly N.K., Malhotra N.S., and Namachchivaya. *Nonlinear Dynamics*, 10(1):63–87, 1996.

[54] Stephen Wiggins. *Introduction to applied nonlinear dynamical systems and chaos*, volume 2. Springer Science & Business Media, 2003.

[55] M. Clerc, P. Coullet, and E. Tirapegui. The Maxwell-Bloch description of 1/1 resonances. *Optics Communications*, 167(1):159–164, 1999.

[56] M.G. Clerc and J.E. Marsden. Dissipation-induced instabilities in an optical cavity laser: A mechanical analog near the 1:1 resonance. *Phys. Rev. E*, 64:067603, 2001.

[57] M.V. Berry and P. Shukla. Curl force dynamics: symmetries, chaos and constants of motion. *New Journal of Physics*, 18(6):063018, 2016.

[58] David G. Grier. A revolution in optical manipulation. *Nature*, 424: "810–816", 2003.

[59] P. Wu, R. Huang, C. Tischer, A. Jonas, and E.L. Florin. Direct measurement of the Nonconservative Force Field Generated by Optical Tweezers. *Phys. Rev. Lett.*, 103:108101, 2009.

[60] S.H. Simpson and S. Hanna. First-order nonconservative motion of optically trapped nonspherical particles. *Phys. Rev. E*, 82:031141, 2010.

[61] N. Hoffmann and L. Gaul. Effects of damping on mode-coupling instability in friction induced oscillations. *ZAMM - Journal of Applied Mathematics and Mechanics / Zeitschrift für Angewandte Mathematik und Mechanik*, 83(8):524–534, 2003.

[62] P.V. Bayly and S.K. Dutcher. Steady dynein forces induce flutter instability and propagating waves in mathematical models of flagella. *Journal of The Royal Society Interface*, 13(123):20160523, 2016.

[63] Shreyas Mandre and L. Mahadevan. A generalized theory of viscous and inviscid flutter. *Proceedings of the Royal Society of London A: Mathematical, Physical and Engineering Sciences*, 466:141–156, 2009.

[64] G. De Canio, E. Lauga, and R.E. Goldstein. Spontaneous oscillations of elastic filaments induced by molecular motors. *Journal of The Royal Society Interface*, 14(136), 2017.

[65] V.I. Arnol'd. Lectures on bifurcations in versal families. *Russian Mathematical Surveys*, 27(5):54, 1972.

[66] W.F. Langford. *Hopf Meets Hamilton Under Whitney's Umbrella*, pages 157–165. 2003.

[67] I. Hoveijn and O.N. Kirillov. Singularities on the boundary of the stability domain near 1:1-resonance. *Journal of Differential Equations*, 248(10):2585–2607, 2010.

[68] R.S MacKay. Movement of eigenvalues of Hamiltonian equilibria under non-Hamiltonian perturbation. *Physics Letters A*, 155(4):266–268, 1991.

[69] A. Bloch, P.S. Krishnaprasad, J.E. Marsden, and T.S. Ratiu. Dissipative perturbations of Hamiltonian flows. *Mathematical Research*, 79: 71–71, 1994.

[70] O.N. Kirillov. Gyroscopic stabilization in the presence of nonconservative forces. *Doklady Mathematics*, 76(2):780–785, 2007.

[71] K. Stewartson and P.H. Roberts. On the motion of liquid in a spheroidal cavity of a precessing rigid body. *Journal of Fluid Mechanics*, 17(1):1–20, 1963.

[72] H.J. Braviner and G.I. Ogilvie. Tidal interactions of a Maclaurin spheroid? I. Properties of free oscillation modes. *Monthly Notices of the Royal Astronomical Society*, 441(3):2321–2345, 2014.

[73] S. Chandrasekhar. Solutions of Two Problems in the Theory of Gravitational Radiation. *Phys. Rev. Lett.*, 24:611–615, 1970.

[74] S. Chandrasekhar. On Stars, Their Evolution and Their Stability. *Science*, 226(4674):497–505, 1984.

[75] L. Lindblom and S.L. Detweiler. On the evolution of the homogeneous ellipsoidal figures. *The Astrophysical Journal*, 213:193–199, 1977.

[76] N. Andersson. Gravitational waves from instabilities in relativistic stars. *Classical and Quantum Gravity*, 20(7):105–144, 2003.

[77] E.P. Holipainen. On the effect of friction in baroclinic waves. *Tellus*, 13(3):363–367, 1961.

[78] B.T. Willcocks and J.G. Esler. Nonlinear baroclinic equilibration in the presence of Ekman friction. *Journal of Physical Oceanography*, 42 (2):225–242, 2012.

[79] T.J. Bridges and F. Dias. Enhancement of the Benjamin-Feir instability with dissipation. *Physics of fluids*, 19(10):104104, 2007.

[80] O.N. Kirillov. A theory of the destabilization paradox in non-conservative systems. *Acta Mechanica*, 174(3):145–166, 2005.

[81] O.N. Kirillov. Singular diffusionless limits of double-diffusive instabilities in magnetohydrodynamics. *Proceedings of the Royal Society of London A: Mathematical, Physical and Engineering Sciences*, 473 (2205), 2017.

[82] A. Luongo, M. Ferretti, and F. D'Annibale. Paradoxes in dynamic stability of mechanical systems: investigating the causes and detecting the nonlinear behaviors. *SpringerPlus*, 5(1):60, 2016.

[83] J.L. Friedman and B.F. Schutz. Secular instability of rotating Newtonian stars. *The Astrophysical Journal*, 222:281–296, 1978.

[84] B.F. Schutz. Perturbations and Stability of Rotating Stars - Part Three - Perturbation Theory for Eigenvalues. *Monthly Notices of the Royal Astronomical Society*, 190:21–31, 1980.

[85] Y. Sugiyama, J. Matsuike, B. Ryu, K. Katayama, S. Kinoi, and N. Enomoto. Effect of concentrated mass on stability of cantilevers under rocket thrust. *AIAA Journal*, 33(3):499–503, 1995.

[86] Y. Sugiyama, K. Katayama, K. Kiriyama, and B. Ryu. Experimental verification of dynamic stability of vertical cantilevered columns subjected to a sub-tangential force. *Journal of sound and vibration*, 236 (2):193–207, 2000.

[87] M.A. Langthjem and Y. Sugiyama. Dynamic stability of columns subjected to follower loads: a survey. *Journal of Sound and Vibration*, 238 (5):809–851, 2000.

[88] A.K. Chopra. *Dynamics of Structures*. Prentice Hall International Series in Civil Engineering and Engineering Mechanics. Prentice Hall, 4 edition, 2011.

[89] R.W. Clough and J. Penzien. *Dynamics of Structures*. McGraw-Hill Companies, 1975.

[90] G.T.S. Done. Damping configurations that have a stabilizing influence on nonconservative systems. *International Journal of Solids and Structures*, 9(2):203–215, 1973.

[91] J.A. Walker. A note on stabilizing damping configurations for linear nonconservative systems. *International Journal of Solids and Structures*, 9(12):1543–1545, 1973.

[92] N.I. Zhinzher. Effect of dissipative forces with incomplete dissipation on the stability of elastic systems. *Izv. Ross. Akad. Nauk. MTT*, 1: 149–155, 1994.

[93] Y.G. Panovko and S.V. Sorokin. Quasi-stability of viscoelastic systems with follower forces. *Mech. Solids*, 2:128–132, 1987.

[94] O.N. Kirillov and A.P. Seyranian. Dissipation induced instabilities in continuous non-conservative systems. *PAMM*, 5(1):97–98, 2005.

[95] G. Wang and Y. Lin. A new extension of Leverrier's algorithm. *Linear Algebra and its Applications*, 180:227–238, 1993.